Martin Hantinger BSc

Mixer design with CFD for marine Diesel SCR application

MASTER'S THESIS

to achieve the university degree of

Diplom-Ingenieur

Master's degree programme: Chemical and Process Engineering

submitted to

Graz University of Technology

Supervisor

Ass.Prof. Dipl.-Ing. Dr.techn. Stefan Radl

Institute of Process and Particle Engineering

External supervisor

Dipl.-Ing. Alexander Ruth

AVL List GmbH

Graz, February 2017

AFFIDAVIT

I declare that I have authored this thesis independently, that I have not used other than the declared sources/resources, and that I have explicitly indicated all material which has been quoted either literally or by content from the sources used.

The text document uploaded to TUGRAZonline is identical to the present master‘s thesis dissertation.

_____	_____
Date	Signature

Abstract

This thesis investigated the mixer design for a marine Diesel selective catalytic reduction (SCR) application via computational fluid dynamics (CFD) simulations. In times of stricter exhaust gas emission regulations SCR gains more and more importance. The thesis was made at AVL List GmbH in Graz.

First, an overview of geometries used in industry, as well as relevant spray mixing parameters is provided based on a literature survey. For mixing parameters a short numerical investigation of limits is made for completely unmixed and perfectly mixed condition. The present thesis is focused on the so-called "uniformity index", and the "mixedness quality".

A reference geometry is investigated in light of its mixing characteristics. For this geometry flow properties like angular momentum and swirl number, as well as spray mixing characteristics are evaluated. The goal is to determine (i) the evaluation duration (i.e., the simulation time), and (ii) the mesh size dependency of the calculated flow properties. The uniformity index shows the best behaviour with respect to mesh and evaluation duration.

Finally, the reference geometry is compared with other mixer geometries. The goal was to identify new geometries with similar mixing properties.

Kurzfassung

Diese Masterarbeit untersuchte Mischer Designs für selektive katalytische Reduktion (SCR) bei Schiffsdieselmotoren anhand von Computational Fluid Dynamics (CFD) Simulationen. In Zeiten strenger Abgasemissionsregulierungen gewinnt SCR mehr und mehr an Bedeutung. Die Arbeit wurde an der AVL List GmbH in Graz erstellt.

Es wird ein Überblick über Geometrien, die in der Industrie verwendet werden, und Spraymischparameter auf Basis einer Literaturrecherche gegeben. Für die Parameter erfolgt eine kurze Untersuchung der Grenzwerte für einen komplett ungemischten und einen perfekt gemischten Zustand. Die Arbeit fokussiert auf den sogenannten "uniformity index" und die "mixedness quality".

Eine Referenzgeometrie wird in Hinsicht auf Spraymischeigenschaften untersucht. Dafür werden Strömungseigenschaften wie Drehimpuls und Swirlnumber, sowie die Sprayparameter ausgewertet. Ziel ist es (i) den Auswertezeitraum (d.h. die Simulationszeit), und (ii) die Gitterabhängigkeit der Mischparameter darzustellen. Hier zeigt der uniformity index die besten Eigenschaften in Hinsicht auf Unabhängigkeit von Gitter und Auswertezeitraum.

Die Referenzgeometrie wird mit anderen Mischergeometrien verglichen. Ziel war es neue Geometrien mit ähnlichen Mischereigenschaften zu finden.

Acknowledgement

I want to give thanks to my external supervisor Dipl.-Ing. Alexander Ruth from AVL. He was very dedicated with help and advice and has large share on success of this work. I also thank Dipl.-Ing. Karl-Heinz Schäfer who supported me with issues about *AVL FIRE*®.

I thank Ass.Prof. Dipl.-Ing. Dr.techn. Stefan Radl from TU Graz for support. He suggested me this thesis.

At last I thank my parents and friends for support.

Table of contents

List of figures

List of tables

Abbreviations

AAPI	air assisted particle injection
BL	Boundary layer
CFD	Computational fluid dynamics
CFL	Courant-Friedrichs-Lewy number
CVP	Counter rotating vortex pair
DDM	Discrete droplet method
DOC	Diesel oxidation catalyst
ECA	Emission control area
EPA	Environmental protection agency
IMO	International maritime organization
MM	Molar mass
PM	Particulate matter
PIV	Particle image velocimetry
RANS	Reynolds averaged Navier Stokers
SCR	Selective catalytic reduction
SMD	Sauter mean diameter
TKE	Turbulent kinetic energy
Turb.	Turbulence or turbulent

Nomenclature

Latin symbols

A	Area	$[m^2]$
c	Local number density of droplets per area	$[1/m^2]$
c_p	Specific heat	$[J/kg\ K]$
C	Mass concentration of species	$[-]$
C_D	Drag coefficient	$[-]$
C_p	Cunningham factor	$[-]$
d_{32}	Sauter diameter of droplets	$[m]$
d_g	Molecule diameter in gas phase	$[m]$
D	Diameter	$[m]$
D	Diffusion coefficient	$[m^2/s]$
DM	Degree of mixedness (not to be mistaken with ξ!)	$[-]$
E_a	Activation energy	$[J/mol]$
F	Force	$[N]$
j	Mass flux	$[kg/m^2\ s]$
$\vec{j}$	Diffusive mass flux	$[kg/m^2\ s]$
g	Gravity	$[m/s^2]$
G	Energy ratio gradients	$[-]$
k	Turbulent kinetic energy	$[m^2/s^2]$
k	Reaction rate	$[various]$
L	Characteristic or channel length	$[m]$
L	Angular momentum	$[kg\ m^2/s]$
L	Latent heat of evaporation	$[J/kg]$
Le	Lewis number	$[-]$

k	Reaction rate	$[various]$
k_b	Boltzmann constant	$[J/kg]$
Kn	Knudsen number	$[-]$
m	Mass	$[kg]$
n	Number of faces	$[-]$
n	Rotational speed	$[1/min]$
n	Moles	$[mol]$
N	Number of droplets	$[-]$
Nu	Nusselt number	$[-]$
p	Pressure	$[Pa]$
$\vec{P}$	Point	$[m]$
Pr	Prandtl number	$[-]$
q	Density distribution	$[1/m]$
Q	Cumulative distribution	$[-]$
Q_m	Mixedness quality	$[-]$
$Q_{m,f}$	Q_m with face averaged diameter U	$[-]$
$\dot{Q}$	Convectiv heat flux	$[W]$
$\dot{r}$	Reaction rate	$[various]$
R	Radius	$[m]$
R	Kinetic energy ratio	$[-]$
RES	Residual	$[-]$
Re	Reynolds number	$[-]$
R_{ij}	Turbulent stress tensor	$[kg/m^2\ s^2]$
Sc	Schmidt number	$[-]$
Sh	Sherwood number	$[-]$
t	Time	$[s]$

Δt	Timestep	$[s]$
T	Temperature	$[°C]$
T	Target function	$[-]$
u	Velocity	$[m/s]$
u_g	Crossflow velocity	$[m/s]$
U	Unmixedness	$[-]$
V	Volume	$[m^3]$
$\dot{V}$	Volume flow	$[m^3/s]$
We	Weber number	$[-]$
w	Mass fraction	$[-]$
X	Conversion	$[-]$
x	Mole fraction	$[-]$
$\vec{x}$	Position vector	$[m]$
y^+	Normalized wall distance	$[-]$
Y	Yield	$[-]$
z	Number fraction	$[-]$

Greek symbols

α	Heat transfer coefficient	$[W/m^2\ K]$
γ	Uniformity index	$[-]$
γ	Activity coefficient	$[-]$
ϵ	Emissivity	$[-]$
ϵ	Concentration ratio	$[-]$
ϵ	Dissipation rate	$[m^2/s^3]$
κ	Isotropic exponent	$[-]$
κ	Von Karman constant	$[-]$

λ	Heat conductance	$[W/m\,K]$
λ	Free path length	$[m]$
μ	Dynamic viscosity	$[Pa\,s]$
ν	Kinematic viscosity	$[m^2/s]$
σ	Surface tension	$[N/m]$
σ	Stefan-Boltzmann constant	$[W/m^2K^4]$
ξ	Degree of mixedness (not not to be mistaken with DM!)	$[-]$
ρ	Density	$[kg/m^3]$
ϕ	Placeholder for any quantity	
ψ	Pressure oriented on outlet	$[Pa]$
ω	Angular velocity	$[rad/s]$
ω	Weighting factor	$[-]$

Subscripts

0	Start-time
1	Number
3	Mass
$comp.$	Complete, complete profile
cyl	Cylinder
D	Drag
d	Diameter, droplet
d,f	Face averaged diameter
env	Environment
$evap.$	Evaporated
f	Fictious
$first$	First iteration

G	Mass
g	Gas
$half$	Half profile
$HNCO$	Isocyanic acid
i	Direction, face or cell number, component
$inj.$	Injected
$last$	Last iteration
max	Maximum
min	Minimum
mol	Molecular
$NH3$	Ammonia
NOX	NO_x
out	Outlet
p	Particles
R	Energy ratios
rel	Relative
s	Spray, spatial, vortex
$start$	Start value
$stat.$	Static
tot	Total
UWL	Urea water solution
UR	Urea
WD	With droplets
$\dot{}$	Flow
$\bar{}$	Average
$\hat{}$	Instantaneous local quantity

1. Introduction

Diesel engines have a wide application range in modern traffic. Motorcars, trucks and ships are only a few of them. The global traffic grows from year to year, and because of this also exhaust gas emissions come into the focus of public debate. A disadvantage of Diesel engines is the relatively high emissions of NO_x and particulate matter (PM). These pollutants have a negative influence on human health, and consequently states want to reduce these emissions through stricter regulations. In the past these standards could be achieved via an improvement of the combustion process (see Nova and Tronconi [1]). However, today it is necessary to perform aftertreatment of exhaust gases to satisfy current regulations. One possibility of such an aftertreatment process is the selective catalytic reduction (SCR) process [1]. Therein, the so-called Adblue® liquid, i.e., a urea water solution, is injected into the exhaust system where it is decomposed to NH_3 which reacts with NO_x. For a satisfactory operation of the SCR process, it is necessary to achieve a homogeneous distribution of NH_3. This can be only achieved with installations that mix the gas with the injected liquid. The aim of the mixer is to achieve a spatially homogeneous distribution of NH_3 at minimum cost, i.e., small backpressure. Also the design of the mixer should be simple, and the installation space should be as small as possible. The focus of the present thesis is to simulate the effect of different mixer geometries on the mixing performance and pressure drop characteristics, as well as parameters characterising them.

1.1. Decomposing mechanism of urea

Because of toxicity, the handling of NH_3 in gaseous form is not easy. A good alternative is urea: it is not toxic and easy to handle. At elevated temperatures urea decomposes in the exhaust gas via a two-step reaction to NH_3 (Koebl et. al. [2]).

Urea thermolysis:

$$CO(NH_2)_2 \rightarrow NH_3 + HNCO \qquad \textbf{R 1}$$

Isocyanic acid hydrolysis:

$$HNCO + H_2O \rightarrow NH_3 + CO_2 \qquad \textbf{R 2}$$

This thesis focuses on the decomposition of urea, while SCR reactions are not considered. However, they are summarized next for completeness.

1.2. SCR reactions

During NO_x reduction, three important reactions occur [1].

Standard SCR:

$$8\,NO + 8\,NH_3 + 2\,O_2 \rightarrow 8\,N_2 + 12\,H_2O \qquad \textbf{R 3}$$

Fast SCR:

$$4\,NO + 4\,NO_2 + 8\,NH_3 \rightarrow 8\,N_2 + 12\,H_2O \qquad \textbf{R 4}$$

NO_2 SCR:

$$6\,NO_2 + 8\,NH_3 \rightarrow 7\,N_2 + 12\,H_2O \qquad \textbf{R 5}$$

R 4 is the fastest of these three reactions. To promote this reaction, a Diesel oxidation catalyst (DOC) is commonly used to form more NO_2 over platinum via the following reaction [1]:

$$2\,NO + O_2 \rightarrow 2\,NO_2 \qquad \textbf{R 6}$$

If too much NO_2 is produced in the DOC (i.e., in case $\frac{NO_2}{NO} > 1$), R 5 becomes operative. This is undesirable because NO_2 can react to N_2O which is a strong greenhouse gas [1]. To meet current Euro VI regulations, cycle-averaged deNOx efficiencies approaching 95 % must be realized [1], necessitating a precise control of the above parallel reaction network.

1.3. Conversion

An important issue is to achieve a maximum yield of NH_3 from the injected urea. To achieve this, the conversion X_{NH3} is taken into account. It is the ratio of ammonia produced (denoted as n_{NH3}) and the maximum amount of ammonia which can be produced (denoted as $n_{NH3,max}$) upon complete conversion of urea.

$$X_{NH3} = \frac{n_{NH3}}{n_{NH3,max}} \qquad \textbf{R 7}$$

1.4. Motivation

Motivation for this thesis is that only a few geometries exist with sufficient mixing performance. These are also protected by patents. Because of this a new geometry patented by AVL is from high interest for the company.

1.5. Regulations

NO_x emissions in marine diesel applications are regulated globally with Tier I and Tier II [3]. In North America, the US Caribbean and the North and Baltic sea, also so-called emission control areas (ECA) exist with stricter standards. For US ECAs Tier III regulations are applied for NO_x, while for North and Baltic Sea these regulations do not apply [4].

In Tier regulations marine engines are classified according to their displacement per cylinder (see Table 1-1).

Cate-gory	Displacement per cylinder (D)		Basic engine technology
	Tier 1-2	Tier 3-4	
1	$D < 5\ dm^3$ †	$D < 7\ dm^3$	Land-based nonroad diesel
2	$5\ dm^3 \leq D < 30\ dm^3$	$7\ dm^3 \leq D < 30\ dm^3$	Locomotive engine
3	$D \geq 30\ dm^3$	$D \geq 30\ dm^3$	Unique marine engine design

† And power ≥ 37 kW

Table 1-1: Marine engine categories [4]

Table 1-2 shows Tier 4 standards valid for category 1 and 2.

Power (P) $[kW]$	NO_x $[g/kWh]$	HC $[g/kWh]$	PM $[g/kWh]$	Date
$P \geq 3700$	1.8	0.19	0.12[a]	2014[c]
	1.8	0.19	0.06	2016[b,c]
$2000 \leq P < 3700$	1.8	0.19	0.04	2014[c,d]
$1400 \leq P < 2000$	1.8	0.19	0.04	2016[c]
$600 \leq P < 1400$	1.8	0.19	0.04	2017[d]

a - 0.25 $[g/kWh]$ for engines with 15-30 $[dm^3]$ per cylinder displacement.

b - Optional compliance start dates can be used within these model years.

c - Option for Cat. 2: Tier 3 $PM/NO_x + HC$ at 0.14/7.8 $[g/kWh]$ in 2012, and Tier 4 in 2015.

d - The Tier 3 PM standards continue to apply for these engines in model years 2014 and 2015 only

Table 1-2: Tier 4 Standards for Marine Diesel Category 1/2 Engines [4]

Tier 3 standards for NO_x were set into force for category 3 engines in North American and US Caribbean ECAs in 2016. The environmental protection agency's (EPA) Tier 2-3 NO_x limits are equivalent to the respective international maritime organization's (IMO) Tier II-III standards. Depending on the engine speed, Tier 2 NO_x limits range from 14.4 to 7.7 $[g/kWh]$, while Tier 3 limits range from 3.4 to 1.96 $[g/kWh]$. In addition to the NO_x limits, EPA adopted an HC emission standard of 2.0 $[g/kWh]$ and a CO standard of 5.0 $[g/kWh]$ for new category 3 engines. No emission standard was adopted for PM, but manufactures are required to measure and report PM emissions [4].

In general it can be said that Euro VI truck NO_x regulations are approximately five times stricter than Tier III.

1.6. Goals

In this thesis goal is to find parameters used in industry relevant for mixing of a droplet spray with a typical gas stream in an engine aftertreatment system. These parameters should be studied based on a well-defined geometry. The overall goal is to find connections between flow and spray parameters that maximize mixing performance. The result of the thesis should be useful for a rational design of the spray-mixer systems: it should be possible to draw conclusions of spray behaviour based on computationally less intensive flow simulations. Finding new geometries would be made easier by making lots of these simulations with justifiable effort. Also, different droplet injection methods and their influence should be compared in order to allow a fast and precise simulation and design of the aftertreatment system in the future.

Also a goal is to find a new mixer geometry. In best case the geometry has similar pressure drop and mixing performance compared to a well-defined geometries. For this it is necessary that the conversion is high, as much spray as possible evaporates and NH_3 is distributed as homogeneous as possible.

1.7. Overview

The thesis is structured as follows:

- In Chapter 2 the currently available mixer geometries and parameters relevant for mixing are summarized.
- Chapter 3 details the governing equations for the CFD simulations.
- Chapter 4 summarizes simulation settings, operation and boundary conditions.

- In Chapter 5 simulation of flow around an inclined plate, including a detailed description of mesh generation, symmetry assessment, gas and spray mixing properties and a comparison of air assisted and non-air assisted spray injection is provided.

1.8. References

[1] I. Nova and E. Tronconi, *Urea-SCR technology for deNOx after treatment of Diesel exhausts*. Springer, New York, 2014.

[2] M. Koebel, M. Elsener, and M. Kleemann, "Urea-SCR: a promising technique to reduce NOx emissions from automotive diesel engines," *Catal. today*, vol. 59, no. 3, pp. 335–345, 2000.

[3] "DieselNet: Emission Standards » International : IMO Marine Engine Regulations." [Online]. Available: https://www.dieselnet.com/standards/inter/imo.php. [Accessed: 03-Feb-2017].

[4] "DieselNet: Emission Standards » United States Marine Diesel Engines." [Online]. Available: https://www.dieselnet.com/standards/us/marine.php. [Accessed: 02-Feb-2017].

2. State of the art

2.1. Mixer design

For proper working of the Diesel oxidation catalyst (DOC) it is very important to get a homogenous distribution of NH_3 in the flow. To achieve this, mixers are necessary. A lot of investigations for different mixer designs in marine applications have been made. Some of them will be shown in the following section. Also, a goal is to have low backpressure, high conversion X_{NH3} (defined in Chapter 1.3), and a simple geometry.

2.1.1. Geometries for rectangular ducts

In Choi et al. [1] a numerical simulations of the flow in mixers is made. Figure 2-1 shows the computational domain, in which the urea water solution is injected in front of the mixer into the exhaust pipe. The pipe has a rectangular cross section in these previous simulations.

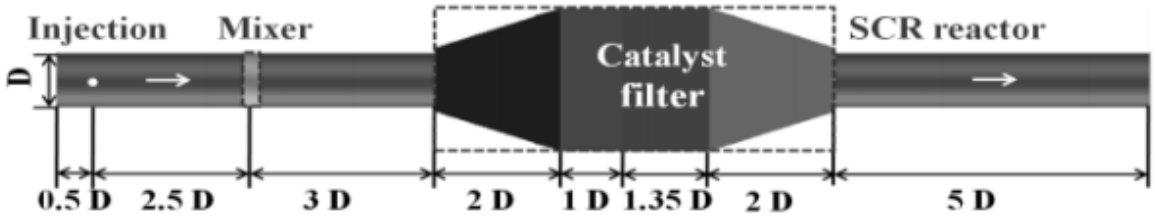

Figure 2-1: Computional domain used for simulation in Choi et al. [1]

In Figure 2-2 the three geometries investigated by Choi et al. [1] are shown. Each mixer has 36 vanes in the same angle of 45°. The vanes have also the same area to investigate the effect on pressure drop.

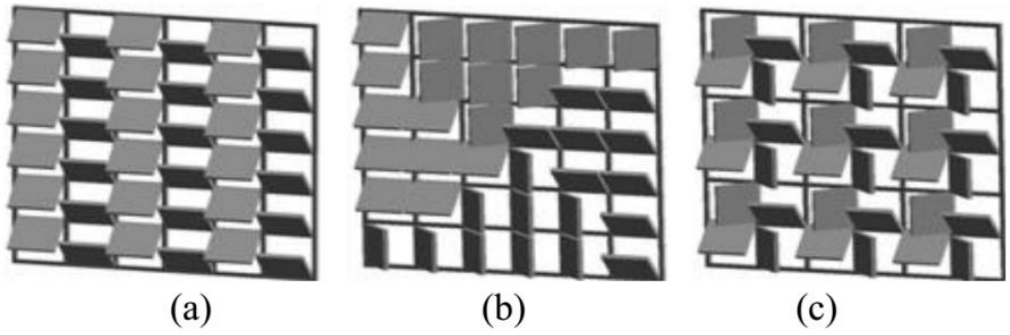

Figure 2-2: Geometry of three types of mixers: (a) up-and-down, (b) entire swirl, (c) partial swirl in [1].

Quantity	Value
w_{N2} $[-]$	0.77
w_{O2} $[-]$	0.23
$\overline{u}_g$ $\left[\frac{m}{s}\right]$	15.4
T $[K]$	623

Table 2-1: Simulation conditions in Choi et al. [1]

Table 2-1 summarizes the simulation conditions of Choi et al. [1]. In Table 2-2 the simulated cases and their backpressure are shown. Case 2 and Case 3 have similar backpressure; Case 4 a much higher one.

Case	Mixer type	Pressure drop
1	no mixer	100 %
2	up-and-down	180 %
3	entire swirl	175 %
4	partial swirl	216 %

Table 2-2: Classified cases according to mixer types [1]

Important for the effectiveness of the mixer is the conversion Specifically, the urea water-solution should react as complete as possible to NH_3. This is depicted in Figure 2-3. Region 1 in the figure extends from the rear side of the mixer before the SCR reactor, Region 2 is located at the front side of the catalyst filter in the reactor, and Region 3 is inside the catalyst filter. It shows that the conversion of Case 1 is very bad. Case 3 is the optimum case in view of conversion. Case 4 is at same level as Case 3 near the exit, however, lower in region 3 and shortly downstream.

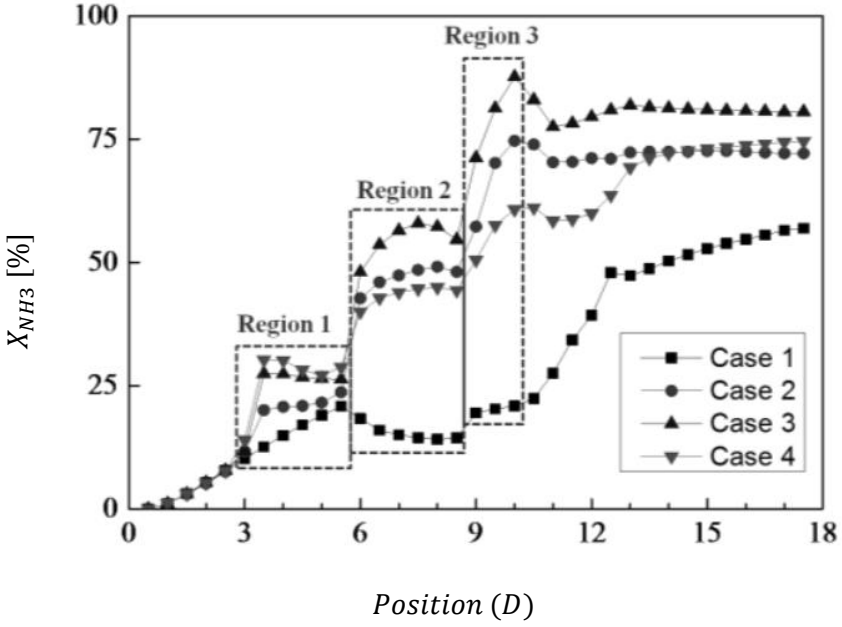

Figure 2-3: Conversion of ammonia for different cases over the channel length expressed as multiples of the channel size *D* [1].

The uniformity index γ is shown in Figure 2-4 (see Chapter 2.2.1 for the definition of γ), where γ was calculated using the concentration of NH_3. Case 1 has very bad mixing. Case 2 has a worse mixing than Case 3 and 4, which are very similar.

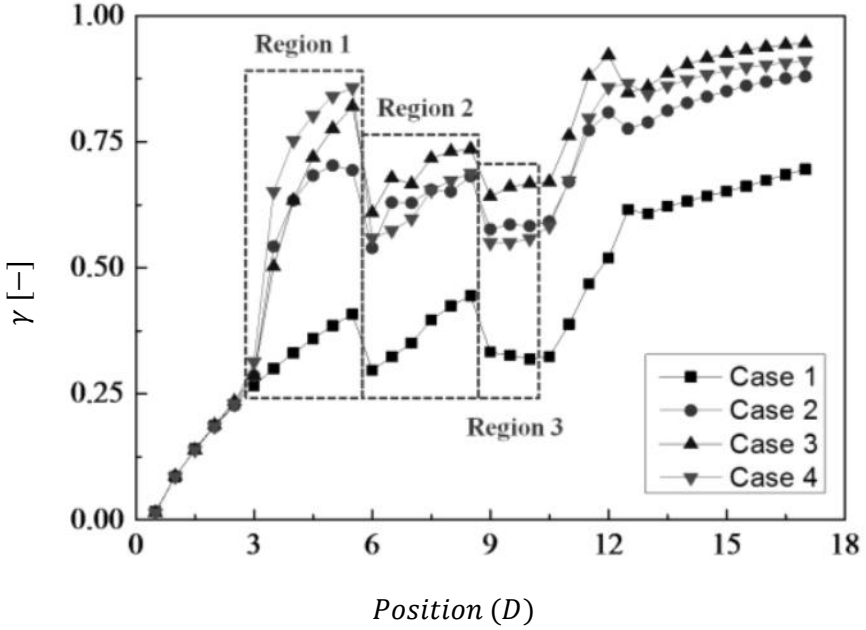

Figure 2-4: Uniformity index for different cases over the channel length expressed as multiples of the channel size *D* [1].

2.1.2. Geometries for circular ducts

Also for circular geometries a couple of mixer designs exist. In Zheng et al. [2] some mixers, which perform generally very good, are summarized. They can be divided in three different main designs: cone, two stage and butterfly mixers.

2.1.2.1. Cone mixers

Cone mixers have a shape similar to an impeller. They have a good mixing performance, however, a relatively high pressure drop [2].

2.1.2.2. Two stage mixers

These mixers have been developed to achieve best mixing performance at different operation points. The goal is to compensate the different spray angles with the first stage and use the second stage for mixing [2].

2.1.2.3. Butterfly mixers

Butterfly mixer have been developed based on the following principles [2]:

- leading edges that face the flow direction, thereby reducing pressure drop and avoiding flow separation,
- a large surface area that facilitates atomization and evaporation of liquid droplets, and liquid films, due to spray droplet collisions with the impingement surfaces
- strong flow deflection that generates turbulence, in particular, diverting flow from the centre of the duct towards the walls.

2.1.3. Conclusion from current mixers

Mixers shown in 2.1.1 and 2.1.2 have in common a complex design. However, customers of marine Diesel applications prefer simple and easy to manufacture solutions for which these designs are not suitable.

2.2. Spray mixing parameters

The aim of a spray mixer in its final application is to generate a homogenously distributed spray. For quantification of the spray distribution, some of the most important parameters from literature are presented next.

All parameters in this thesis have in common that they are evaluated on a two-dimensional (i.e., a cross-sectional area) or three-dimensional (i.e., volume) mesh. This is schematically depicted in Figure 2-5, in which A_i denotes the area of a control area (for two-dimensional

mesh), and V_i the volume of a control volume (for three dimensional mesh). For a three dimensional mesh ϕ_i are quantities (e.g., the droplet mass) in this cell at time t, while for a two dimensional mesh ϕ_i are accumulated quantities from particles which passed this cell between time t_{min} and t_{max}. Spray particles are recorded when they are passing the cross section from injector in distances of diameter to three times pipe diameter from injector.

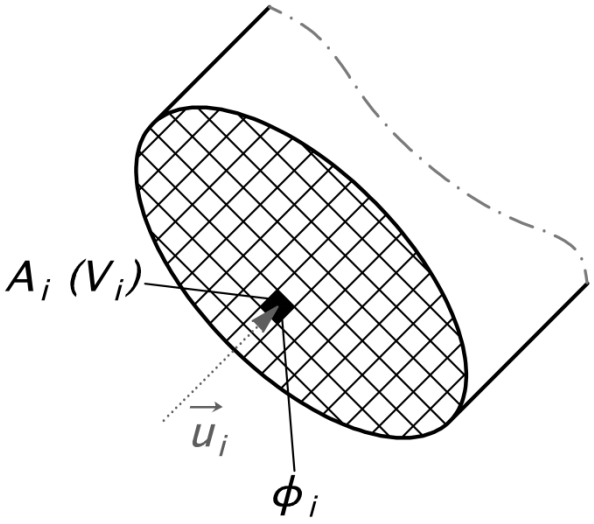

Figure 2-5: Illustration of the surface mesh used to evaluate mixing in cross-sectional areas of the simulation domain.

In Eqn. 2-1 shows calculation of property ϕ_i of a two dimensional mesh.

$$\phi_i = \sum_{i=1}^{N} \underbrace{\phi_d}_{\phi \; for \; droplet} \qquad \textbf{Eqn. 2-1}$$

There ϕ_d is property ϕ for a single droplet. This is summed up for all *N* droplets (see Eqn. 2-1) which are passing this area in the time interval t_{min} and t_{max}. In Eqn. 2-2 and Eqn. 2-3 definitions for mass flow $\dot{m}$ and mass flux j are shown. $\vec{u}_i$ is the velocity vector.

$$\dot{m}|_{t_{min}}^{t_{max}} = \frac{m_i}{t_{max} - t_{min}} \quad \left[\frac{kg}{s}\right] \qquad \textbf{Eqn. 2-2}$$

$$j|_{t_{min}}^{t_{max}} = \frac{m_i}{(t_{max} - t_{min})\, A_i} \quad \left[\frac{kg}{m^2 s}\right] \qquad \textbf{Eqn. 2-3}$$

To calculate spray mixing factors every particle is assigned to a cell on a two dimensional mesh with rectangular cells (in case of a circular cross section cells are squares). As mesh size a size similar to the polyhedron mesh is chosen.

In Figure 2-6 two meshes for a circular cross section are illustrated. There it is necessary to proof if one cell of the rectangular mesh has to be considered for calculation or not. For

this the distance from at least one node of the cell to the centre of the circle is smaller than the radius of the circle. To minimize errors due to the finite representation of the cell area, first a mesh with a finer step size (right picture in Figure 2-6) is made for particle assignment and area calculation. This fine mesh is summarized to a coarser mesh. It is obvious that the area covered by fine mesh is much smaller than area of coarser mesh.

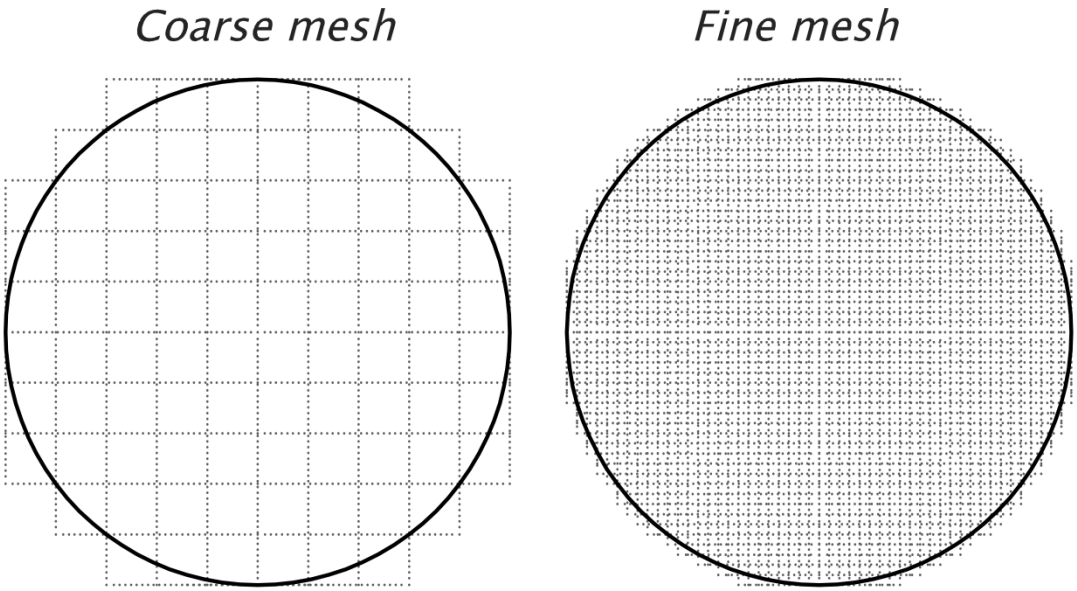

Figure 2-6: Influence of mesh size on area of cross section, only cells which are considered for calculation are depicted

2.2.1. Uniformity index

In the automotive industry for the calculation of homogeneity the uniformity index is widely used. The generic definition is given in Eqn. 2-4 and it was introduced by Weltens et al. [3].

$$\gamma = 1 - \frac{1}{2} \sum_{i=1}^{n} \frac{A_i \left|\phi_i - \overline{\phi}\right|}{\overline{\phi} \sum A_i} \qquad \textbf{Eqn. 2-4}$$

Here n is the total number of cells, A_i the area of cell i and ϕ any quantity for which the uniformity should be evaluated. Thus, γ is a linear deviation from an average value. If $\gamma \to 1$ the quantity is completely homogenous distributed; if $\gamma \to 0$ the quantity is completely inhomogeneously distributed. Instead of cell area A_i, often the volume or mass of each mesh cell is used for averaging.

Two uniformity indices for spray are typically evaluated: (i) γ_m (Eqn. 2-5) based on a mass per element (i.e., volume or are) quantity, and (ii) γ_j (Eqn. 2-6) based on the mass flux.

$$\gamma_m = 1 - \frac{1}{2} \sum_{i=1}^{n} \frac{A_i \, |m_i - \overline{m}|}{\overline{m} \, \sum A_i} \quad [-] \qquad \textbf{Eqn. 2-5}$$

$$\gamma_j = 1 - \frac{1}{2} \sum_{i=1}^{n} \frac{A_i \, |j_i - \overline{j}|}{\overline{j} \, \sum A_i} \quad [-] \qquad \textbf{Eqn. 2-6}$$

For both factors the mean value is calculated based on an area-averaging operation as shown in Eqn. 2-7.

$$\overline{\phi} = \frac{\sum \phi_i \, A_i}{\sum A_i} \qquad \textbf{Eqn. 2-7}$$

For gas mixing, the uniformity index is shown in Eqn. 2-8.

$$\gamma_g = 1 - \frac{1}{2} \sum_{i=1}^{n} \frac{V_i \, |x_i - \overline{x}|}{\overline{x} \, \sum V_i} \quad [-] \qquad \textbf{Eqn. 2-8}$$

Here, in contrast to the generic definition, A_i is substituted with V_i. As relevant mole fractions x, the values for the species NH_3 and $HNCO$ are most relevant in SCR applications.

2.2.2. Mixedness quality

The origin of this index goes back to Danckwerts [4]. He developed the definition originally for mixing of two mutually soluble liquids based on the local mass fraction. For the description of the degree of mixing, two quantities are used: they are (i) the scale of segregation and (ii) the intensity of segregation. The measure for the scale of segregation is analogous to the scale of turbulence in the statistical theory of turbulence.

Liscinsky et al. [5] [6] used parameters from Danckwerts [4] to describe mixing characteristics of experiments in an rectangular duct.

Sun et al. [7] introduced the parameter mixedness quality for spray mixing as a modification of the parameters presented in [5] and [6]. In [7] a numerical simulation of a spray in crossflow is performed, and the mixing of the spray is investigated. Unfortunately, it is not described in detail if the procedure detailed in Chapter 2.2 for a two dimensional mesh is used. To indicate the degree of mixing, a local number density of droplets per unit area denoted as c_i is defined (see Eqn. 2-9 adapted from [7]):

$$c_i = \frac{N_i}{A_i} \left[\frac{1}{m^2}\right] \qquad \textbf{Eqn. 2-9}$$

Here N_i is the number of droplets and A_i the area of the mesh cell i.

Based on this definition, the spatial unmixedness U_s is calculated using Eqn. 2-10 [7].

$$U_s = \frac{\sum_{i=1}^{n}\left(\frac{c_i}{c_{\max}} - \frac{\overline{c}}{c_{\max}}\right)^2}{n\,\frac{\overline{c}}{c_{\max}}\left(1-\frac{\overline{c}}{c_{\max}}\right)}\ [-] \qquad \textbf{Eqn. 2-10}$$

For the above calculation, the total cross-sectional area is first divided in *n* cells. For each cell the spatial concentration c_i is computed. $c_{\max}$ is the maximum of the c_i values from all cells and $\overline{c}$ is the ratio of total number of droplets N and total area A defined in Eqn. 2-11.

$$\overline{c} = \frac{N}{A}\ \left[\frac{1}{m^2}\right] \qquad \textbf{Eqn. 2-11}$$

If droplets are perfectly mixed $U_s \to 0$, and if perfectly unmixed $U_s \to 1$. While U_s is an indicator for the unmixedness of droplets in space, the diameter of the droplets, the size of each surface element A_i, as well as the speed of the droplets is not considered.

Chaikittisilp et al. [8] used a similar definition denoted as "degree of mixedness", which is shown in Eqn. 2-12. Here z_i is the number fraction of particles in each sampling cell.

$$DM = 1 - \frac{\sum_{i=1}^{n}(z_i - \overline{z})^2}{n\ \overline{z}\ (1-\overline{z})}\ [-] \qquad \textbf{Eqn. 2-12}$$

DM should not be confused with the degree of mixedness ξ defined in Chapter 2.2.3.

For the diameter distribution of the droplets the parameter U_d (diameter unmixedness) was defined [7]. Therefore, only c is substituted with the Sauter mean diameter (SMD) d_{32}, leading to Eqn. 2-13:

$$U_d = \frac{\sum_{i=1}^{n}\left(\frac{d_{32,i}}{d_{32,max}} - \frac{d_{32,whole}}{d_{32,max}}\right)^2}{n\,\frac{d_{32,whole}}{d_{32,max}}\left(1-\frac{d_{32,whole}}{d_{32,max}}\right)} \qquad \textbf{Eqn. 2-13}$$

d_{32} is defined as follows, and by using the volume of each droplet V_d and the surface area of each droplet A_d.

$$d_{32} = \frac{6\ \sum_{j=1}^{N} V_d}{\sum_{j=1}^{N} A_d}\ [m] \qquad \textbf{Eqn. 2-14}$$

$d_{32,i}$ is the SMD from mesh cell i, $d_{32,whole}$ from the whole cross-sectional area, and $d_{32,max}$ is the maximum $d_{32,i}$ of all cells.

Similar to U_s, the diameter unmixedness $U_d \to 0$ in case d_{32} is distributed completely homogeneously. $U_d \to 1$ in case d_{32} is distributed very inhomogeneously. This causes that

U_d can reach values higher than 1 because of some mesh cells having a lot of big droplets passing (and with that a high droplet volume and droplet surface) compared to other cells. This causes that smaller droplets in other mesh cells have nearly no influence on $d_{32,whole}$ because of their low volume and surface which leads to $d_{32,whole} \rightarrow d_{32,max}$. The denominator of Eqn. 2-13 may become zero, which leads to the limit of U_d being infinity as shown in Eqn. 2-15.

$$\lim_{\frac{d_{32,whole}}{d_{32,max}} \rightarrow 1} U_d = \frac{\sum_{i=1}^{n} \left(\frac{d_{32,i}}{d_{32,max}} - 1 \right)^2}{n \ 1 \ (1-1)} = \frac{\sum_{i=1}^{n} \left(\frac{d_{32,i}}{d_{32,max}} - 1 \right)^2}{0} = \infty \qquad \textbf{Eqn. 2-15}$$

This issue can be avoided by using of a cell averaged d_{32} instead of $d_{32,whole}$. This is shown in detail in Chapter 5.4.6.

U_s and U_d can be combined using a weighting factor ω to define a mixedness quality Q_m as shown in Eqn. 2-16 [7].

$$Q_m = \frac{\left(\omega \ (1 - U_s) + \ (1 - \omega) \ (1 - U_d) \right)}{2} \qquad \textbf{Eqn. 2-16}$$

In [7] ω was set to 0.5.

In Bai et al. [9] a modified version of U_s was used. The difference is that U_S was calculated with intensities of light I as following (based on Leong et al. [10]) as shown in Eqn. 2-17:

$$U_S = \frac{I_{var}}{I_{avg}(1 - I_{avg})} \quad with: I_{var} = \frac{1}{m \, n} \sum_{i=1}^{m} \sum_{j=1}^{n} \left(I(i,j) - I_{avg} \right)^2 \qquad \textbf{Eqn. 2-17}$$

m and n are number of lines and rows for the two dimensional mesh.

In [9] an experimental investigation of spray droplets in crossflow in a rectangular duct is made. Droplets are injected by a nozzle. Droplet velocities are measured with a particle image velocimetry (PIV) system at different cross sections. Measurement is made with 40 instantaneous images with five frames per second. With *MATLAB*® time averaged profiles are made.

The conclusions of [9] are that bigger counter rotating vortex pairs (CVP) increase mixing performance. The centrifugal forces lead to more droplets at the outer region of the vortex and less droplets in the centre. Many large droplets are near the wall and small droplets are located in the centre of the cross section.

2.2.3. Degree of mixedness

Bai et al. [11] made experiments with spray injected in a crossflow. They evaluate the mixedness with the degree of mixedness shown in Eqn. 2-18 [11].

$$\xi = 1 - \frac{\frac{1}{(n-1)}\sum_{i=1}^{n}(c_i - \overline{c})^2}{\overline{c}^2} \qquad \textbf{Eqn. 2-18}$$

c_i etc. are defined same as in Chapter 2.2.2, i.e., a local droplet number density based on the cell area was considered. The enumerator of the second term is the variance of the spatial droplet number density per unit area. Considering the denominator, ξ expresses the relative deviation from average the droplet number density $\overline{c}$. In case $\xi = 1$ droplets are perfectly mixed, while in case $\xi \to 0$ droplets are completely unmixed. Thus, ξ quantifies the degree of spatial mixedness of droplets.

This factor has the issue if c_i is much higher than $\overline{c}$ the denominator becomes very large. If, for example, $c_i = 10\,\overline{c}$ is $\frac{(c_i - \overline{c})^2}{\overline{c}^2} = 81$. In some practical applications of the above defined mixing index, it can occur that c_i for some cells is more than $10^3\,\overline{c}$, which leads to $\xi < 0$. An obvious explanation for this is that at cells with higher gas velocity more droplets pass the cell than at cells with lower gas velocity. Even if the droplet distribution is perfectly homogenous you get different number of droplets per cell (see Chapter 2.2.5). This is shown in Figure 2-7: in the left panel several Gaußian-distributed values for c_i with different standard deviations σ are shown. n indicates the cell number. In the right panel of Figure 2-7 the corresponding degree of mixedness is depicted. It can be seen that a very broad distribution (i.e., large values of σ) is required to get values smaller than 1. In this graph the magnitude of ξ is considered, because ξ becomes negative, which precludes a plot using a logarithmic scale.

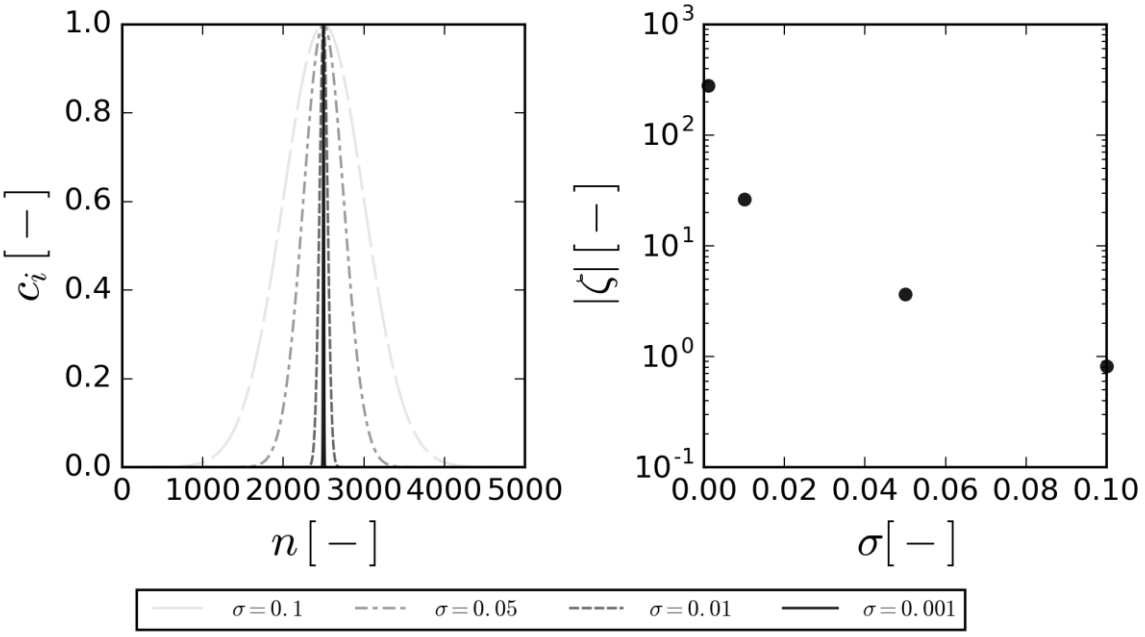

Figure 2-7: Degree of mixedness for several Gaußian distributed number density of droplets

2.2.4. Assessment of mixing parameters

Behaviour dependent on mesh size and evaluation duration for mixing parameters is made in Chapter 5.4.5.

2.2.5. Comparison with classical sampling theory

For collecting representative samples of a particle-lade gas stream isokinetic sampling must be performed (i.e., sample extraction has to be done with the same velocity as in the flow field, see Stieß [12]). Also, each sample has to have same gas volume. This requires a sample extraction procedure with (i) different sample extraction velocities, as well as (ii) different durations of the sampling procedure in case the flow field is not uniform.

This in contrast to the procedures summarized in Chapter 2.2 which are taken from the literature: in a perfectly homogenously distributed gas-particle flow each area element will experience different amounts of droplets, droplets mass etc. depending on the velocity profile in the cross section (it is assumed that droplets have same velocity than the fluid). This will lead to situations in which some of the mixing parameters defined in literature will indicate an inhomogeneous distribution although the gas-particle mixture is perfectly homogenous. Thus, care has to be taken when interpreting the results for such mixing quantities, because the not necessarily indicate the extent to which a uniform (mass-based) droplet concentration is achieved in the gas.

2.3. Flow quantities

2.3.1. Angular momentum and velocity

A very important metric in mixing theory is the angular momentum L. It is defined in Eqn. 2-19. It is the rotational analogue of linear momentum from a mass element m at spatial position $\vec{x}$ with velocity $\vec{u}$ around an axis defined with points $\vec{P}_1$ and $\vec{P}_2$. $\vec{L}_i$ is the angular momentum of the gas in cell i around the coordinate origin. $\vec{L}_i \cdot \vec{n}$ is the angular momentum around an axis defined by $\vec{P}_1$ and $\vec{P}_2$. Here N is the number of cells of the mesh.

$$L = \sum_{i=1}^{N} \underbrace{m \underbrace{(\vec{x} - \vec{P}_1)}_{radius} \times \vec{u}}_{\vec{L}_i} \cdot \underbrace{\frac{(\vec{P}_2 - \vec{P}_1)}{|\vec{P}_2 - \vec{P}_1|}}_{\vec{n}} \quad \left[\frac{kg\ m^2}{s}\right] \qquad \textbf{Eqn. 2-19}$$

Similar to the angular momentum is the angular velocity, or rotational speed ω. The relation between L and ω is shown in Eqn. 2-20.

$$\omega = \frac{L}{m\ R^2} \quad \left[\frac{Rad}{s}\right] \qquad \textbf{Eqn. 2-20}$$

Radius R is calculated in Eqn. 2-21. Figure 2-8 shows the used points and lengths. $\vec{n}_{P1P2}$ is the normal vector defined by $\vec{P}_1$ and $\vec{P}_2$.

$$R^2 = (\underbrace{|\vec{x} - \vec{P}_1|}_{H})^2 - \underbrace{\left((\vec{x} - \overrightarrow{P_1}) \cdot \underbrace{\frac{(\overrightarrow{P_2} - \overrightarrow{P_1})}{|\overrightarrow{P_2} - \overrightarrow{P_1}|}}_{\vec{n}_{P1P2}} \right)^2}_{C} \qquad \textbf{Eqn. 2-21}$$

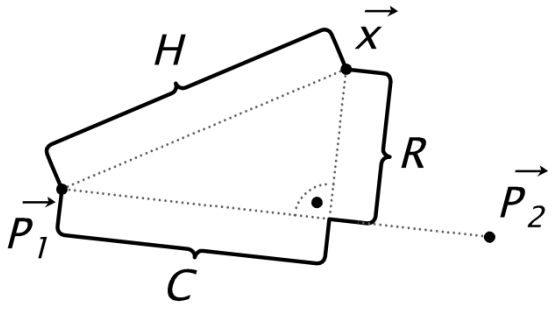

Figure 2-8: Vectors defined in Eqn. 2-21

2.3.2. Swirl number

A very common parameter in automotive industry is the swirl number. It comes from engine engineering and indicates the ratio of a fictitious anemometer speed n_f and the

swirl speed n_s as shown in Eqn. 2-22. It is the ratio of the rotational speed of the vortex and the exchange rate of the gas in a cylindrical volume V_{cyl}, i.e., it can be computed using $\frac{\dot{V}}{V_{cyl}}$. $\dot{V}$ is the volume flow on the inlet of the geometry.

$$\frac{n_s}{n_f} = \frac{\frac{30}{\pi}\overset{\left[\frac{rad}{s}\right]}{\tilde{\omega}}}{30\underbrace{\frac{\dot{V}}{V_{cyl}}}_{\left[\frac{1}{s}\right]}} \; [-] \qquad \textbf{Eqn. 2-22}$$

2.3.3. Mass balance

To ensure a meaningful simulation, the mass balance has to be checked. It is shown in Eqn. 2-23. This approach considers only gas phase and species H_2O, NH_3 and $HNCO$.

$$\dot{m}_{g,out} = \dot{m}_{g,in} + \dot{m}_{evap.} \qquad \textbf{Eqn. 2-23}$$

$\dot{m}_{g,out}$ is the mass flow rate of gaseous species at the outlet, $\dot{m}_{g,in}$ at the inlet and $\dot{m}_{evap.}$ is the mass-based evaporation rate in the investigated region. The wallfilm mass is neglected in the above balance, since its mass is negligibly small.

2.4. References

[1] C. Choi, Y. Sung, G. M. Choi, and D. J. Kim, "Numerical analysis of urea decomposition with static mixers in marine SCR system," *J. Clean Energy Technol.*, vol. 3, no. 1, pp. 39–42, 2015.

[2] G. Zheng, G. Palmer, G. Salanta, and A. Kotrba, "Mixer development for urea SCR applications," *SAE Tech. Pap.*, p. 2879, 2009.

[3] H. Weltens, H. Bressler, F. Terres, H. Neumaier, and D. Rammoser, "Optimisation of catalytic converter gas flow distribution by CFD prediction," in *SAE Technical Paper*, 1993.

[4] P. V Danckwerts, "The definition and measurement of some characteristics of mixtures," *Appl. Sci. Res. Sect. A*, vol. 3, pp. 279–296, 1952.

[5] D. S. Liscinsky, B. True, and J. D. Holdeman, "Experimental investigation of crossflow jet mixing in a rectangular duct," *NASA Tech. Memo.*, vol. 106152, 1993.

[6] D. S. Liscinsky, B. True, and J. D. Holdeman, "Mixing characteristics of directly opposed rows of jets injected normal to a crossflow in a rectangular duct," *NASA*

Tech. Memo., vol. 106477, 1994.

[7] H. Sun, B. Bai, J. Yan, and H. Zhang, “Single-jet spray mixing with a confined crossflow,” *Chinese J. Chem. Eng.*, vol. 21, pp. 14–24, 2013.

[8] W. Chaikittisilp, T. Taenumtrakul, P. Boonsuwan, W. Tanthapanichakoon, and T. Charinpanitkul, “Analysis of solid particle mixing in inclined fluidized beds using DEM simulation,” *Chem. Eng. J.*, vol. 122, pp. 21–29, 2006.

[9] B. F. Bai, H. Bin Zhang, L. Liu, and H. J. Sun, “Experimental study on turbulent mixing of spray droplets in crossflow,” *Exp. Therm. Fluid Sci.*, vol. 33, no. 6, pp. 1012–1020, 2009.

[10] M. Y. Leong, V. G. McDonell, and G. S. Samuelsen, “Mixing of an airblast-atomized fuel spray injected into a crossflow of air,” *NASA/CR*, vol. 2000–21046, 2000.

[11] B. Bai, H. Sun, H. Zhang, and L. Liu, “Numerical study on turbulent mixing of spray droplets in crossflow,” *J. Propuls. Power*, vol. 27, no. 1, pp. 132–143, 2011.

[12] M. Stieß, *Mechanische Verfahrenstechnik - Partikeltechnologie 1*. Springer, Berlin Heidelberg, 2009.

3. CFD models

This section provides an overview of governing equations used in CFD simulations of this master thesis. For the thesis the simulation code *AVL FIRE*® (**F**low **I**n **R**eciprocating **E**ngines*)* is used with *AVL FIRE Workflow manager v2014.2*® (later on called *FIRE*®). While droplets are tracked in a Lagrangian way, the gas flow is described in an Eulerian fashion using a finite volume approach. Specifically, the computational domain is discretised in a finite number of control volumes (mesh). For each cell of this mesh, the equations summarized in the following sections are applied.

If no separate reference is given, the equations were taken from the *AVL FIRE*® user guide.

3.1. Gas flow solver

This Chapter is based on AVL user guide for the CFD solver [1]. The basis are the fundamental conservation laws, which are approximated in the CFD solver.

These are (depicted in Einsteinian sum convention):

- Mass conservation: Equation of continuity [1]:

$$\frac{\partial \rho}{\partial t} + \frac{\partial}{\partial x_j}\left(\rho\, U_j\right) = 0 \qquad \textbf{Eqn. 3-1}$$

- Momentum conservation: Navier Stokes equation [1]:

$$\rho\, \frac{DU_i}{Dt} = \rho\, g_i - \frac{\partial p}{\partial x_i} + \frac{\partial}{\partial x_j}\left[\mu_{mol}\left(\frac{\partial U_i}{\partial x_j} + \frac{\partial U_j}{\partial x_i} - \frac{2}{3}\frac{\partial U_k}{\partial x_k}\,\delta_{ij}\right)\right] \qquad \textbf{Eqn. 3-2}$$

- Thermal energy conservation: First law of thermodynamics [1]:

$$\rho\, \frac{DH}{Dt} = \rho\, \dot{q}_g + \frac{\partial p}{\partial t} + \frac{\partial}{\partial x_i}\left(\tau_{ij}\, U_j\right) + \frac{\partial}{\partial x_j}\left(\lambda \frac{\partial T}{\partial x_j}\right) \qquad \textbf{Eqn. 3-3}$$

- Species conservation: Concentration equation [1]:

$$\rho\, \frac{DC}{Dt} = \rho\, \dot{r} + \frac{\partial}{\partial x_j}\left(D \frac{\partial C}{\partial x_j}\right) \qquad \textbf{Eqn. 3-4}$$

In Table 3-1 symbols in Eqn. 3-1 - Eqn. 3-4 are explained.

Symbol	Description
$\frac{D}{Dt}$	Material derivative $\left(\frac{D(\rho\,\phi)}{Dt} = \frac{\partial(\rho\,\phi)}{dt} + \frac{\partial(\rho\,\phi\,U_j)}{\partial x_j}\right)$
ρ	Fluid density $[kg/m^3]$
U_i, U_j, U_k	Instantaneous local velocities $[m/s]$
g_i	Gravity $[m/s^2]$
p	Local pressure $[Pa]$
μ_{mol}	Dynamic (molecular) viscosity $[Pa\ s]$
$\delta_{ij} = \begin{cases} 1 & if\ i = j \\ 0 & if\ i \neq j \end{cases}$	Kronecker delta $[-]$
τ_{ij}	Strain tensor $[N/m^2]$
λ	Thermal conductivity $[W/mK]$
T	Temperature $[K]$
C	Mass concentration of a species $[-]$
$\dot{r}$	Reaction rate $[1/s]$

Table 3-1: Symbols of CFD conservation laws

In practice (and when considering the so-called Reynolds-averaged set of equations) only ensemble-averaged values and their fluctuations can be computed. This is because the computational mesh, as well as the time step used for integration, is typically too large to resolve small-scale fluctuations. Therefore, ϕ is decomposed in a mean component $\overline{\Phi}$ and a fluctuating component ϕ' as in Eqn. 3-5.

$$\phi = \overline{\Phi} + \phi' \qquad \textbf{Eqn. 3-5}$$

With that, the Reynolds-averaged Navier Stokes equations (RANS) are derived (Eqn. 3-6):

$$\rho\,\frac{D\overline{U_i}}{Dt} = \rho\,g_i - \frac{\partial\overline{p}}{\partial x_i} + \frac{\partial}{\partial x_j}\left[\mu\left(\frac{\partial\overline{U_i}}{\partial x_j} + \frac{\partial\overline{U_j}}{\partial x_i} - \frac{2}{3}\frac{\partial\overline{U_k}}{\partial x_k}\,\delta_{ij}\right)\underbrace{-\rho\,\overline{U_i{}'U_j{}'}}_{R_{ij}}\right] \qquad \textbf{Eqn. 3-6}$$

Therein μ is the total dynamic viscosity as defined in Eqn. 3-7.

$$\mu = \mu_{mol} + \mu_{turb.} \qquad \textbf{Eqn. 3-7}$$

That RANS equations have new unknown variables. This causes the closure problem of the equation set. The most challenging part of the turbulence closure problem is the modelling of the turbulent stress tensor R_{ij}.

3.1.1. Turbulence model

To close the RANS equation set, a turbulence model is employed. At AVL the $k-\zeta-f$ model is state of the art, and was investigated and published by Hanjalic et al. [2].

For this model the eddy viscosity is represented by Eqn. 3-8 [1].

$$\nu_{turb.} = C_\mu \, \zeta \frac{k^2}{\epsilon} \quad with: \;\; \nu = \frac{\mu}{\rho} \qquad \textbf{Eqn. 3-8}$$

The set of model equations to predict the turbulence quantities *k*, ζ, and *f* are summarized in following set of equations.

- Transport equation for the turbulent kinetic energy (TKE) k [1]:

$$\rho \frac{Dk}{Dt} = \rho(P_k - \epsilon) + \frac{\partial}{\partial x_j}\left[\left(\mu + \frac{\mu_{turb.}}{\sigma_k}\right)\frac{\partial k}{\partial x_j}\right] \qquad \textbf{Eqn. 3-9}$$

- Transport equation for the turbulent energy dissipation ϵ [1]:

$$\rho \frac{D\epsilon}{Dt} = \rho \, \frac{C_{\epsilon 1}^* P_k - C_{\epsilon 2}\epsilon}{T} + \frac{\partial}{\partial x_j}\left[\left(\mu + \frac{\mu_{turb.}}{\sigma_k}\right)\frac{\partial \epsilon}{\partial x_j}\right] \qquad \textbf{Eqn. 3-10}$$

- Transport equation for the velocity scale ratio ζ [1]:

$$\rho \frac{D\zeta}{Dt} = \rho \, f - \rho \frac{\zeta}{k} P_k + \frac{\partial}{\partial x_j}\left[\left(\mu + \frac{\mu_{turb.}}{\sigma_\zeta}\right)\frac{\partial \zeta}{\partial x_j}\right] \qquad \textbf{Eqn. 3-11}$$

- Elliptic relaxation function for f [1]:

$$f - L^2 \frac{\partial^2 f}{\partial x_j \partial x_j} = \left(C_1 + C_2 \frac{P_k}{\zeta}\right)\frac{\frac{2}{3} - \zeta}{T} \qquad \textbf{Eqn. 3-12}$$

- Turbulent time scale T [1]:

$$T = \max\left(min\left(\frac{k}{\epsilon}, \frac{a}{\sqrt{6}\, C_\mu \, |S| \, \zeta}\right), \, C_\tau \left(\frac{\nu}{\epsilon}\right)^{\frac{1}{2}}\right) \qquad \textbf{Eqn. 3-13}$$

- Turbulent length scale L [1]:

$$L = C_L \max\left(min\left(\frac{k^{\frac{3}{2}}}{\epsilon}, \frac{k^{\frac{1}{2}}}{\sqrt{6}\, C_\mu\, |S|\, \zeta} \right),\ C_\eta \frac{\nu^{\frac{3}{4}}}{\epsilon^{\frac{1}{4}}} \right) \quad \textbf{Eqn. 3-14}$$

- $C_{\epsilon 1}$ [2]:

$$C_{\epsilon 1} = 1.4 \left(1 + \frac{0.012}{\zeta}\right) \quad \textbf{Eqn. 3-15}$$

- Damping of constant $C_{\epsilon 1}$ close to walls [1]:

$$C_{\epsilon 1}^{*} = C_{\epsilon 1} \left(1 + 0.045 \sqrt{\frac{1}{\zeta}}\right) \quad \textbf{Eqn. 3-16}$$

- Closure for the mean production of turbulent kinetic energy $[m^2/s\text{^}3]$ proposed by Durbin [3]:

$$P_k = 2 \frac{\mu_{turb.}}{\rho}\, S_{ij}\, S_{ji} \quad \textbf{Eqn. 3-17}$$

- Rate of strain tensor $[1/s]$ [3]:

$$S_{ij} = \frac{1}{2}\left(\frac{\partial U_j}{\partial x_i} + \frac{\partial U_i}{\partial x_j}\right) \quad \textbf{Eqn. 3-18}$$

- $|S|$ $[1/s]$ [3]:

$$|S| = \sqrt{S_{ij} S_{ji}} \quad \textbf{Eqn. 3-19}$$

In Table 3-2 the model constants for the $k - \zeta - f$ model are shown [2].

C_μ	$C_{\epsilon 2}$	C_1	C_2	σ_k	σ_ϵ	σ_ζ	C_τ	C_L	C_η
0.22	1.9	0.4	0.65	1	1.3	1.2	6	0.36	85

Table 3-2: Constants for turbulence model [2]

3.1.2. Wall treatment

At walls it has to be distinguished between two different boundary layers (BL). Near the wall a laminar BL exists which becomes a turbulent BL with increasing distance from wall. In the laminar BL the velocity increases rapidly with increasing distance from the wall. To reproduce the resulting very steep velocity gradient, a sufficiently fine computational grid near the wall would be needed in combination with a low Reynolds number turbulence model. For this a lot of cells and computation power would be needed.

To solve this issue, wall treatment models for the approximation of near wall velocity and temperature distribution are frequently employed. In this thesis, the hybrid wall treatment is used (see Eqn. 3-20). It is based on the work of Popovac and Hanjalic [4], and accounts for a gradual transition from a laminar to a turbulent BL.

With y^+ velocity U^+ can be calculated according Eqn. 3-20 [1] and Eqn. 3-21 [1] with the Von Karman constant $\kappa = 0.41$, and the additive constant E in the standard logarithmic wall law [4].

$$U^+ = y^+ e^{-\Gamma} + \frac{1}{\kappa} ln\,(E y^+) e^{-\frac{1}{\Gamma}} \qquad \textbf{Eqn. 3-20}$$

$$\Gamma = \frac{0.01\,(Pr\,y^+)^4}{1 + 5\,Pr^3\,y^+} \qquad \textbf{Eqn. 3-21}$$

In Eqn. 3-22 the normalized wall distance y^+ is shown with a normal distance of the cell centre to the wall denoted as Δn_p [4].

$$y^+ = \frac{C_\mu^{\frac{1}{4}}\, k^{\frac{1}{2}}\, \Delta n_p}{\nu} = \frac{y}{\nu} \underbrace{\sqrt{\frac{\tau_w}{\rho}}}_{u_\tau} \qquad \textbf{Eqn. 3-22}$$

3.1.3. Convection and radiation

Heat transport with convection and radiation is defined in Eqn. 3-23 [1].

$$\dot{q}_b = \underbrace{\alpha\,(T_e - T_0)}_{Convection} + \underbrace{\epsilon\,\sigma\,(T_r^4 - T_0^4)}_{Radiation} \qquad \textbf{Eqn. 3-23}$$

In Table 3-3 symbols in Eqn. 3-23 are defined.

Symbol	Description
α	Heat transfer coefficient $[W/m^2\,K]$
T_e	Environmental temperature $[K]$
T_0	Outer wall temperature $[K]$
ϵ	Outer wall emissivity $[-]$
σ	Stefan-Boltzmann constant $[W/m^2K^4]$
T_r	Environment radiation temperature $[K]$

Table 3-3: Symbols for heat transfer

3.2. Species transport

This Chapter is based on AVL user guide for the species transport module [5]. The transport model *General* is chosen for simulations. The resulting species transport equation is shown in Eqn. 3-24 [5].

$$\frac{\partial}{\partial t}(\rho\, w_k) + \frac{\partial}{\partial x_i}(\rho\, u_i\, w_k) = \frac{\partial}{\partial x_i}\left(\Gamma_{w_k}\frac{\partial w_k}{\partial x_i}\right) + S_{w_k} \qquad k = 1 \ldots K_{spec} \qquad \textbf{Eqn. 3-24}$$

w_k is the mass fraction of an individual chemical species k. K_{spec} is the total number of chemical species.

In the species transport equation Γ_{w_k} is defined as shown in Eqn. 3-25 [5].

$$\Gamma_{w_k} = \left(\rho D_{k,m} + \frac{\mu_{turb.}}{Sc_{turb.}}\right) \qquad \textbf{Eqn. 3-25}$$

Here $Sc_{turb.} = 0.7$ is the turbulent Schmidt number, and $D_{k,m}\left[\frac{m^2}{s}\right]$ is the diffusion coefficient of species k in the mixture.

The mass source S_{w_k} is defined in Eqn. 3-26 with reaction rate $k\left[\frac{kmol}{m^3 s}\right]$ and molar mass of species $MM_k\left[\frac{kg}{kmol}\right]$. Also terms for mass transfer and evaporation occur but they are not defined in detail in [5].

$$S_{w_k} = k\, MM_k \qquad \textbf{Eqn. 3-26}$$

Multi component diffusion is not taken into account.

3.3. Spray

This Chapter is based on AVL user guide for the spray module [6]. The calculations in spray module are based on the discrete droplet method (DDM) proposed by Dukowicz [7]. This method solves ordinary differential equations for the trajectory, momentum, heat and mass transfer of single droplets. Each droplet is in a group of non-interacting droplets called a "parcel". The vapour originating of evaporating droplets is a source term of an additional transport equation for the vapour fraction in an Eulerian formulation (see Chapter 3.2). Body forces are active on particles and liquid films forming at walls. Mass and heat coupling of the spray with the fluid domain was activated in all simulations done in this thesis. Particle interactions, wall interactions, breakup and virtual mass forces were not activated, though.

In Eqn. 3-27 the momentum equation for the droplets is shown (terms not considered in this thesis are not shown) [6].

$$m_d \frac{d\vec{u}_d}{dt} = \vec{F}_D + \vec{F}_G \qquad \textbf{Eqn. 3-27}$$

The drag force $\vec{F}_D$ is given in Eqn. 3-28 [6].

$$\vec{F}_D = \frac{1}{2}\rho_g A_d C_D |u_{rel}| u_{rel} \qquad \textbf{Eqn. 3-28}$$

Here A_d is the cross-sectional area of each droplet, and u_{rel} is the relative velocity of the droplet to the surrounding fluid.

The drag coefficient C_D is formulated following the often-used Schiller Naumann [8] correlation shown in Eqn. 3-29.

$$C_D = \begin{cases} \frac{24}{Re_d C_p}\left(1 + 0.15\, Re_d^{0.687}\right) & Re_d < 10^3 \\ \frac{0.44}{C_p} & Re_d \geq 10^3 \end{cases} \qquad \textbf{Eqn. 3-29}$$

The particle Reynolds number is shown in Eqn. 3-30 [6].

$$Re_d = \frac{\rho_g |u_{rel}| D_d}{\mu_g} \qquad \textbf{Eqn. 3-30}$$

In the case of small particles the Cunningham correction factor C_p [9] shown in Eqn. 3-31 and based on the Knudsen number Kn reduces the drag coefficient.

$$C_p = 1 + Kn_p\left(2.492 + 0.84 e^{-\frac{1.74}{Kn_p}}\right) \qquad \textbf{Eqn. 3-31}$$

Kn is defined in Eqn. 3-32. It is the ratio of mean free path λ and a representative physical length scale, in this case droplet diameter D_d [6].

$$Kn = \frac{\lambda}{D_d} \qquad \textbf{Eqn. 3-32}$$

Mean free path length λ in gaseous phase can be calculated with Eqn. 3-33 [6].

$$\lambda = \frac{k_b T_g}{\sqrt{2}\,\pi d_g^2 p_g} \qquad \textbf{Eqn. 3-33}$$

There k_b is the Boltzmann constant and $d_g = 2.8 \cdot 10^{-10}\ [m]$ is the molecule diameter in gas phase.

$\vec{F}_G$ in Eqn. 3-34 represents effects of gravity and buoyancy due to a hydrostatic pressure gradient [6].

$$\vec{F}_G = V_p(\rho_p - \rho_g)g \quad \textbf{Eqn. 3-34}$$

Pressure force given in Eqn. 3-35 [6] is NOT considered in calculations for this thesis.

$$\vec{F}_{ip} = -V_p \cdot \nabla p \quad \textbf{Eqn. 3-35}$$

3.3.1. Evaporation model

For the calculations the SCR-thermolysis model is used. It is modelled as a two-step process following the PhD thesis of Birkhold [10]. This consists of pure water evaporation until the drop is composed of urea only, and a subsequent thermolysis reaction of urea to form NH_3 and $HNCO$.

When modeling evaporation of water and the thermolysis of urea, the processes are described independently. Evaporation rates are calculated based on Abramzon and Sirignano [11], and the extension "Multi component evaporation model" developed by Brenn et al [12].

Therein, the mass flow for component i is calculated according to Eqn. 3-36. Overbars indicate that values are average values over components. $\overline{D}_{g,i}$ is the binary diffusion coefficient of component *i* in the gas [6].

$$\dot{m}_i = \pi\, \overline{\rho}_g\, \overline{D}_{g,i}\, D_d\, Sh_i^*\, \ln(1 + B_{Y,i}) \quad \textbf{Eqn. 3-36}$$

The Spalding number $B_{Y,i}$ is evaluated via Eqn. 3-37 with concentrations of component i at the droplet surface (denoted with subscript s) and at external gas flow (denoted with subscript ∞) [6].

$$B_{Y,i} = \frac{w_{i,s} - w_{i,\infty}}{1 - w_{i,s}} \quad \textbf{Eqn. 3-37}$$

The sum of $\dot{m}_i$ gives the total mass transfer rate of evaporation (Eqn. 3-38) [6].

$$\dot{m} = \sum_{i=1}^{N} \dot{m}_i \quad \textbf{Eqn. 3-38}$$

The total mass transfer rate can also be calculated from the energy balance shown in Eqn. 3-39 with the average thermal conductivity $\overline{\lambda}_g$ and vapour specific heat in the film $\overline{c}_{p,f}$ [11].

$$\dot{m} = \pi \frac{\overline{\lambda}_g}{\overline{c}_{p,f}} D_d \, Nu^* \ln(1 + B_T) \quad \textbf{Eqn. 3-39}$$

B_T is shown in Eqn. 3-40 [6] and ϕ in Eqn. 3-41 [6].

$$B_T = (1 + B_Y)^{\phi} - 1 \quad \textbf{Eqn. 3-40}$$

$$\phi = \frac{\overline{c}_{p,f}}{\overline{c}_{p,g}} \frac{Sh^*}{Nu^*} \frac{1}{Le} \quad \textbf{Eqn. 3-41}$$

Le is here the Lewis number (Eqn. 3-42). It is the ratio between the heat diffusivity and the molecular diffusivity of the vapour in the ambient gas.

$$Le = \frac{\lambda}{\rho \, c_p \, D} = \frac{Sc}{Pr} \quad \textbf{Eqn. 3-42}$$

F_T and F_M are correction factors for the film thickness of the non evaporating droplet and calculated with Eqn. 3-43 [6]:

$$F(B) = (1 + B)^{0.7} \frac{\ln(1 + B)}{B} \quad \textbf{Eqn. 3-43}$$

which are subsequently used to calculate the Nu and Sh numbers using the correlations shown in Eqn. 3-44 [6] and Eqn. 3-45 [6].

$$Nu^* = 2 + \frac{Nu_0 - 2}{F_T}, \qquad Nu_0 = 2 + 0.552 \, Re^{\frac{1}{2}} Pr^{\frac{1}{3}} \quad \textbf{Eqn. 3-44}$$

$$Sh^* = 2 + \frac{Sh_0 - 2}{F_M}, \qquad Sh_0 = 2 + 0.552 \, Re^{\frac{1}{2}} Sc^{\frac{1}{3}} \quad \textbf{Eqn. 3-45}$$

The heat transfer rate to the droplet is depicted in Eqn. 3-46 [6] with latent heat of evaporation $\overline{L}$.

$$\dot{Q}_S = \dot{m} \left(\frac{\overline{c}_{p,f} \, (T_\infty - T_S)}{B_T} - \overline{L}(T_S) \right) \quad \textbf{Eqn. 3-46}$$

The final algorithm to calculate the heat and mass transfer follows as [6]:

1. Get the average physical properties $\overline{\rho}$, $\overline{c}_{p,f}$, $\overline{c}_{p,g}$, $\overline{\lambda}_g$, $\overline{D}_{g,i}$
2. Calculate Nu_0 and Sh_0
3. Get $B_{Y,i}$, F_M, Sh^* and $\dot{m}$ from Eqn. 3-36
4. Guess the value of B_T by using the value from the previous iteration or time step
5. Calculate the modified Nussel number Nu^* and correct the heat transfer number B_T by comparing the two mass transfer rates from equations Eqn. 3-36 and Eqn. 3-39

If the correction of B_T is too large go back to step 4.

6. Calculate the heat transfer by Eqn. 3-46

Real gas behaviour for calculating the mixture fractions and mixture properties at the droplets surface is taken into account by using the activity coefficient concept. Specifically, the activity coefficients γ_i are calculated using the UNIFAC method, and as shown in Eqn. 3-47 [6] the gas partial pressure $p_{v,i}$ of component i can then be used to calculate the equilibrium mole fractions in the gas phase.

$$x_{i,s} = x_{i,l}\,\gamma_i \frac{p_{v,i}}{p} \qquad \textbf{Eqn. 3-47}$$

The above equations describe the evaporation from the water-urea solution. In *FIRE*® wall film module [13] (see Chapter 3.4) is indicated that thermolysis starts if water mass fraction is less than 5 %. However, in *FIRE*® spray module [6] it is indicated that the droplet is completely solid, i.e., made of urea only when starting thermolysis. Then, in accordance with Birkhold [10] reaction R 8 is taken into account for modelling the thermolysis behavior.

$$(NH_2)_2CO(s\ or\ l) \xrightarrow{\Delta H=+185.5\frac{kj}{mol}} NH_3(g) + HNCO(g) \qquad \textbf{R 8}$$

The reaction rate is calculated following Eqn. 3-48 from Birkhold et al. [14] with $A = 0.42\ \left[\frac{kg}{m\ s}\right]$ and $E_a = 6.9 \cdot 10^4\ \left[\frac{J}{mol}\right]$.

$$\frac{dm_{Urea}}{dt} = -\pi\ A\ D_d\ \exp\left(-\frac{E_a}{RT}\right)\ \left[\frac{kg\ m^2}{s}\right] \qquad \textbf{Eqn. 3-48}$$

3.3.2. Turbulent dispersion model

From particles suspending in a turbulent flow it is assumed that they interact with the individual turbulent eddies. Each interaction deflects the particle as dictated by the instantaneous velocity of the turbulent eddy and particle inertia. These additional turbulence effects on spray particles cannot be resolved by the ensemble-averaged flow field obtained from a RANS-based simulation. Thus, a turbulent dispersion model is frequently used in such simulations.

In the stochastic dispersion method from Gosman and Ioannides [15] the effects of turbulence on spray particles (or droplets) are modelled by adding a fluctuating velocity u_{ig}.

Assuming isotropic turbulence, the components of the particle fluctuating velocity $\vec{u}_i'$ is determined by sampling randomly from a Gaussian distribution (Eqn. 3-49 [6]) with standard deviation $\sigma = \sqrt{\frac{2k}{3}}$ where k is the turbulent kinetic energy of the gas at the particle location.

$$\vec{u}_i' = \left(\frac{2}{3}k\right)^{\frac{1}{2}} sign(2Rn_i - 1)\ \mathrm{erf}^{-1}(2Rn_i - 1) \qquad \textbf{Eqn. 3-49}$$

Rn_i is a random number from $[0 < Rn_i < 1]$ for each vector component and erf^{-1} is the inverse Gauss function.

$\vec{u}_i'$ is chosen as piecewise constant function of time, and is only updated when the turbulence correlation time $t_{turb.}$ has passed. $t_{turb.}$ is the minimum of the eddy break up time and the time needed for a particle to traverse an eddy. It is calculated according to Eqn. 3-50 [6] with $C_\tau = 1$ and $C_1 = 0.16432$. ϵ is the dissipation rate.

$$t_{turb.} = \min\left(C_\tau \frac{k}{\epsilon},\ \ C_1 \frac{k^{\frac{3}{2}}}{\epsilon} \frac{1}{\left|\vec{u}_g + \vec{u}' - \vec{u}_d\right|}\right) \qquad \textbf{Eqn. 3-50}$$

If $t_{turb.}$ is smaller than the computational time step Δt, the spray integration time step is reduced to $t_{turb.}$.

3.4. Wallfilm

This Chapter is based on the AVL user guide for the wall film module [13].

3.4.1. Fundamental assumptions underlying the model

In the *FIRE*® wall film model the following fundamental assumptions and modelling approaches are considered [13]:

- Gas and wall film flow are treated as two separate single phases
- Film thickness is very small in relation to the mean diameter of the gas flow
- The wavy surface of the film is not simulated in detail but modelled via a mean film thickness with a superimposed film roughness
- The mean film surface is assumed to be parallel to the wall
- Wall friction and interfacial shear stress dominate film behaviour
- The wall temperature is below the Leidenfrost point

The above assumptions lead to an implementation of the wall film model as a 2D finite volume method on the wall boundaries of the air flow geometry.

3.4.2. Simulation settings

Solution flags wall shear, TKE, heat transfer, temperature, evaporation, entrainment, balancing, splashing and momentum equation were activated. Coupling flags momentum source, vapour mass source and vapour energy source were enabled in all simulations.

3.4.3. Governing equations

The basic equation that describes wall film flow is the film thickness equation. It is a slightly modified formulation of the continuity equation. For simplicity, only the Cartesian formulation of the film thickness equation is shown in Eqn. 3-51 [13] with the film thickness denoted as δ.

$$\frac{\partial \delta}{\partial t} + \frac{\partial \delta u_i}{\partial x_i} + \frac{\partial \delta u_j}{\partial x_j} = \frac{1}{\rho A} \underbrace{(S_{mD} - S_{mV})}_{source\ term} \qquad \textbf{Eqn. 3-51}$$

In Eqn. 3-52 [13] the momentum balance equation of the wall film is given. For simplicity incompressibility of the liquid making up the film is assumed.

$$\frac{\partial}{\partial t}\vec{u}_f + (\vec{u}_f \cdot \nabla)\vec{u}_f = -\nabla \frac{p}{\rho_0} + \frac{\mu}{\rho_0}\Delta \vec{u}_f + \vec{S}_f \qquad \textbf{Eqn. 3-52}$$

The enthalpy balance is shown in Eqn. 3-53 [13]. It takes convective heat transfer within the film, as well as all essential heat transfer mechanisms into account.

$$\frac{\partial h_i}{\partial t}\Delta V\, \rho_f + \rho_f \sum_j h_i\, \vec{u}_f\, d\vec{s}_{ij} = \dot{H}_{s,wf} - \dot{H}_{s,fg} - \dot{m}_{ev}\, h_{ev} + \dot{H}_{s,imp} + \dot{H}_{s,ent} \qquad \textbf{Eqn. 3-53}$$

In Table 3-4 symbols for Eqn. 3-53 are explained in closer detail.

Symbol	Description
$\frac{\partial h_i}{\partial t} \Delta V \, \rho_f$	Change of energy stored in film $[W]$
$\rho_f \sum_j h_i \, \vec{u}_f \, d\vec{s}_{ij}$	Convective heat transfer within the film $[W]$
$\dot{H}_{s,wf}$	Heat transfer from the wall to the film $[W]$
$\dot{H}_{s,fg}$	Heat transfer between film and gas $[W]$
$\dot{m}_{ev} \, h_{ev}$	Enthalpy transfer due to the latent heat that is consumed during evaporation $[W]$
$\dot{H}_{s,imp}$	Enthalpy transfer via spray droplet impingement $[W]$
$\dot{H}_{s,ent}$	Enthalpy loss via droplet entrainment $[W]$

Table 3-4: Symbols of wall film enthalpy equation

3.4.1. Entrainment

At high air velocity, the shear force at the film surface tears droplets back into the air flow. These droplets are generated at, or near surface waves. This is described with the entrainment model. In this thesis the Schadel-Hanratty model is used. In this model the critical Weber number is calculated according to Eqn. 3-54 [13]. The Weber number is the ratio of fluid inertia compared to its surface tension σ and the average film velocity $\overline{u}_f$.

$$We_{cr,SH} = \frac{\rho_g \left| \overline{u}_{gas} - \overline{u}_f \right|^2 \rho}{\sigma} \qquad \textbf{Eqn. 3-54}$$

If $We_{cr,SH} \geq 17$ first droplets start to entrain. This entrainment model generates only a mass flux that leaves the wall film. Hence, it acts as a mass sink to the film, and as a mass source for the spray. When introducing new droplets to the spray, a droplet diameter has to be chosen. Therefore, a volume mean diameter $D_{vm,K}$ is calculated following Kataoka et al. [16], i.e., using Eqn. 3-55 and Eqn. 3-56.

$$D_{vm,K} = 0.028 \frac{\sigma}{\rho_g \, \overline{u}_g^2} \, Re_{f,IM}^{-1/3} \, Re_g^{2/3} \left(\frac{\rho_g}{\rho_f} \right)^{-1/3} \left(\frac{\mu_g}{\mu_f} \right)^{2/3} \qquad \textbf{Eqn. 3-55}$$

$$Re_{f,IM} = \frac{4 \, \overline{u}_f \, \delta}{\nu_f} \qquad \textbf{Eqn. 3-56}$$

3.4.2. Evaporation

The SCR-thermolysis model discussed in Chapter 3.3.1 is chosen.

3.4.1. Splashing

This section describes the splashing model by Kuhnke [17] which is used in this thesis for the description of impingement of droplets from the spray onto the wall. It takes into account the wall temperature T_W. K given in Eqn. 3-57 [13] is the dimensionless droplet velocity and a characteristic quantity which serves to distinguish between different impingement regimes – it is used as the key parameter for the splashing model.

$$K = \frac{(\rho_d \, d_d)^{3/4} \, u_{d,n}^{5/4}}{\sigma_d^{1/2} \, \mu_d^{1/4}} \qquad \textbf{Eqn. 3-57}$$

Therein is $u_{d,n}$ the droplet velocity normal to the wall.

The model has four regimes:

- Deposition
- Splash
- Rebound
- Thermal breakup

3.5. Thin walls

This Chapter is based on AVL user guide for the thin walls module [18]. In this thesis, the option "normal heat conduction" in *FIRE*® is used: in a multi layered wall transient one-dimensional heat conduction is solved, and the direction normal to the wall is considered only. Thus, for each homogeneous wall layer the temperature profile is described using the heat balance equation shown in Eqn. 3-58.

$$\frac{\partial T}{\partial t} - \frac{\lambda}{\rho \, c_p} \frac{\partial^2 T}{\partial x^2} = 0 \qquad \textbf{Eqn. 3-58}$$

On the interface between layers i and j Eqn. 3-59 is valid.

$$\lambda_i \left.\frac{\partial T}{\partial x}\right|_i = \lambda_j \left.\frac{\partial T}{\partial x}\right|_j \qquad \textbf{Eqn. 3-59}$$

x is the coordinate in the direction normal to the wall.

For heat transfer see 3.1.3.

3.6. References

[1] AVL List GmbH, “FIRE v2014.2 – CFD solver.”

[2] K. Hanjalic, M. Popovac, and M. Hadziabdic, “A robust near-wall elliptic-relaxation eddy-viscosity turbulence model for CFD,” *Int. J. Heat Fluid Flow*, vol. 25, pp. 1047–1051, 2004.

[3] P. A. Durbin, “On the k-3 stagnation point anomaly,” *Int. J. Heat Fluid Flow*, vol. 17, pp. 89–90, 1996.

[4] M. Hanjalic and K. Popovac, “Compound wall treatment for RANS computation of complex turbulent flows and heat transfer,” *Flow Turbul. Combust*, vol. 78, pp. 177–202, 2007.

[5] AVL List GmbH, “FIRE v2014 – species transport module,” no. 08.0205.2014.

[6] AVL List GmbH, “FIRE v2014.2 – spray module,” no. 08.0205.2014.2.

[7] J. K. Dukowicz, “A particle-fluid numerical model for liquid sprays,” *J. Comput. Phys.*, vol. 35, pp. 229–253, 1980.

[8] L. Schiller and A. Naumann, “Über die grundlegenden Berechnungen bei der Schwerkraftaufbereitung,” *VDI*, vol. 77, no. 12, pp. 318–320, 1933.

[9] E. Cunningham, “On the velocity of steady fall of spherical particles through fluid medium,” *Proc. R. Soc. London. Ser. A, Contain. Pap. a Math. Phys. Character*, vol. 83, no. 563, pp. 357–365, 1910.

[10] F. Birkhold, “Selektive katalytische Reduktion von Stickoxiden in Kraftfahrzeugen : Untersuchung der Einspritzung von Harnstoffwasserlösung,” 2007.

[11] B. Abramzon and W. A. Sirignano, “Droplet vaporization model for spray combustion calculations,” *Int. J. Heat Mass Transf.*, vol. 32, no. 9, pp. 1605–1618, 1989.

[12] G. Brenn, L. J. Deviprasath, and F. Durst, “v,” in *Proc. 9th Int. Conf. Liquid Atomiz. Spray Syst.(ICLASS), Sorrento (Italy)*, 2003.

[13] AVL List GmbH, “FIRE v2014.2 – wall film module,” no. 08.0205.2014.2.

[14] F. Birkhold, U. Meingast, and P. Wassermann, “Analysis of the Injection of urea-water-solution for automotive SCR deNOx-systems : modeling of two-phase flow and spray/wall-interaction,” *SAE Tech. Pap.*, no. 2006-01–0643, 2006.

[15] A. D. Gosman and E. Loannides, “Aspects of computer simulation of liquid-fueled combustors,” *J. Energy*, vol. 7, no. 6, pp. 482–490, 1983.

[16] I. Kataoka, M. Ishii, and K. Mishima, “Generation and size distribution of droplet in annular two-phase flow,” *J. Fluids Eng.*, vol. 105, pp. 230–238, 1983.

[17] D. Kuhnke, “Spray/wall interaction modelling by dimensionless data analysis,” Darmstadt, 2004.

[18] AVL List GmbH, “FIRE v2014.2 – thin walls module,” no. 08.0201.2014.

4. Simulation settings

In this Chapter simulation settings for all simulations are listed. These are operation conditions, spray properties, simulation setup and boundary conditions.

4.1. Operating conditions

For the simulation of marine Diesel engines three different operation modes are from interest. They are summarized in Table 4-1.

	Mode 1	**Mode 2**	**Mode 3**
$\dot{m}\ \left[\frac{kg}{s}\right]$	3.61	2.78	1.25
$u_g\ \left[\frac{m}{s}\right]$ (circular chan.)	31.22	23.81	11.70
$u_g\ \left[\frac{m}{s}\right]$ (square chan.)	24.52	18.71	9.19
$T\ [°C]$	320.00	315.00	370.00
$p_{out}\ [bar]$	1.00	1.00	1.00
$T_{env}\ [°C]$	35.00	35.00	35.00
$\alpha\ \left[\frac{W}{m^2K}\right]$	7.50	7.50	7.50
$\epsilon\ [-]$	0.95	0.95	0.95
$T_{UWL}\ [°C]$	21.00	21.00	21.00
$\frac{\dot{n}_{NH3}}{\dot{n}_{NOX}}\ [-]$	0.95	0.95	0.95
$\dot{m}_{UWL}\ \left[\frac{g}{s}\right]$	10.00	7.00	2.00

Table 4-1: Operation modes of marine Diesel engines

The urea water solution has a urea mass fraction of urea $w_{UR} = 0.4$ for all modes.

For customers, a good mixing quality at low pressure loss is necessary. A typical benchmark for this is a pressure difference of $\Delta p < 300\ [Pa]$.

4.2. Spray characteristics

In the simulation an air assisted injector will be approximated with spray particles injected with a given particle density distribution and an air stream. The distribution is depicted in

Figure 4-1. A q_1 distribution is used because for the simulations a distribution based on measurements is available. The breakup of the injected liquid jet itself is not computed, since it would not be possible to resolve key breakup phenomena with the computational mesh.

For the injection of spray particles a single hole nozzle is used. The injection positions and velocities of the particles are computed with the nozzle dimensions depicted in Figure 4-2. The particles are injected without swirl. A full cone spray is used with dimensions according to Table 4-2.

Quantity	Dimension
$u_{s,start}\ \left[\frac{m}{s}\right]$	10.00
$d\ [mm]$	0.00
$D\ [mm]$	0.15
α [°]	0.00
β [°]	7.50

Table 4-2: Spray data

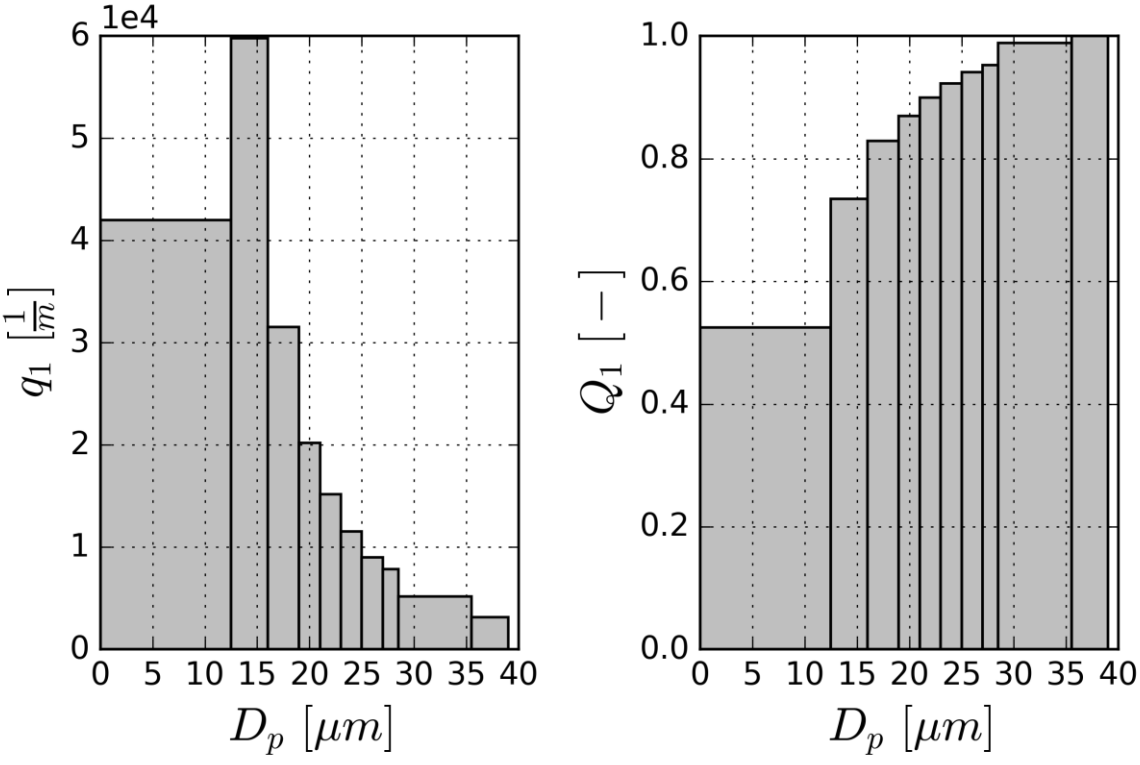

Figure 4-1: Number distributions of spray particles at injection

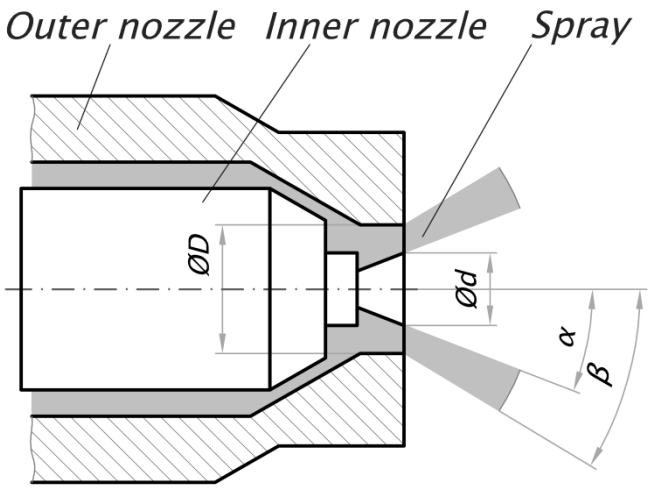

Figure 4-2: Nozzle dimensions

4.3. Simulation setup

For the simulations the modules *Species* and *Thin walls* were activated; for spray simulations the additional modules *Spray* and *Wallfilm* were activated as well. In the domain the species N_2, O_2, $HNCO$, NH_3 and H_2O were defined. Body force is activated as well.

4.3.1. Timestep

An important number in CFD simulations is the Courant-Friedrichs-Lewy number (CFL). Its definition is shown in Eqn. 3-1.

$$CFL = \frac{u\ \Delta t}{\Delta x} \qquad \textbf{Eqn. 4-1}$$

In Table 4-3 the timesteps and CFL number for an average cell size of $\Delta x = 6.9\ [mm]$ and a typical velocity of $u = 200\ [m/s]$ for chosen for simulations are indicated.

Simulation	Δt	CFL
Gas flow $[s]$	0.01	288.90
Spray flow $[s]$	0.001	28.89

Table 4-3: Timesteps

The maximum CFL number was not recorded, and hence could not be reported.

4.3.2. Thin wall module

In the module *Thin Walls* one dimensional heat conduction for the pipe wall is computed. For this two layers for the wall are defined in Table 4-4.

Quantity	Pipe wall	Insulation
$Thickness\ [mm]$	5.00	50.00
$\lambda\ \left[\frac{W}{m\ K}\right]$	15.00	0.10

Table 4-4: Thin wall definitions

4.3.3. Summary of active equations

In Table 4-5 a summary of the equations of the CFD solver that were activated during the simulation is provided.

Active Equations	Status
Momentum	yes
Turbulence model	$k-\zeta-f$
Energy	yes
Enthalpy	total enthalpy
Pressure work	no
Scalar (for passive scalar)	no
Two stage pressure correction	no
Compressibility	yes
Wall treatment	hybrid wall treatment
Heat transfer wall model	standard wall function

Table 4-5: Active equations

4.3.4. Differencing schemes

In Table 4-6 settings for the differencing schemes are depicted. A blending factor of 0.6 means that 60 % of the chosen and 40 % of the upwind discretization procedure will be used for the calculation. In case of different settings for the simulations, this will be indicated in the corresponding Chapter.

	Procedure	Blending factor
Momentum	MINMOD relaxed	1
Continuity	Central differencing	1
Turbulence	Upwind	-
Energy	Upwind	-
Scalar	Upwind	-

Table 4-6: Differencing scheme

4.3.5. Boundary conditions

In Table 4-7 common boundary conditions are depicted. Additional boundary settings are specified in the corresponding Chapter.

	Inlet	Outlet	Cylinder
Boundary condition	velocity	p_{out}	wall
$w_{O2}\ [-]$	0.76	-	-
$w_{N2}\ [-]$	0.24	-	-
Turbulence intensty $[\%\ of\ u_g]$	1.00	-	-
Turb. length scale $[m]$	0.05	-	-
Convection	-	-	α, T_{env}
Radiation	-	-	ϵ, T_{env}

Table 4-7: Common boundary conditions

For the outlet an average pressure boundary condition was chosen. The definition is shown in Eqn. 4-2. The pressure for each face i can be less or more than the average pressure; however, only the average pressure p_{out} is fixed.

$$p_{out} = \frac{1}{\sum A_i} \sum_{i=1}^{n} p_i A_i \qquad \textbf{Eqn. 4-2}$$

5. Flow across an inclined plate

As a reference for mixer design, a well-known geometry is chosen: a simple inclined plate in a circular tube. This configuration has very good mixing properties at very low backpressure. With this geometry a spray simulation is made and mixing parameters, detailed in Chapter 2.2, will be compared and investigated.

5.1. Geometry and meshing

In Figure 5-1 the geometry of the inclined plate is depicted. It consists of a circular tube with an inclined plate as mixer. At the inlet position of the injector a mesh with length C was embedded to improve flow property predictions (this will be discussed in detail in Chapter 5.1.1). In Table 5-1 dimensions of the geometry are indicated. The spray and the air stream for approximating an air assisted nozzle is injected at origin of coordinate system.

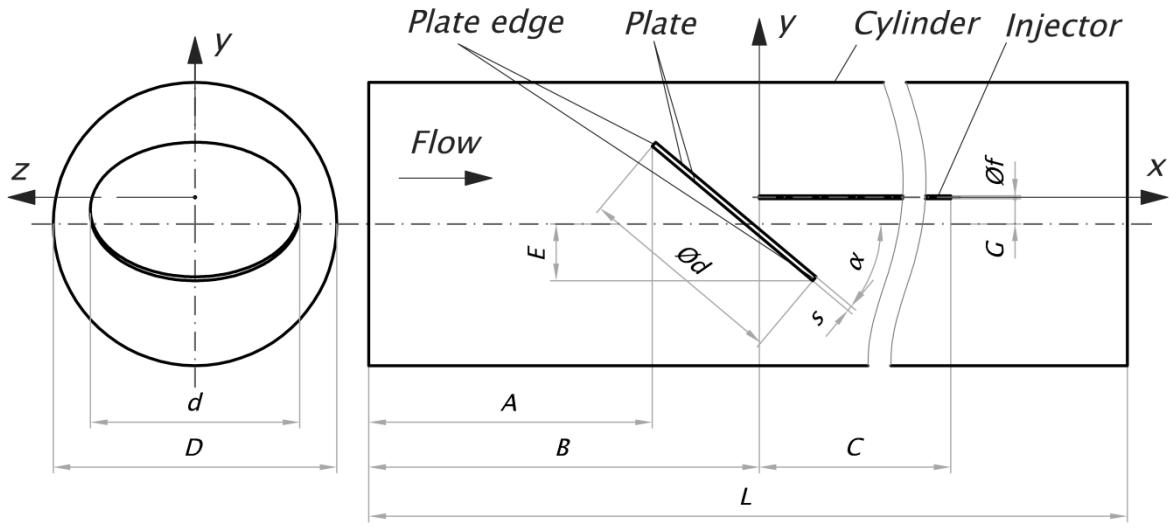

Figure 5-1: Geometry of inclined plate

$A\ [m]$	0.500	$f\ [m]$	0.005
$B\ [m]$	0.689	$G\ [m]$	0.045
$C\ [m]$	2.000	$s\ [m]$	0.009
$D\ [m]$	0.500	$L\ [m]$	3.000
$d\ [m]$	0.369	$\alpha\ [°]$	40
$E\ [m]$	0.100		

Table 5-1: Dimensions of inclined plate

5.1.1. General considerations

The mesh was generated with *AVL FAME M polymesher v2016*® (later on called *FAME M*®) as a polyhedron mesh. The air flow of the injector has a much higher velocity than the main flow. This would cause a very fast spread of the injector stream because of numerical diffusion. This effect is depicted in Figure 5-2. Using a hexahedron mesh one can orientate the mesh direction in the flow direction such numerical diffusion has no effect normal to the main flow. Unfortunately, this is not the case for polyhedron mesh cells, which are inhomogeneously and randomly orientated. In these mesh configurations, flows with large velocity gradients between cells "diffuses" very fast, since the normal direction of the cells is not orientated in the main flow direction. On can see this phenomenon in the grey cells in Figure 5-2 which indicate that they are flow affected.

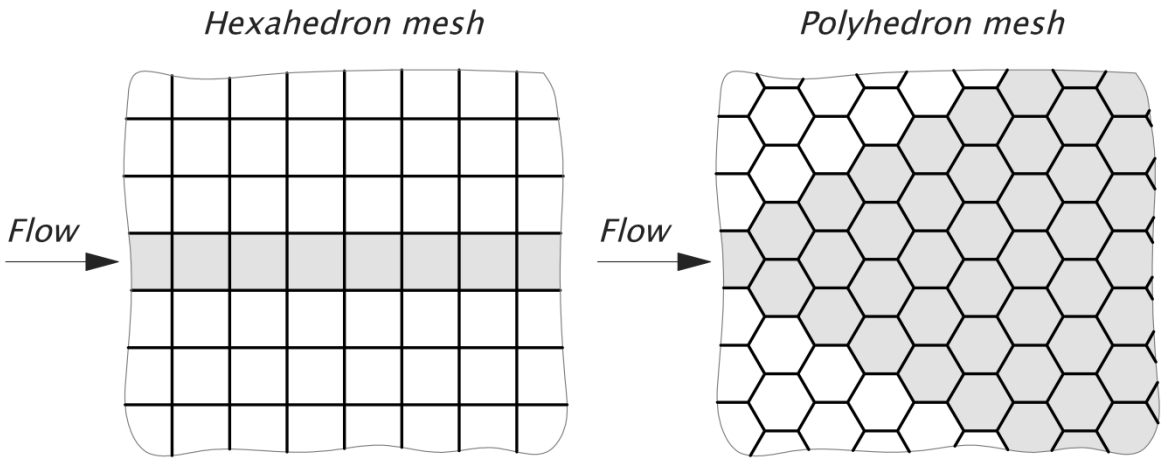

Figure 5-2: Schematic comparison of hexahedron and polyhedron mesh with respect to numerical diffusion

To reduce this effect, the mesh is generated in two parts: the cylinder mesh and the injector mesh. Every of the two meshes has on the interface two boundary layers with nearly prismatic cells. This leads to a much reduced effect of numerical diffusion. The two parts are connected with the command *Conform connect* in *FIRE*®. For this it is required that the two meshes have completely same nodes on the interface. The command recognizes two different nodes which are within a specified tolerance and merge them to one common node.

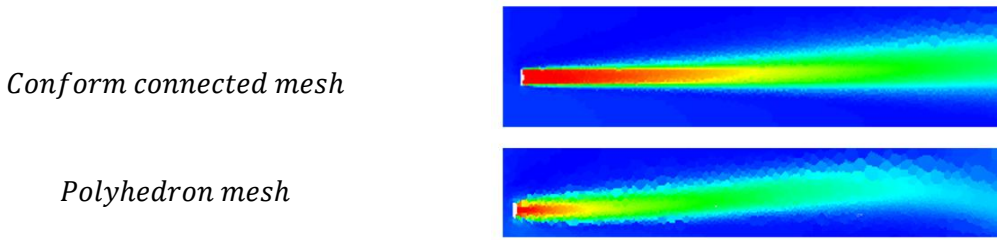

Figure 5-3: Comparison of the two meshes

The benefit of this procedure is depicted in Figure 5-3. A combination of two conform connected meshes and only one single polyhedron mesh is shown. The colours in the pictures indicate the magnitude of the flow velocity. Red colour indicates a flow velocity of 200 $\left[\frac{m}{s}\right]$.

5.1.2. General settings for mesh generation

Meshes in this Chapter are made with *FAME M*®. In Table 5-2 the general settings for the mesh generation procedure are specified. *FAME M*® takes as input a surface mesh. On this surface it generates cells with the (approximately) surface target cell size. In the volume it generates cells with the volume target cell size. On the surface it generates approximately prism cells with thickness specified in Table 5-2. Boundary layer ratio is defined as the ratio between the thicknesses of the 2nd cell layer to the first cell layer near the wall. The growth rate indicates the maximum size ratio of cells that border each other. *Auto refinement* is switched off because of a more homogeneous cell size distribution when selection this option.

Property	Value
Surface target cell size $[mm]$	15
Volume target cell size $[mm]$	20
Number of boundary layers $[-]$	2
Thickness of boundary layers $[mm]$	3
Boundary layer ratio $[-]$	0.5
Growth rate $[-]$	1.05

Table 5-2: General meshing settings for all meshes

5.1.3. Refinements

For a good mesh it is necessary to make the mesh at some locations finer than on others. This is made on locations where big gradients are expected (for example near edges of the

mesh). For this purpose cylinder refinements are defined: all cells within a cylinder are made with a defined maximum cell size.

Refinement zone	Cell size [mm]
Cyl 1	1.5
Cyl 2	15
Cyl 3	10

Table 5-3: Cell sizes at cylinder refinements for Mode 1, Mode 2, Mode 3 and Mode 3 100

In Figure 5-4 the locations of the cylinder refinement regions are indicated. Table 5-4 lists the dimensions.

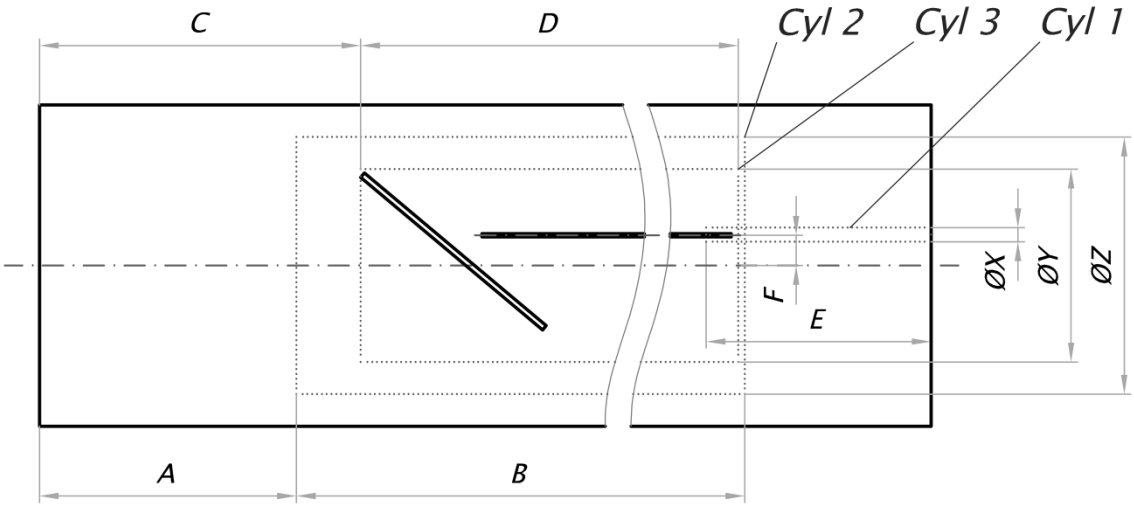

Figure 5-4: Refinement zones for Mode 1, Mode 2, Mode 3 and Mode 3 100

$A\ [m]$	0.4	$F\ [m]$	0.048
$B\ [m]$	2.31	$X\ [m]$	0.022
$C\ [m]$	0.5	$Y\ [m]$	0.3
$D\ [m]$	2.2	$Z\ [m]$	0.4
$E\ [m]$	0.35		

Table 5-4: Dimensions of cylinder refinements for Mode 1, Mode 2, Mode 3 and Mode 3 100

Also refinements on face selections are specified. In Table 5-5 dimensions for these refinements are summarized. The corresponding areas are indicated in Figure 5-1.

Area	Cell size [mm]	Refinement depth [mm]
Plate	5	10
Plate edge	2	10
Injector	1	6

Table 5-5: Dimensions of face selection refinement Mode 1, Mode 2, Mode 3 and Mode 3 100

5.1.4. Mesh check and properties

After meshing a mesh check with *FIRE*® was made. This is important to avoid failures during simulation. In Table 5-6 results from this mesh check are summarized. It indicates that no failures have been detected. In Table 5-7 properties of the mesh are summarized. The average length of one cell is 6.9 mm ($\sqrt[3]{\frac{Volume}{Number\ of\ cells}}$).

Description	Number of cells	Lower limit
Negative volume	0	
Negative normal distance	0	
Partially negative volume	0	10^{-20}
Partially negative volume (alternative)	0	10^{-20}
Cell orthogonality (cos (α))	0	0.08
Duplicated cells	0	
Identical vertex	0	
Irregular connection	0	

Table 5-6: Mesh check results for Mode 1, Mode 2, Mode 3 and Mode 3 100

Description	Value
Number of tetrahedron cells	1762
Number of hexahedron cells	1834
Number of pyramid cells	8107
Number of prism cells	7
Number of polyhedron cells	1754940

Total number of cells	1766650
Volume [m^3]	0.585
Average cell length [mm]	6.9

Table 5-7: Mesh properties for Mode 1, Mode 2, Mode 3 and Mode 3 100

5.2. Additional boundary condition

For the inclined plate two additional boundary conditions for the nozzle were made. They are shown in Table 5-8.

	Nozzle	**Nozzle wall**
Boundary condition	velocity x-direction	wall
Value	200 $\left[\frac{m}{s}\right]$ ($\dot{m} = 3.122$ $\left[\frac{g}{s}\right]$)	-

Table 5-8: Additional boundary conditions

5.3. Typical flow results

For post processing purposes, several data sets as described in Chapter 2.2 and 2.3 are evaluated at selections of 0.1 m width beginning from the inlet. The corresponding x-positions are shown in Figure 5-5. A group of cells for evaluation is called a selection. For all diagrams the geometrical barycentre of the selection is taken for the x-position ($Length$).

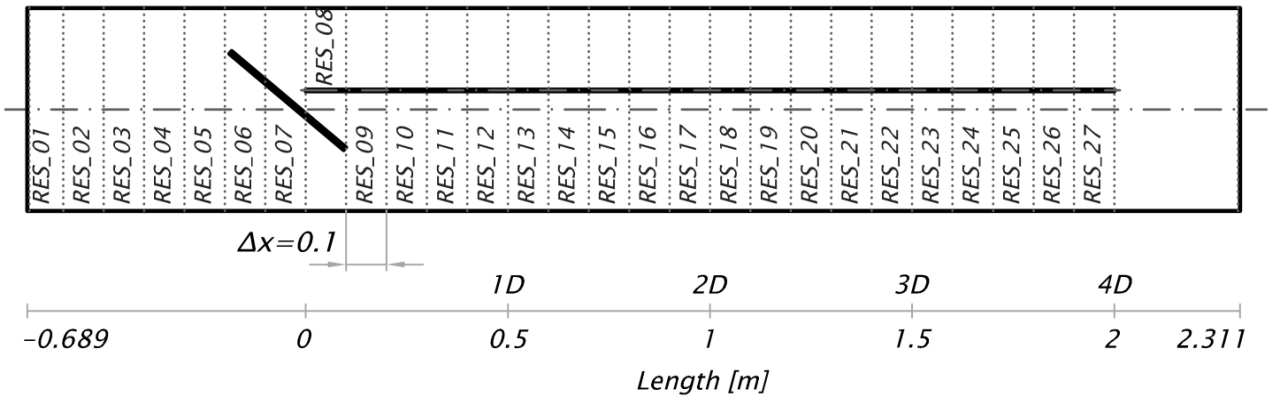

Figure 5-5: x-positions of selection regions used for evaluation of mixing indices

These selections were made with complete and half cross section as shown in Figure 5-6. The name of complete selections start with $RES\_$, while the name of half selections starts with $RESH\_$.

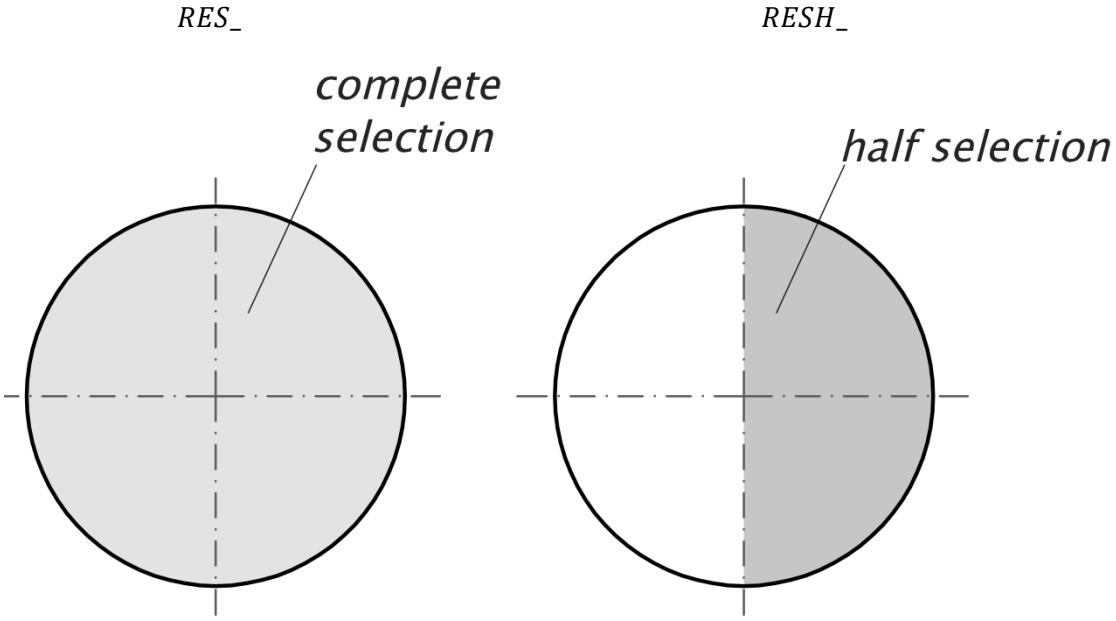

Figure 5-6: Evaluated selections

In additional to flow properties, spray droplets are recorded at four different planes beginning from injector inlet up to $x = 3D$ in steps of $1D$. Every passing droplet is recorded with position, velocity, diameter, density etc..

Before starting the spray simulation, a simulation with gas flow only was made. This is necessary to achieve a steady flow which serves as start condition for the spray simulation. It was made with same settings as for the spray simulation but with a larger timestep (see Chapter 4.3.1 for details). For proof of steadiness, the time evolution of the angular momentum was evaluated. In Figure 5-7 the corresponding results are depicted for different positions of Mode 1. After about 0.5 s the flow becomes steady.

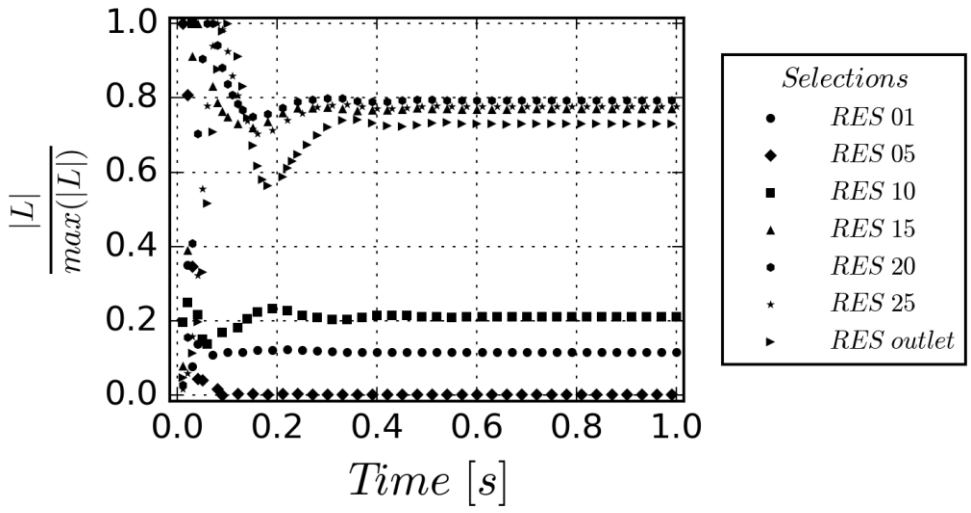

Figure 5-7: Temporal evolution of the normalized angular momentum at different positions for Mode 1 (flow only)

For spray simulations it is important that wallfilm mass, mole fraction at the outlet, liquid mass in the whole domain, and temperature at the inside of the pipe wall are constant. This values are depicted in Figure 5-8. Also, start and end times of the evaluations are drawn in (Table 5-9).

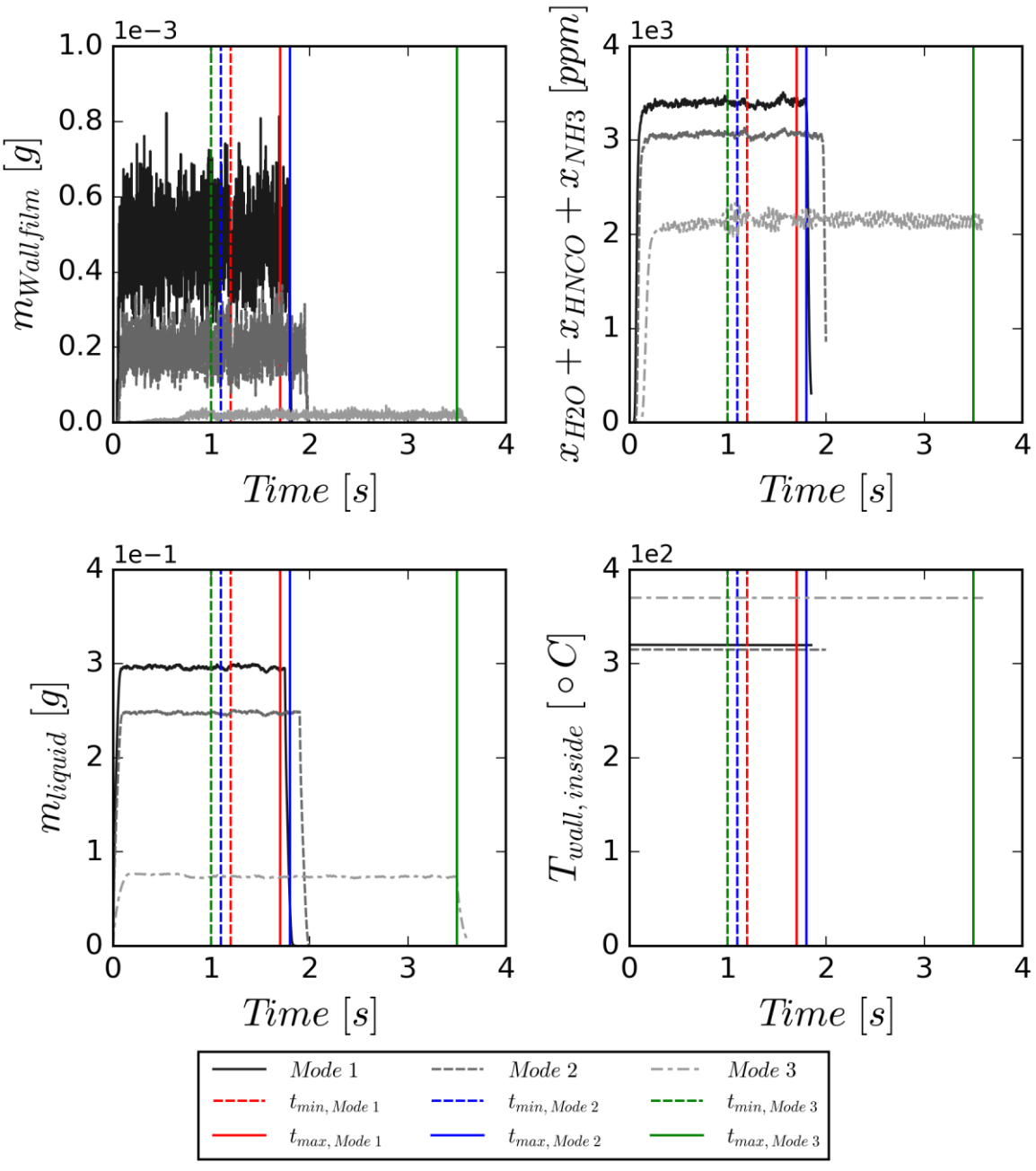

Figure 5-8: Temporal evolution of representative values for spray simulation for Mode 1, Mode 2 and Mode 3

Modes	t_{min} $[s]$	t_{max} $[s]$
Mode 1	1.2	1.7
Mode 2	1.1	1.8
Mode 3	1	3.5

Table 5-9: Evaluation times for simulations

In Figure 5-9 velocity vectors in the middle of the pipe from the spray simulation of Mode 1 are illustrated. Big green arrows indicate the main flow; and red ones the injector. This cut is in flow direction. Directly after the inclined plate for a short length backflow occurs, but approximately 0.5 m after the trailing edge this backflow disappears.

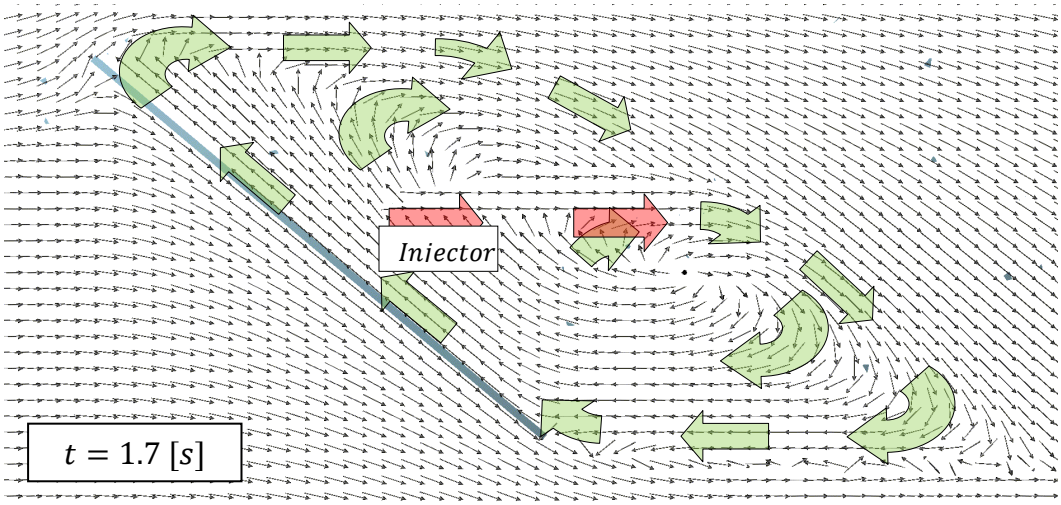

Figure 5-9: Velocity vectors of spray simulation at inclined plate and injector of Mode 1

Figure 5-10 shows velocity vector fields beginning from the injector in slices at distances $0D, 1D, 2D$ and $3D$ downstream of the injector. A counter rotating vortex pair appears which increases the mixing effect. Velocity unit is $[m/s]$.

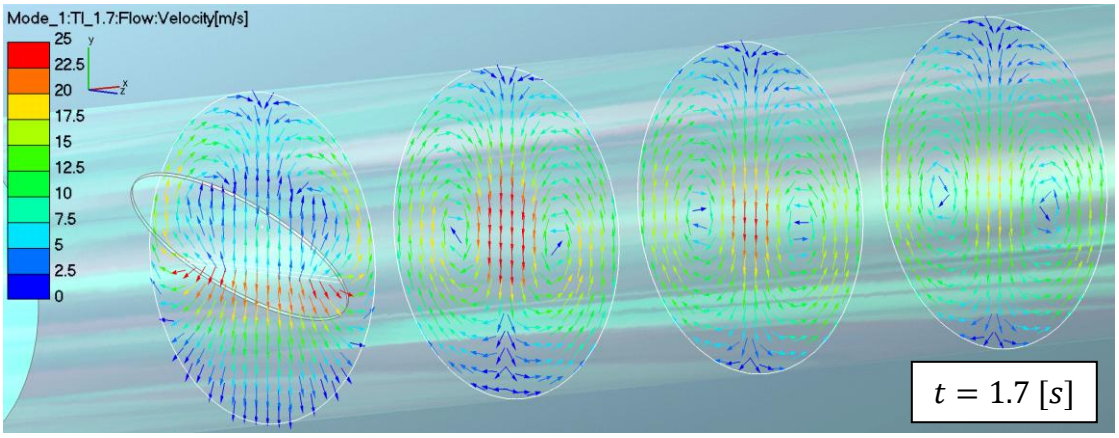

Figure 5-10: Velocity vectors for Mode 1

5.4. Results

5.4.1. General remarks

All evaluations in this section are regarding spray simulations and time averaged values from times shown in Table 5-9. The trailing edge (i.e., the downstream end of the inclined plate) and the leading edge (i.e., the upstream end of the inclined plate) are depicted in the diagrams. The origin of the coordinate system is located at the droplet injection point according to the coordinate system defined in Figure 5-1.

5.4.2. Symmetry of flow

In the investigated geometry it is important to note that the (time-averaged) flow is symmetric. For this the kinetic energy of the whole profile, as well as that of the half profile (see Figure 5-6) has been evaluated as a function of the axial position x. The quotient of them has to be two in ideal case because energy of whole profile has to be double as high in case the flow is symmetric.

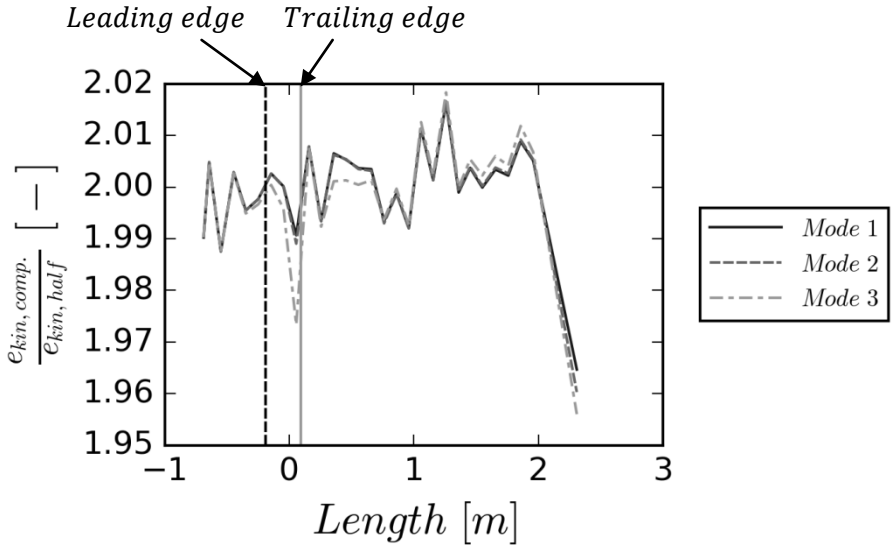

Figure 5-11: Ratio of kinetic energy of complete and half profile versus the axial position for Mode 1, Mode 2 and Mode 3

In Figure 5-11 shows that Mode 1 and Mode 2 have nearly over the whole length a difference of the kinetic energies of less than one percent. Mode 3 has at the trailing edge a higher deviation than Mode 1 and Mode 2. In summary it can be said that Mode 1 and Mode 2 have nearly the same flow behaviour. Mode 3 has sometimes higher values. Finally, it should be noted that because a polyhedron mesh was used, the half profile may not have exactly half the volume of whole profile.

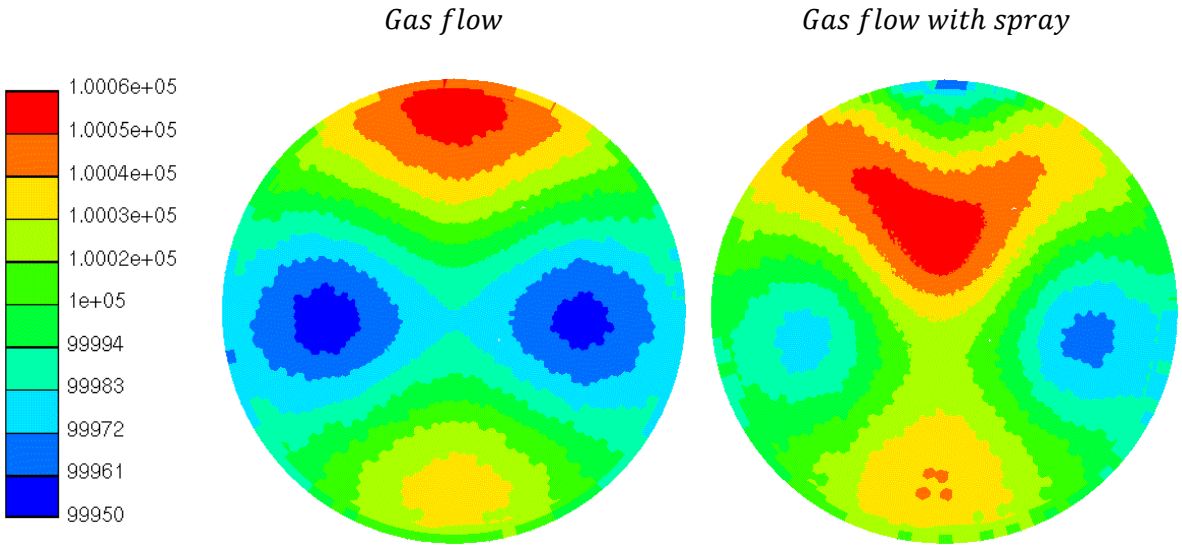

Figure 5-12: Static pressure of Mode 1 on outlet, unit of colour bar is [Pa]

In Figure 5-12 the pressure distribution of Mode 1 is shown. The gas flow (left panel) shows a very symmetric distribution. In the spray simulation (right panel) the situation changes, and an asymmetric flow field is obtained. This also occurred at Mode 2 and Mode 3.

In Figure 5-14 the total and static pressure versus the length of the domain for the complete profile are shown. For a better visualisation, p_{out} of the boundary condition on the outlet is subtracted from the pressure p_i at position i. This is depicted in Figure 5-13.

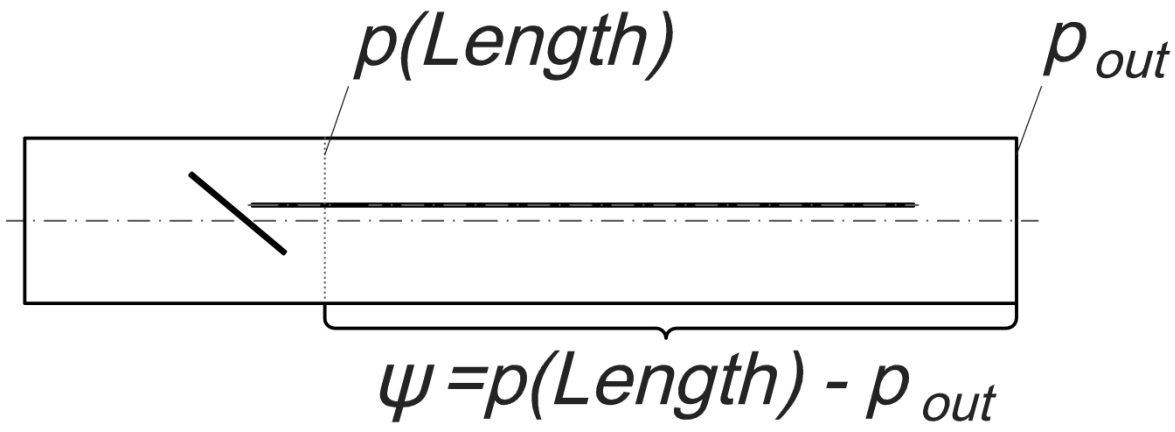

Figure 5-13: Pressure subtraction

Between the leading and the trailing edge both p_{tot} and $p_{stat.}$ decrease monotonically. The drop in $p_{stat.}$ is larger (approximately 700 Pa at Mode 1 from the maximum to minimum) compared to p_{tot} (approximately 575 Pa from maximum to minimum) because of the velocity increase in the bottleneck of inclined plate. The same effect is causing a higher increase of $p_{stat.}$ after the leading edge because of lower velocity.

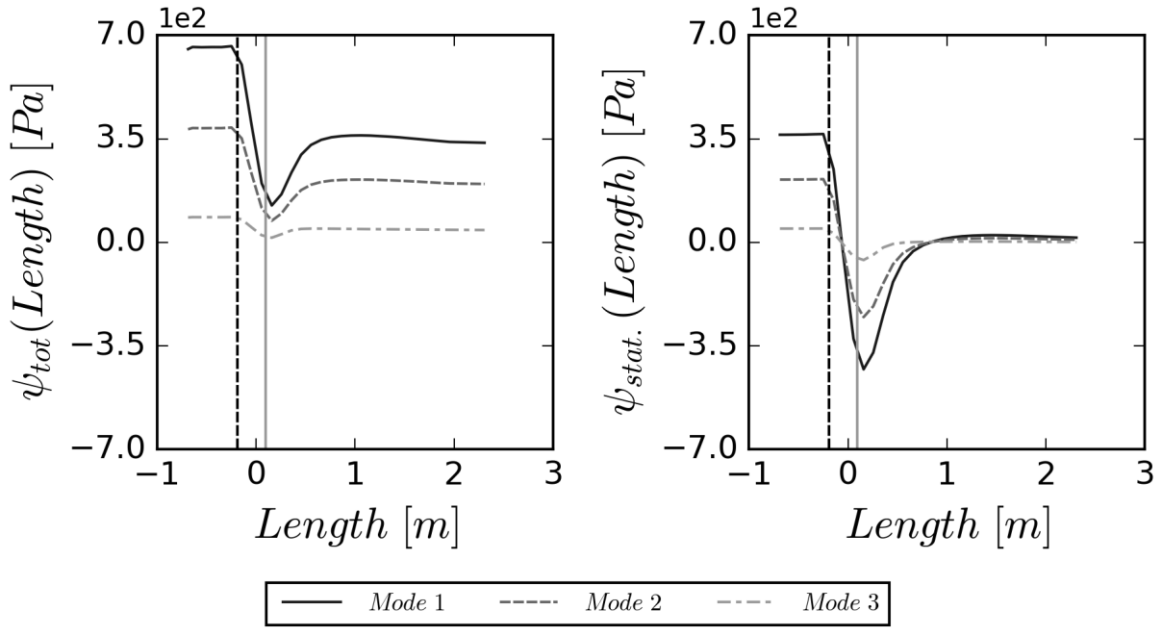

Figure 5-14: Total (left panel) and static pressure (right panel) in the whole cross section over length of domain for Mode 1, Mode 2 and Mode 3

In Table 5-10 pressure losses from the different modes are shown. Mode 1 is slightly above the limit given in Chapter 4.1 with 300 Pascal.

Mode	$\Delta p_{tot}\ [Pa]$
Mode 1	317.5
Mode 2	185.3
Mode 3	42.6

Table 5-10: Pressure loss from inlet to outlet

5.4.3. Angular momentum and angular velocity

In Figure 5-15 the angular momentum and the angular velocity versus the length of the pipe are illustrated for the half cross section. Rotation axis for angular momentum calculation is the geometrical barycentre of the selection. At the inlet both are nearly zero and start to increase near the leading edge. At approximately $x \sim 0.8\ [m]$ (for Mode 1 and Mode 2) respectively $x \sim 0.4\ [m]$ $|L|$ and $|\omega|$ are decreasing. All Modes have similar qualitative behaviour but differ in magnitude. $|L|$ fluctuates because it is directly influenced by the mass, and the evaluated selections do not have exactly same size, i.e., the mass differs slightly in each selection. Because of this L is very small at the outlet because the cell selection is very thin. $|L|$ and $|\omega|$ are important values and main contributors for mixing. If their values are very low, an insufficient mixing can be expected.

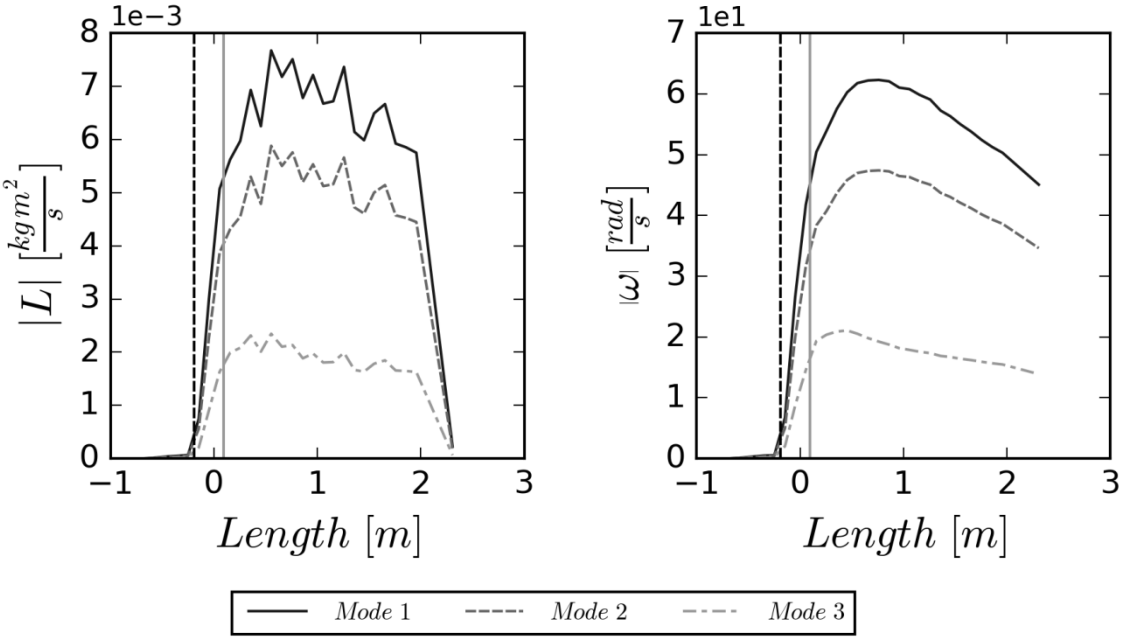

Figure 5-15: Angular momentum and angular velocity for Mode 1, Mode 2 and Mode 3

Oscillations at Mode 3 for L were quite high. In Figure 5-16 the temporal fluctuation of L is depicted at an axial location of $x = 0.25$ and at the $Outlet$. At the $Outlet$ the longer the simulation lasts, the lower is the oscillation but it does not disappear. At the axial position $x = 0.25$, nearly no decrease of oscillation can be recognized.

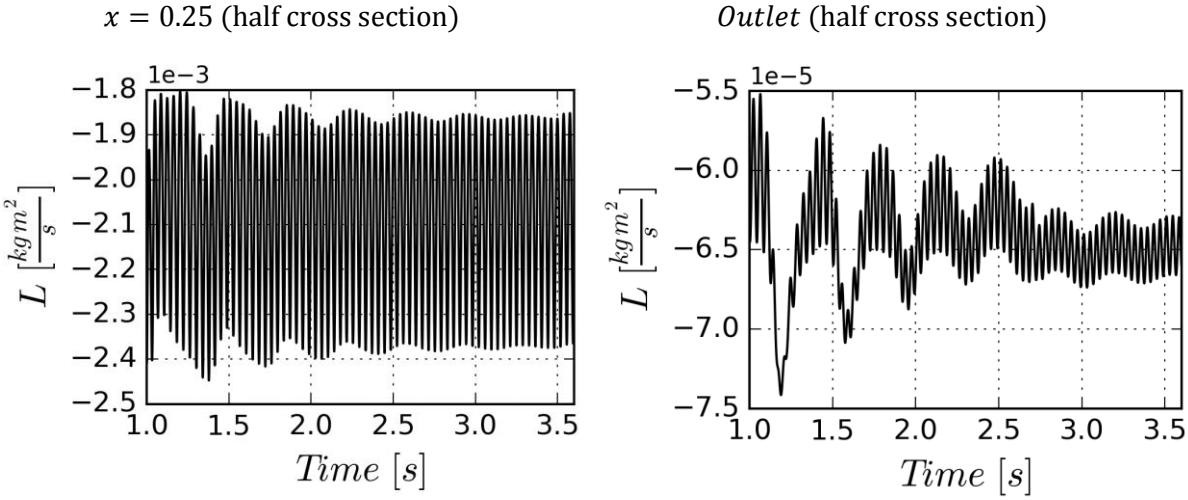

Figure 5-16: Angular momentum on outlet for Mode 3 at different positions

Because of this, simulation of Mode 3 was repeated with a finer mesh to test if the grid resolution causes the oscillation. The general mesh size was reduced from 20 mm to 15 mm. Cylinder refinements for the refined case are shown in Figure 5-17; corresponding dimensions are summarized in Table 5-11, Table 5-12 and Table 5-13. The goal was to refine especially around the edge of the inclined plate.

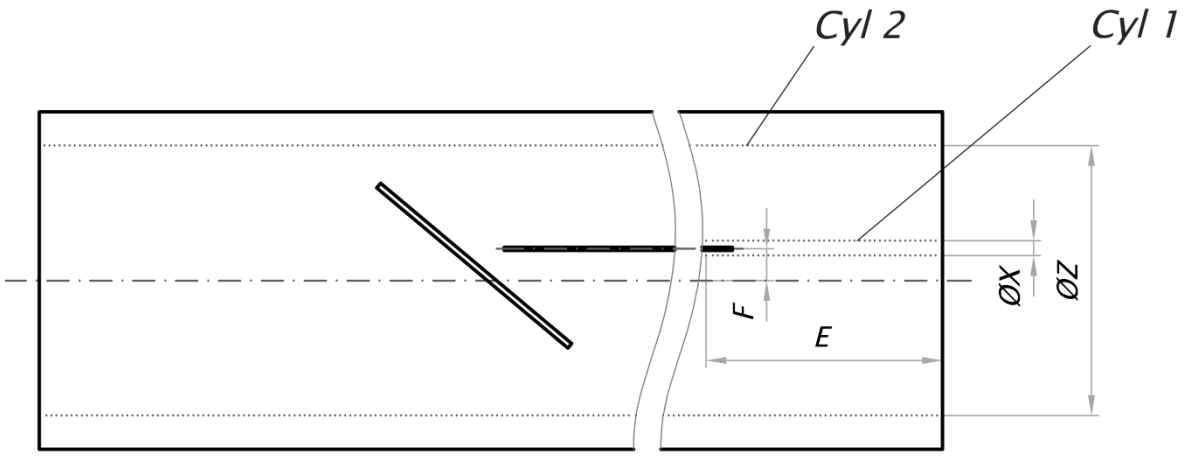

Figure 5-17: Cylinder refinements of Mode 3 fine

Refinement zone	Cell size [mm]
Cyl 1	1.5
Cyl 2	10

Table 5-11: Cell sizes of Mode 3 fine

$E\ [m]$	0.35	$F\ [m]$	0.048
$X\ [m]$	0.022	$Z\ [m]$	0.4

Table 5-12: Dimensions of cylinder refinements of Mode 3 fine

Area	Cell size [mm]	Refinement depth [mm]
Plate	4	12
Plate edge	2	12
Injector	1	6

Table 5-13: Dimensions of face selection refinements of Mode 3 fine

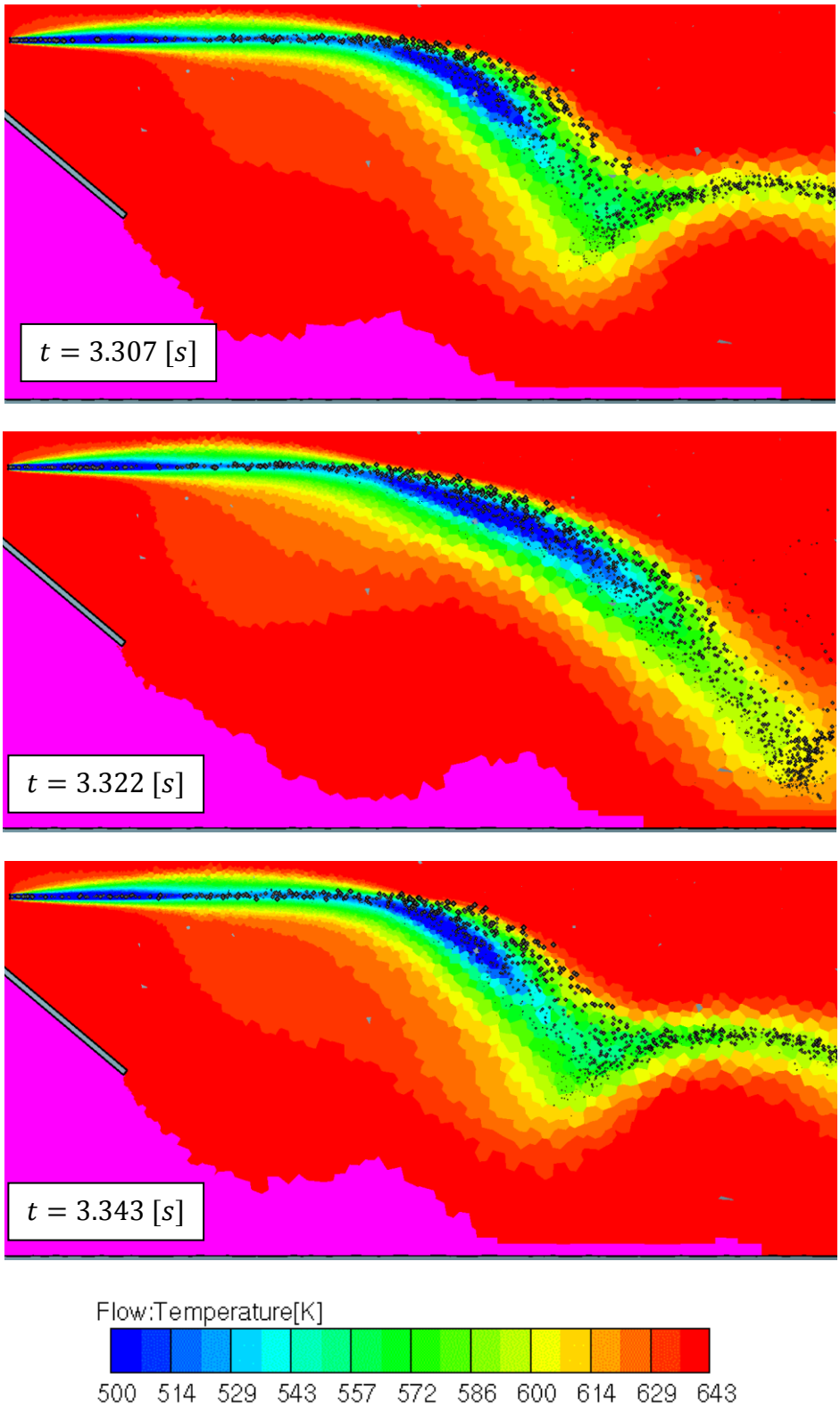

Figure 5-18: Spray characteristic near the injector inlet of Mode 3 fine at different times

However, also with the refined mesh oscillation appeared. After further investigation, an explanation of this could be the evaporation of spray droplets. At the beginning of an oscillating cycle, droplets are evaporated very quickly because of hot exhaust gas (see

Figure 5-18). Evaporation requires a large amount of energy and cools down the gas. Because of this the following droplets are not evaporated as fast as that before, and the temperature of the gas starts to increase again. Then, the cycle starts again.

5.4.4. Gas mixing properties

Several parameters concerning mixing are depicted in Figure 5-19. The mixing of the gas phase was calculated with the uniformity index γ_g (see Chapter 2.2.1). Species considered are NH_3 and $HNCO$. At the beginning, γ_g is 1 because there is no species in this area. After a peak γ_g is decreasing and increasing again for Mode 1 and Mode 2. This peak is approximately three times diameter after the injector. Mode 3 shows a quite different behaviour. It has a local maximum at the trailing edge and after a local minimum shortly behind the trailing edge it is increasing nearly constantly.

The species concentration is rising constantly from the inlet to the outlet for all modes. It is expressed as a ratio of concentration and maximum possible concentration ϵ as shown in Eqn. 2-4.

$$\epsilon = \frac{x_{NH3} + x_{HNCO}}{x_{NH3,max} + x_{HNCO,max}} \qquad \textbf{Eqn. 5-1}$$

Therefore mass flow of UWS is calculated from mass flow NO_x in Eqn. 5-2.

$$\dot{m}_{UWS} = \frac{\dot{m}_{NOx}}{\underbrace{46}_{Mole\ NO_x}} \underbrace{60}_{MM\ Urea} \underbrace{\frac{1}{2}}_{Urea \rightarrow 2NH_3} \underbrace{\frac{1}{0.4}}_{weigth\ fraction\ UWS} = 2.006\,\dot{m}_{NOX} \qquad \textbf{Eqn. 5-2}$$

In Table 5-14 the corresponding NO_x and $HNCO$ concentrations, calculated with mass flows for UWS and gas as defined in Chapter 2.3.3 according to Eqn. 5-3, are shown.

Property	$Mode\ 1$ [ppm]	$Mode\ 2$ [ppm]	$Mode\ 3$ [ppm]
x_{NOx}	1100	980	650
$x_{NH3,max} + x_{HNCO,max}$	1050	931	618

Table 5-14: Nitrous gases and corresponding ammonia and isocyanic acid concentration

$$x_{NH3} + x_{HNCO} = \frac{\dot{n}_{NH3}}{\dot{n}_{NOX}}\, x_{NOx} \qquad \textbf{Eqn. 5-3}$$

Also of interest for characterising mixing properties is the ratio of the tangential (y and z-direction) and the axial (x-direction) kinetic energy $\frac{e_{kin,tan}}{e_{kin,ax}}$. The higher this ratio, the higher the mixing rate can be expected. The inclined plate indicates an only slowly decreasing

ratio as a function of the axial position. This indicates that mixing will appear also after a certain length, and is not only limited to the area of the inclined plate itself.

A high yield of species evaporation Y, as defined below, is important for proper operation of the mixer.

$$Y = \frac{\dot{m}_{NH3} + \dot{m}_{HNCO} + \dot{m}_{H2O}}{\dot{m}_{liquid,injected}} \qquad \textbf{Eqn. 5-4}$$

As expected, the yield is increasing monotonically from the inlet towards the outlet. Mode 1 and Mode 2 have nearly the same behaviour. Mode 3 has a higher yield. A reason for this is probably the higher temperature of Mode 3, which leads to more complete evaporation of droplets. At Mode 1 and Mode 2 it is rising till the outlet. Y is only evaluated at the inlet, the outlet and at the beginning from injector every diameter D downstream.

Most times the mass balance from Chapter 2.3.3 is fulfilled within an error corridor of less than 2 %. Only from the inlet to the injector big deviations occur. Reasons for this can be that there is nearly no mass flow in this region ($< 5 \cdot 10^{-6}$ $\left[\frac{kg}{s}\right]$). It also has to be considered that the post-processed mass flow data for the calculation can have a deviation of 5 %. At Mode 3, between the injector and a position $1D$ downstream of it an error of 6.8 % occurs.

The swirl number $\left|\frac{n_s}{n_f}\right|$ starts to increase downstream of the leading edge and decreases at $x \sim 0.8\,[m]$ (for Mode 1 and Mode 2) respectively $x \sim 0.4\,[m]$ for Mode 3. Mode 1 and Mode 2 have nearly the same values over whole length. The qualitative behaviour is similar to $|\omega|$. $|\omega|$ and $|L|$ have been already discussed in Figure 5-15. V_{cyl} (see Chapter 2.3.2) was calculated with a diameter and length of 1 $[m]$.

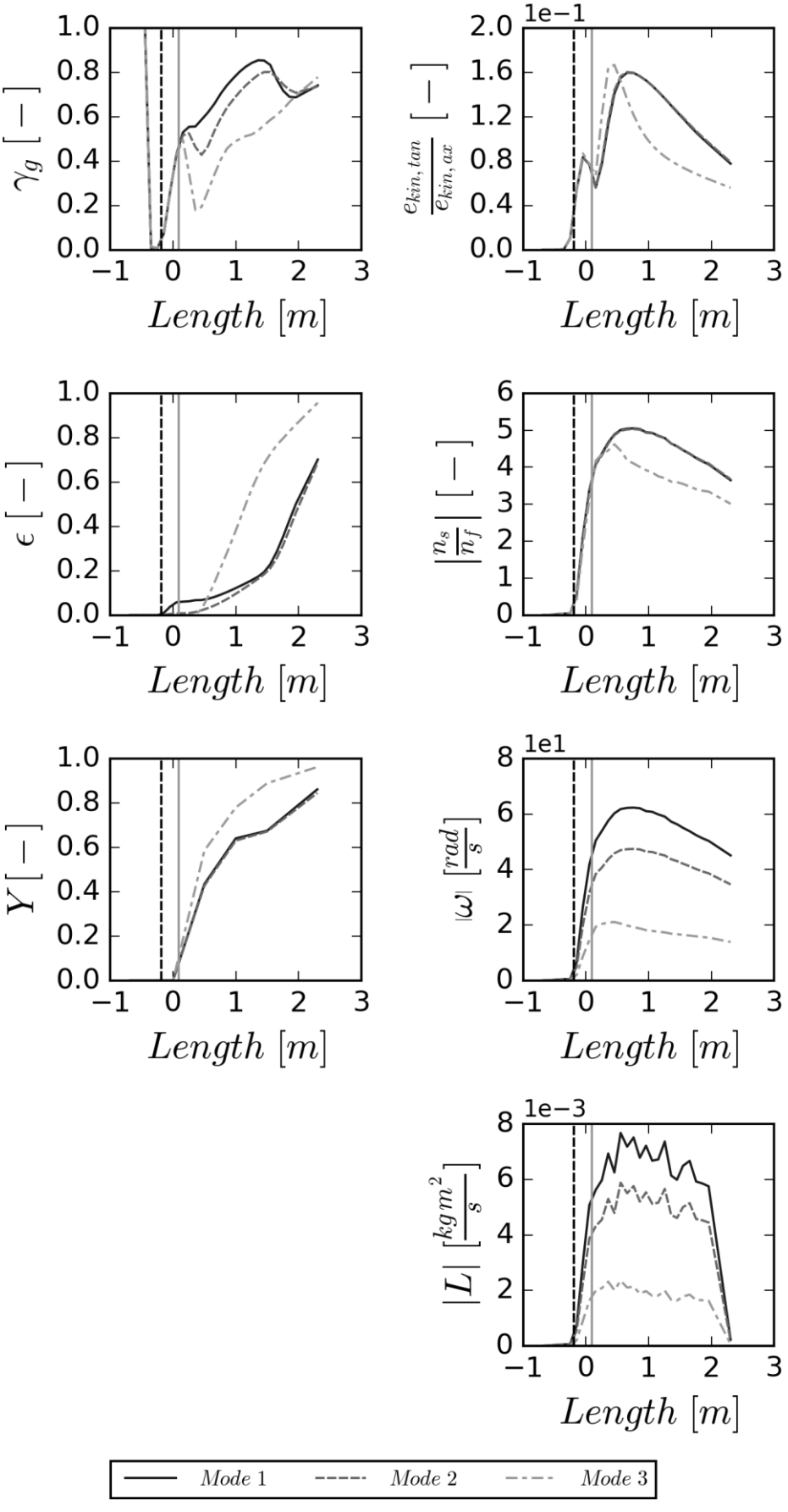

Figure 5-19: Gas mixing properties of Mode 1, Mode 2 and Mode 3

5.4.5. Spray properties

Figure 5-20 shows the spatial spray distribution in domain for Mode 1 to Mode 3. Different modes are indicated with different colors. Mode 3 has the best distribution in space.

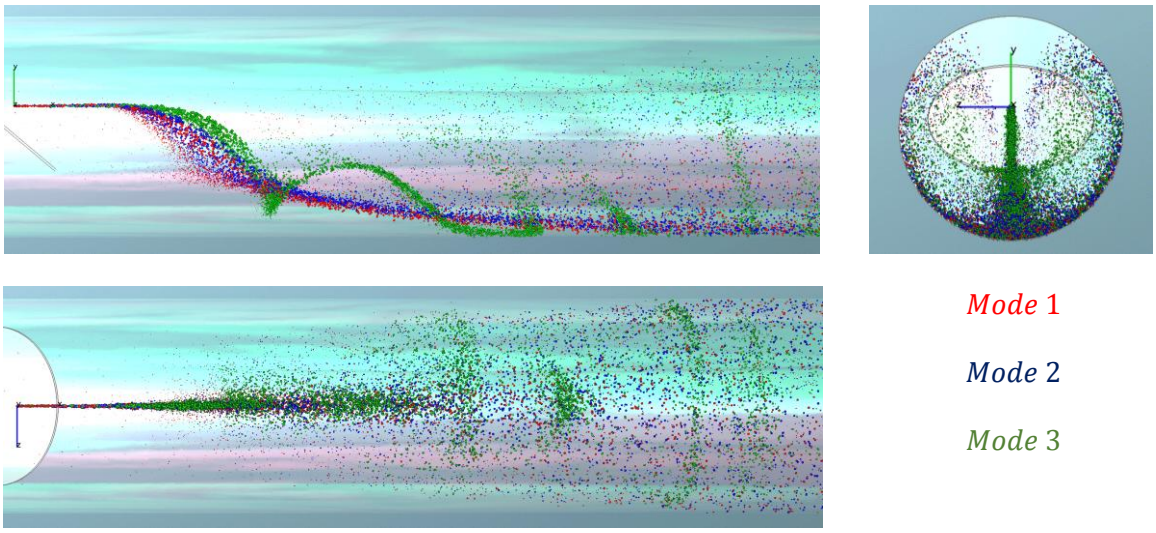

Figure 5-20: Spray clouds for Mode 1, Mode 2 and Mode 3

A good indicator for the spray symmetry is the ratio between the angular momentums of spray droplets for each half of the cross section depicted in Figure 5-21. Angular momentums are calculated with geometrical barycentre of considered region (barycentre of semicircle is $\vec{P}_1$ in L) and normal vector $\vec{n} = \vec{P}_2 - \vec{P}_1 = \begin{pmatrix} 1 \\ 0 \\ 0 \end{pmatrix}$ (parallel to flow direction). It indicates that the spray flow has a quite big deviation from symmetry. The biggest deviation is observed for Mode 3.

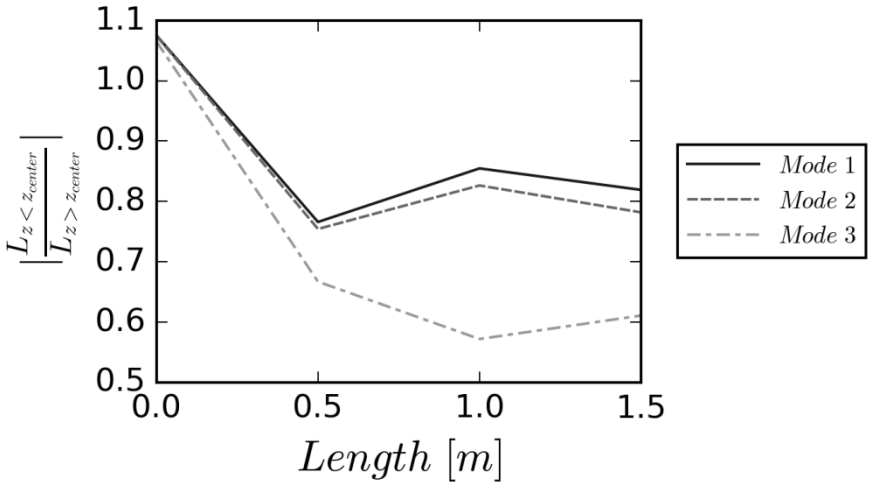

Figure 5-21: Angular momentum ratios of spray droplets for Mode 1, Mode 2 and Mode 3

Figure 5-22 - Figure 5-24 shows the influence of different evaluation times when evaluating the spray mixing factors. The longer evaluation time, the higher the mass passing a spray plane, and hence a more stable result can be expected. The durations were chosen for an injected mass of $1\ g$, $2.5\ g$ and $5\ g$. Minimum and maximum times are indicated in Table 5-9. If values are smaller -0.01 or higher than 2 at position $x = 0\ [m]$ (injector position) they are not shown in this figure. The spray planes have been evaluated with a mesh size of $0.010\ [m]$ (diagrams on left side) and $0.020\ [m]$ (diagrams on right side).

While the influence of the evaluation time on U_s is small, it is very high on U_d. An explanation for the high U_d deviations is simple: if more cells of the cross section have droplets, the enumerator of U_d gets smaller because there are less cells with no droplets (i.e., in which $d_{32,i} = 0$). U_d also reaches values higher than 1. High U_d deviations lead to high Q_m deviations.

For γ_m and γ_j different evaluation durations have nearly no influence. These two metrics also do not differ significant from each other. Because of that, only γ_m is shown in Figure 5-22 - Figure 5-24. $\frac{S_{WD}}{S}$ is the ratio between the area affected by droplets and the whole area of the cross section. The influence of evaluation duration on this metric is quite high. This can be explained easily: the longer the evaluation time, the higher the possibility that a cell is affected by an droplet.

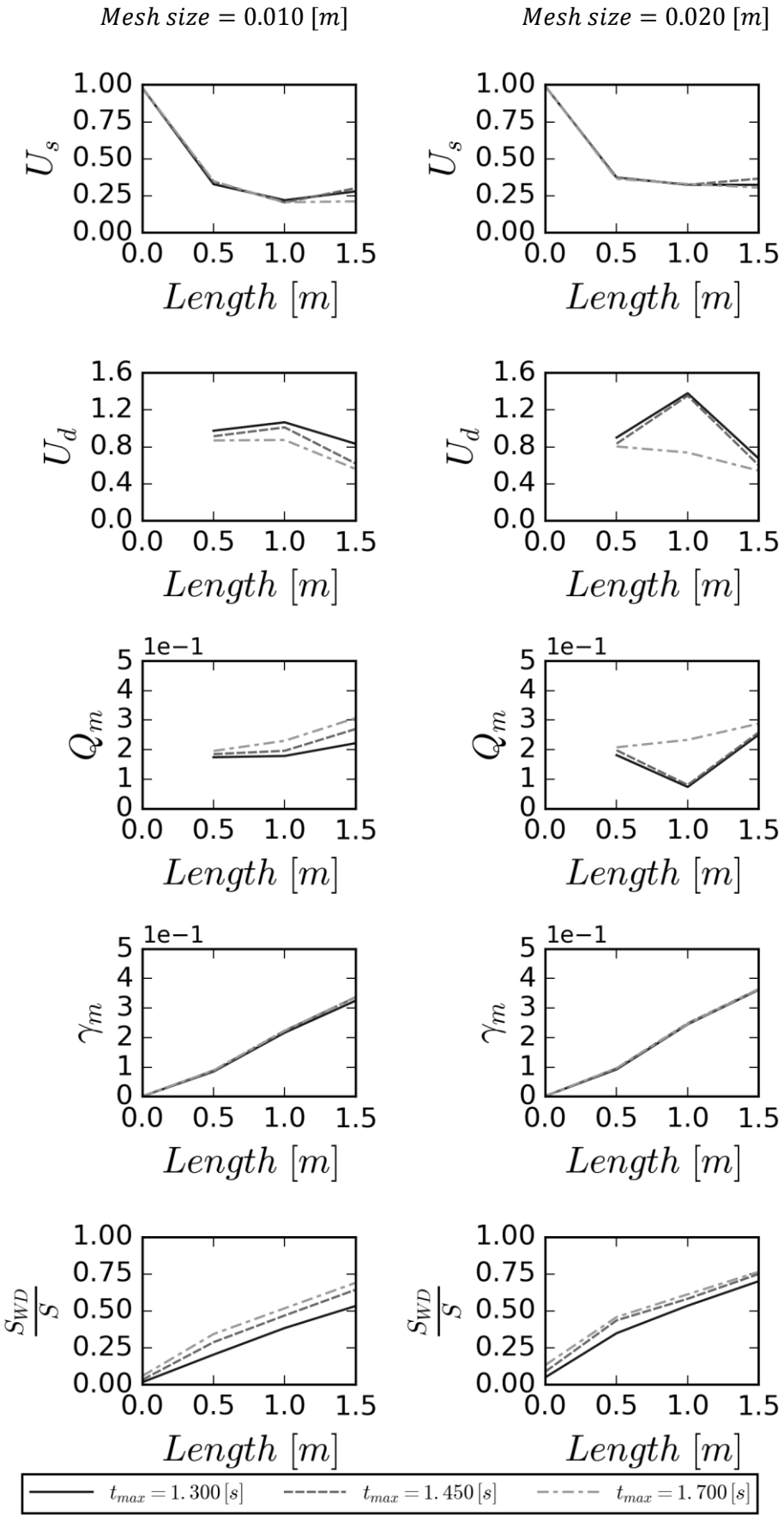

Figure 5-22: Spray mixing factors for different evaluation times and mesh sizes Mode 1

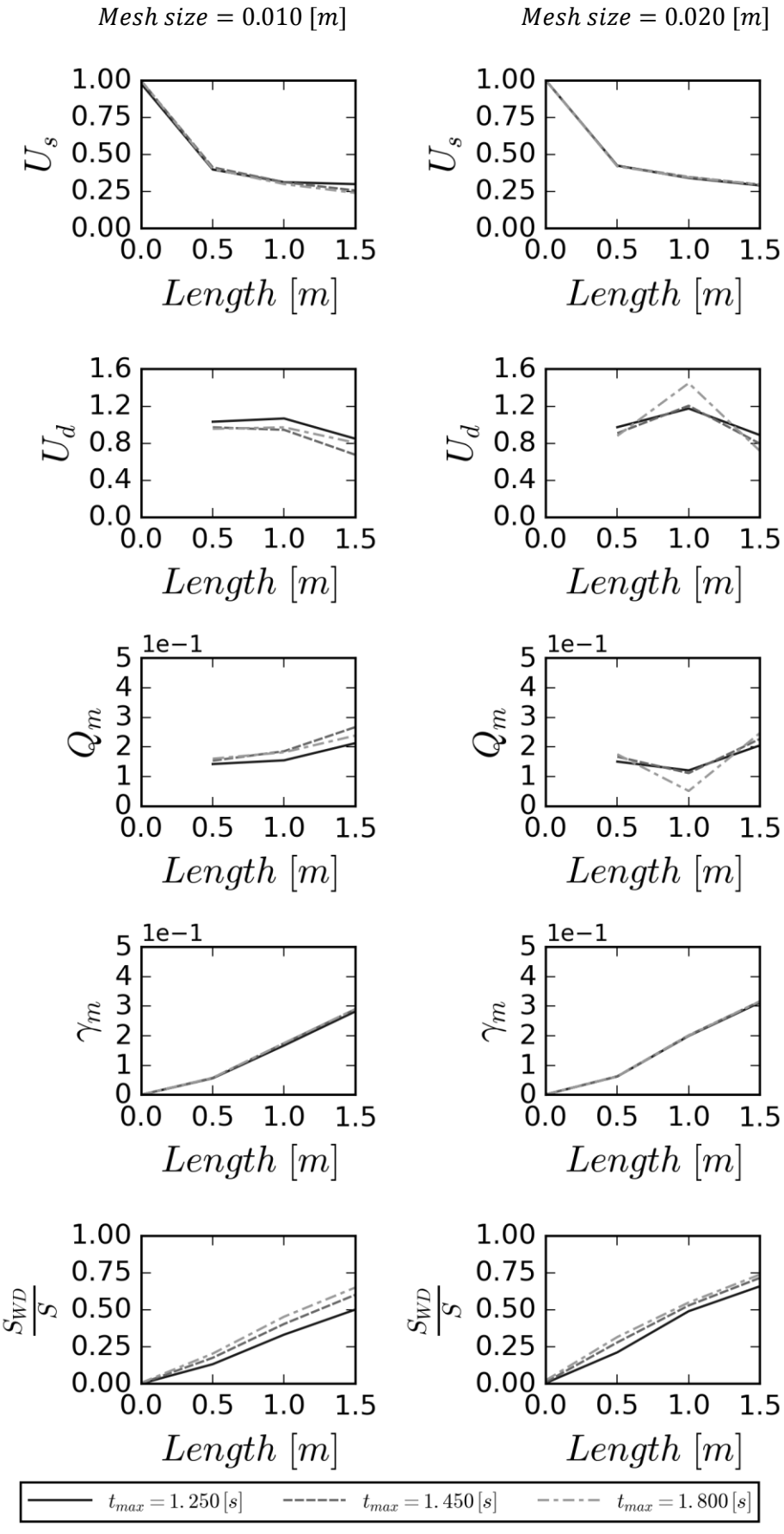

Figure 5-23: Spray mixing factors for different evaluation times and mesh sizes Mode 2

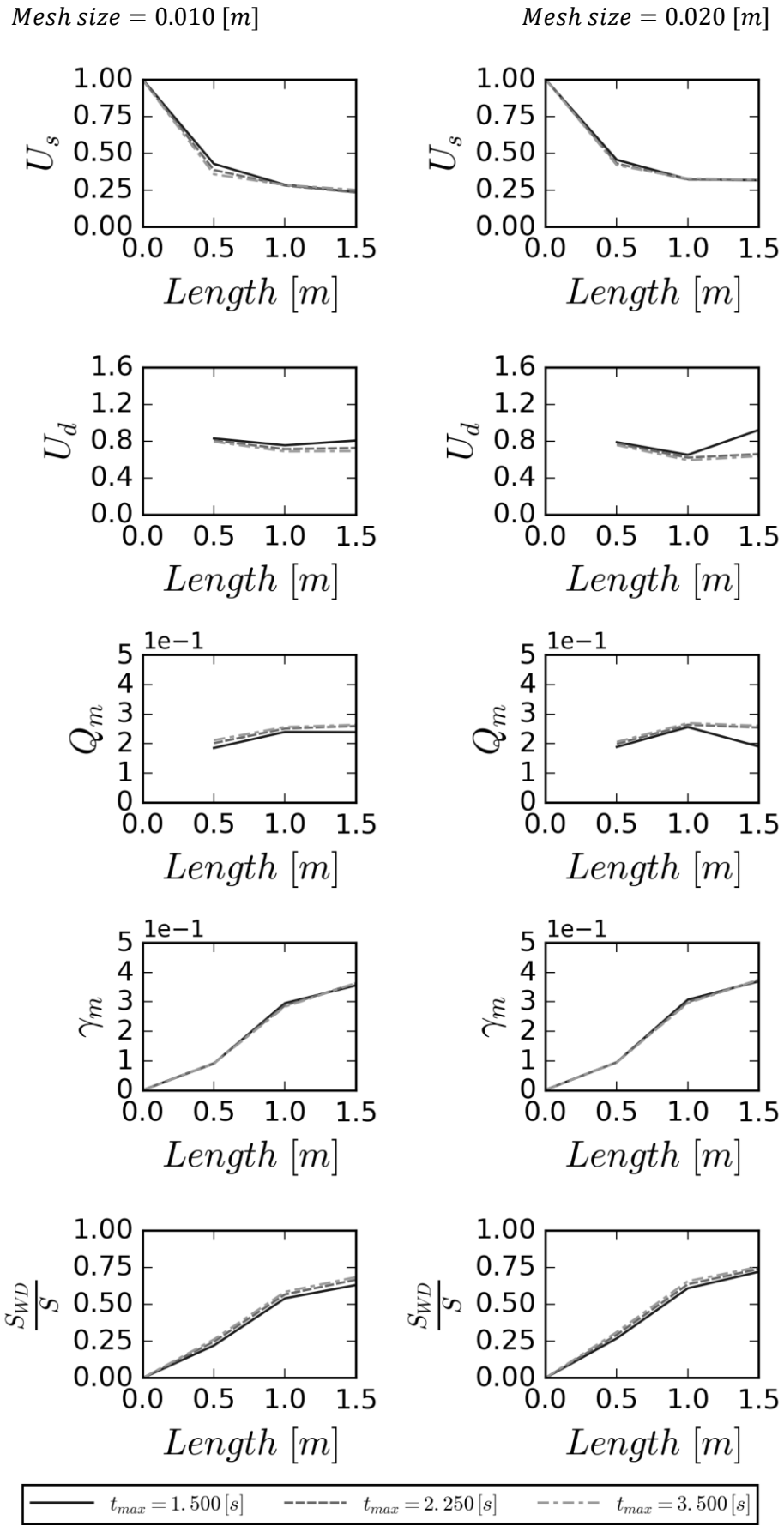

Figure 5-24: Spray mixing factors for different evaluation times and mesh sizes Mode 3

Also, an influence of the mesh size can be observed. U_d, and also Q_m show a quite high mesh size dependency, as well as time dependencies. Fortunately, U_s has a lower sensitivity to these settings.

Also for $\frac{S_{WD}}{S}$ a certain influence of the mesh size can be observed. The bigger the mesh size, the higher is the value for $\frac{S_{WD}}{S}$ because of bigger size of each affected cell.

γ_m has nearly same behaviour at both mesh sizes. Mesh dependence is getting higher with increased distance from injector. γ_m is getting higher constantly over length.

The degree of mixedness ξ delivers no reasonable values, and hence is not shown in this thesis.

In Figure 5-25 the spatial mass flow distribution of spray droplets for Mode 1 and Mode 3 at different positions is shown for a mesh size of $20\ [mm]$. The definition for mass flow is shown in Eqn. 5-5. The mass flow in one cell i is the ratio of the mass passing between the time instant t_{min} and t_{max}, and the time difference $t_{max} - t_{min}$.

$$\dot{m}_i|_{t_{min}}^{t_{max}} = \frac{m_i|_{t_{min}}^{t_{max}}}{(t_{max} - t_{min})} \qquad \textbf{Eqn. 5-5}$$

At $x = 0.5\ [m]$ the spray stream is very concentrated at one point. Mode 1 is better distributed at this position than Mode 2, probably this is due to backflow in Mode 1. At $x = 1\ [m]$ Mode 1 and Mode 2 are similarly distributed with a bigger covered area observed for Mode 1. At $x = 1.5\ [m]$ this same trend is visible. An unbalance between left and right half occurs. The left side has always a bigger area than the right side. Results for Mode 3 are shown in Chapter 5.5.2. The highest mass flow indicated in colorbar is set in a way that mass flow differences can be seen good. I. e. that cells indicated with this mass flow can have a even higher mass flow.

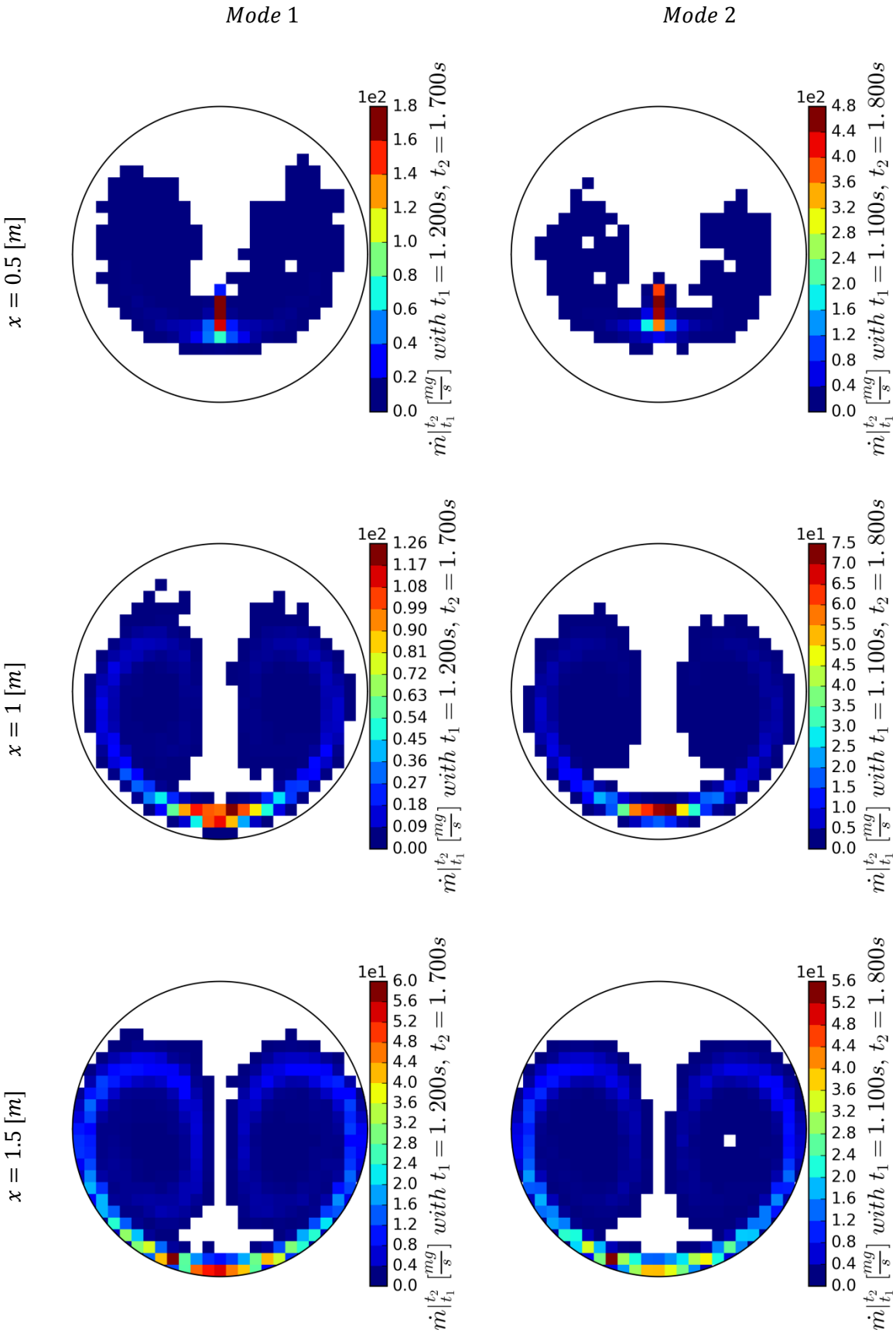

Figure 5-25: Spatial spray mass flow distribution for Mode 1 and Mode 2

5.4.6. Suggestions for improved mixing factors

To avoid high U_d deviations, which lead to high Q_m deviations explained in Chapter 2.2.2, a modification is suggested when calculating $U_{d,f}$. Specifically, the latter should be calculated the same as U_d, however, using the cell averaged Sauter mean diameter $d_{32,f}$ as shown in Eqn. 2-13 instead of $d_{32,whole}$. Cells with no droplets are treated with $d_{32,i} = 0$.

$$d_{32,f} = \frac{\sum_{i=1}^{n} d_{32,i}\ A_i}{\sum_{i=1}^{n} A_i} \qquad \textbf{Eqn. 5-6}$$

With $U_{d,f}$ the mixedness quality $Q_{m,f}$ is calculated. $U_{d,f}$ is, at every position in the simulated domain, smaller than 1. The very low values at the injector position for example for Mode 1 can be explained with backflow of very small droplets in this area. This causes a higher $d_{32,f}$ and a smaller $U_{d,f}$. $U_{d,f}$ has also a lower time dependent differences than U_d. This also leads to lower deviations of $Q_{m,f}$ compared to Q_m.

In Figure 5-26 the behaviour of $Q_{m,f}$ at different mesh sizes for all evaluation times are depicted. $Q_{m,f}$ has lower time-and mesh size-dependent differences than Q_m. $Q_{m,f}$ has also decreasing and stagnant regions, which makes it a less robust metric to use.

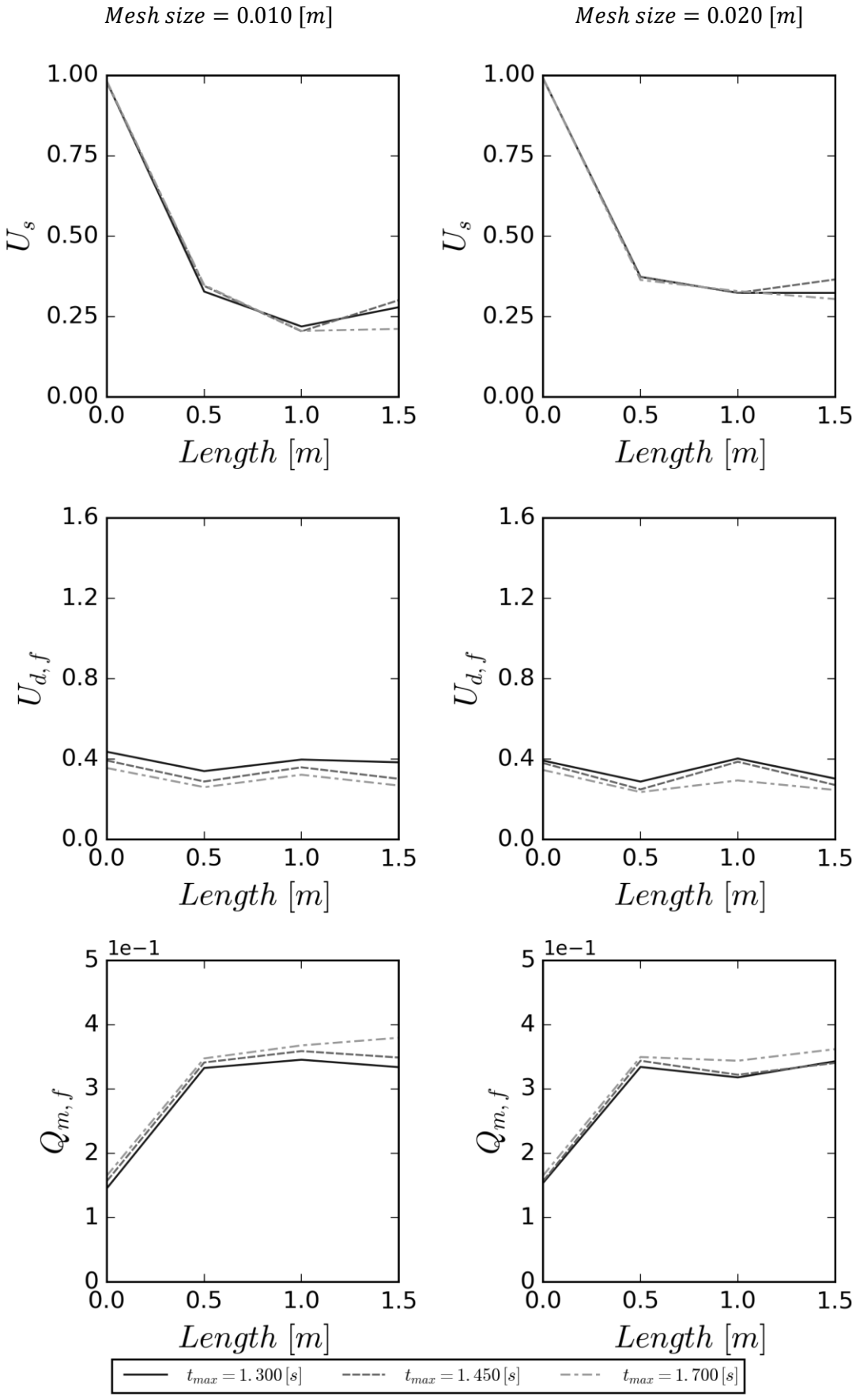

Figure 5-26: Spray mixing factors for different mesh sizes for Mode 1

5.5. Comparison of Mode 3 with different settings

5.5.1. Flow properties

In Figure 5-27 values for all Mode 3 simulations are depicted. It shows same values as that reported in Figure 5-8 for Mode 1 to Mode 3. "Mode 3 fine" is a simulation of Mode 3 with a finer mesh (see Chapter 5.4.3) and "Mode 3 100" is a simulation with a droplet injection velocity of 100 $\left[\frac{m}{s}\right]$ with the mesh from Mode 3. Most distinguishing detail is the concentration on outlet $x_{H20} + x_{HNCO} + x_{NH3}$. At Mode 3 fine it is oscillating the most. Evaluation durations for all three simulations are the same as in Table 5-9 for Mode 3.

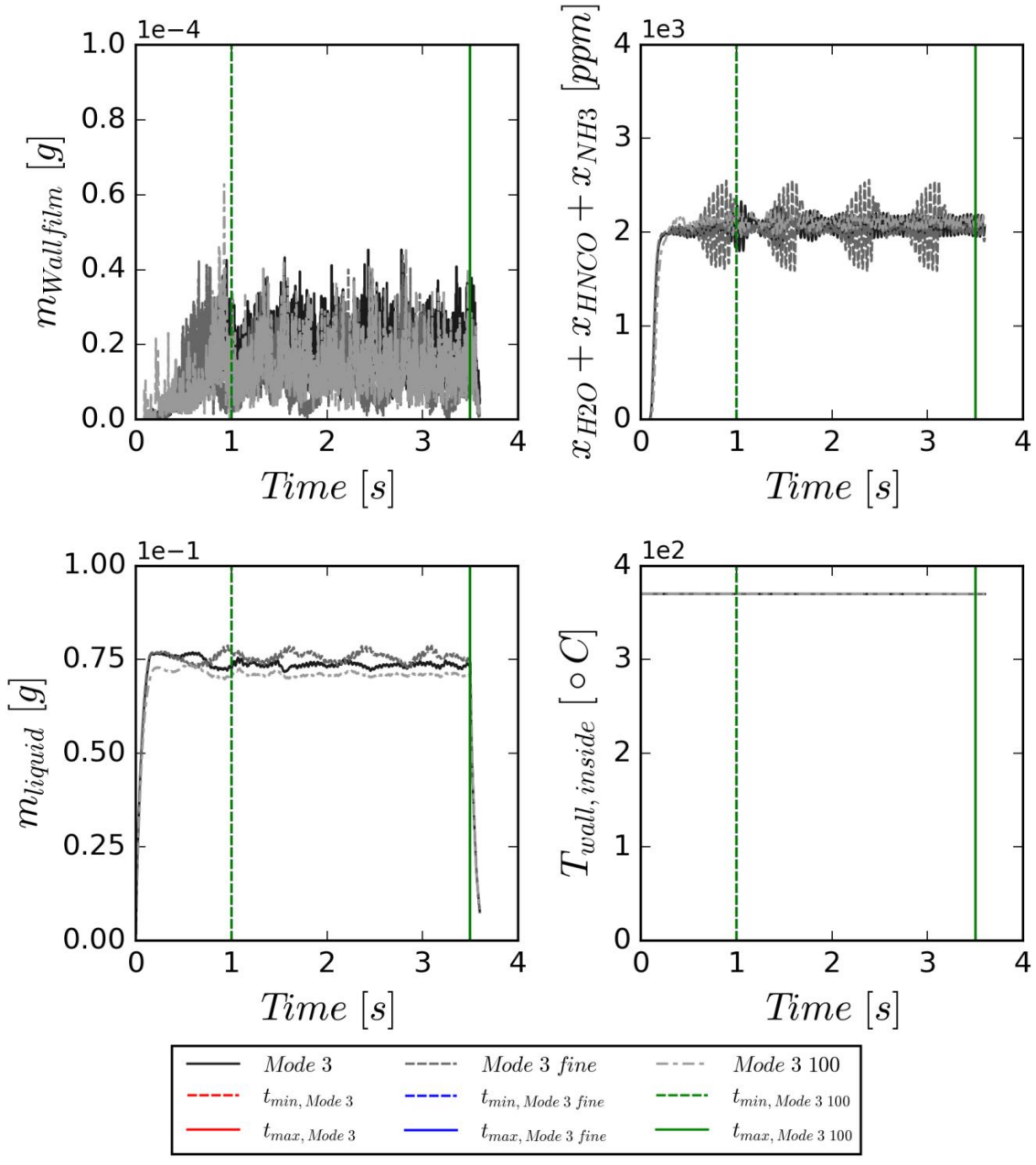

Figure 5-27: Representative values for spray simulations Mode 3, Mode 3 fine and Mode 3 100

For the kinetic energy ratio shown in Figure 5-28, a mesh dependency is observed. Mode 3 and Mode 3 fine indicate nearly the same results; Mode 3 fine has a different trend.

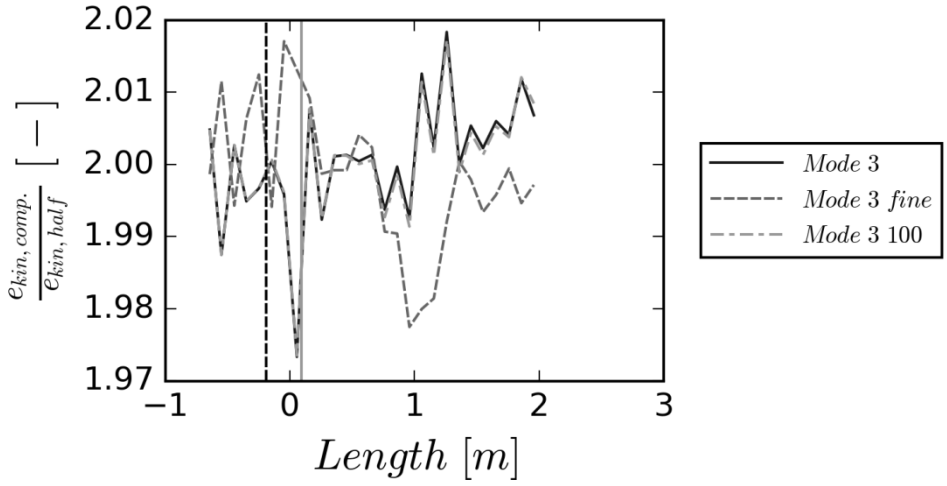

Figure 5-28: Ratio of kinetic energy of complete and half profile over pipe length for Mode 3, Mode 3 fine and Mode 3 100

The trends of static and dynamic pressure do not show differences between all simulations.

γ_g shown in Figure 5-29 is higher for Mode 3 100 than for Mode 3 and Mode 3 fine. The same is true for ϵ and Y. The higher droplet injection velocity causes a better gas distribution with higher evaporation. The mesh dependency for γ_g and ϵ is small.

Angular momentum, angular velocity, kinetic energy ratio and swirl number are only different for different meshes, but do not depend on the droplet injection velocity.

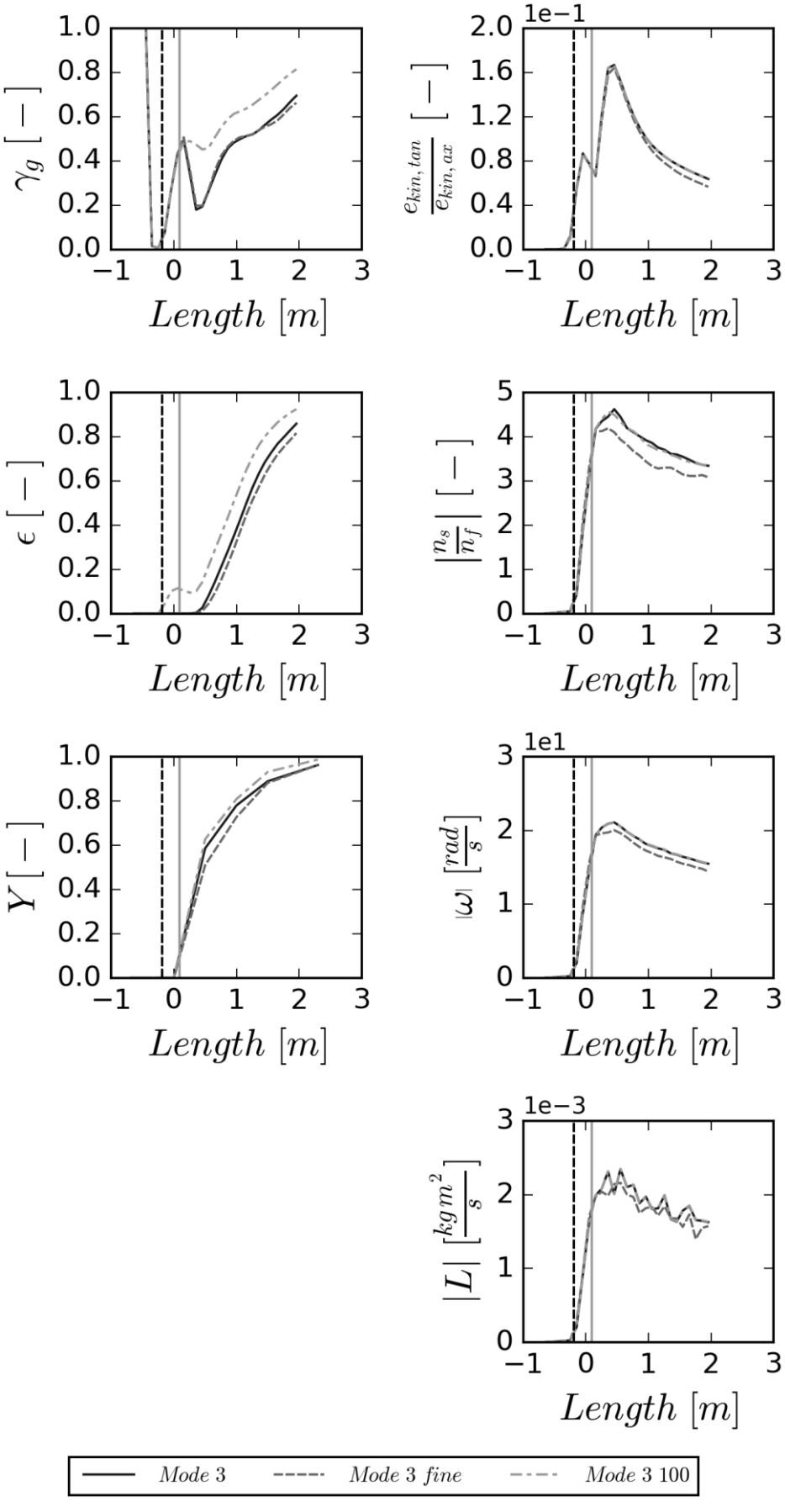

Figure 5-29: Gas mixing properties for Mode 3, Mode 3 fine and Mode 3 100

Kinetic energy ratios and swirl number indicate only a weak mesh dependency. The mesh dependency is higher for the swirl number. Y is higher for Mode 3 100 over the whole length of the simulated domain. Mode 3 and Mode 3 fine differ only slightly.

5.5.2. Spray properties

In Figure 5-30 spray clouds for Mode 3, Mode 3 100 and Mode 3 fine are depicted. Mode 3 100 indicates the best distribution over space. Mode 3 and Mode 3 fine are similar.

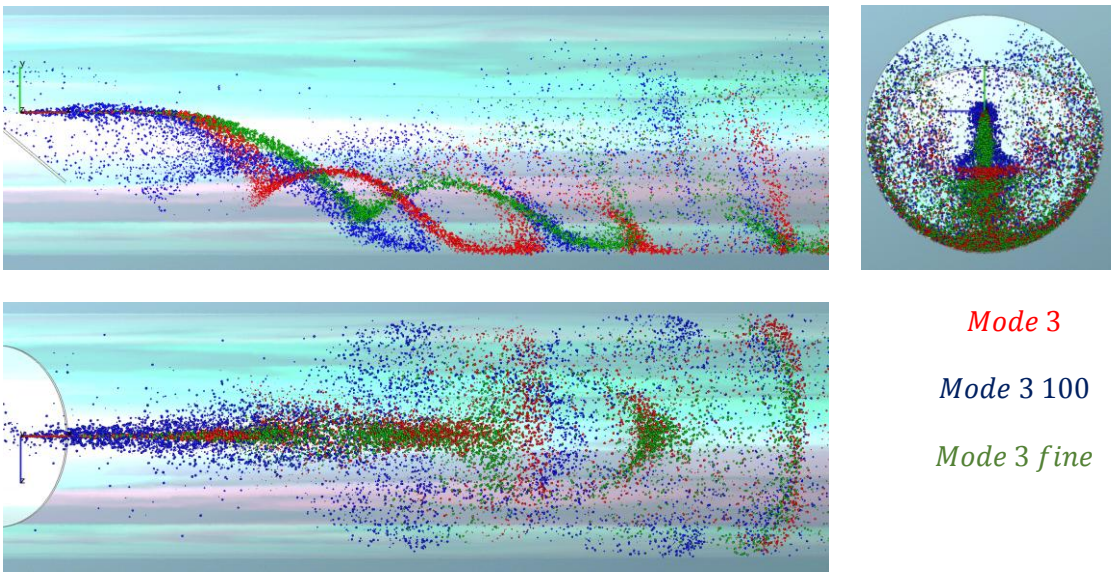

Figure 5-30: Spray clouds for Mode 3, Mode 3 fine and Mode 3 100

In Figure 5-31 the angular momentum ratios are shown. Mode 3 fine and Mode 3 100 have a much better symmetry than Mode 3.

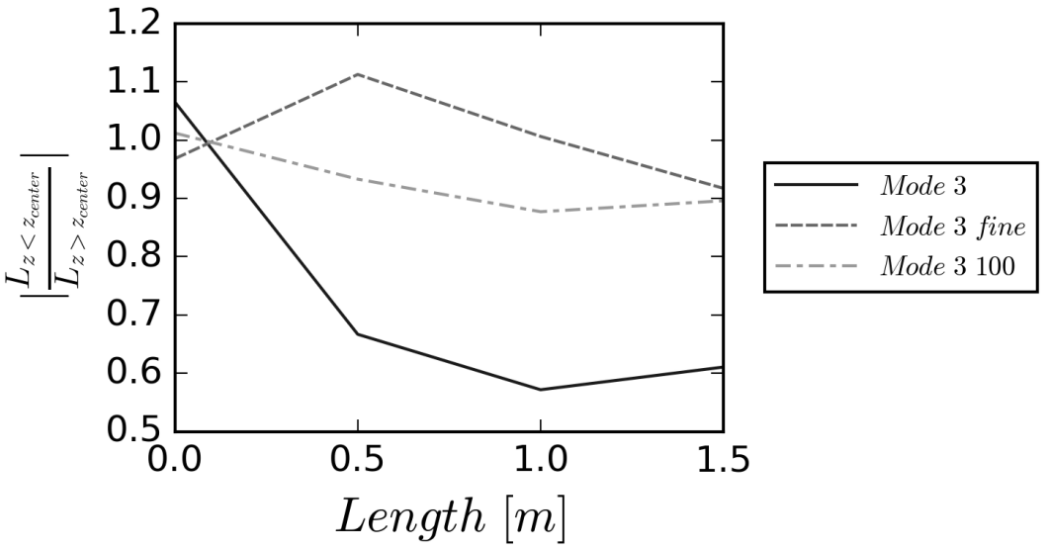

Figure 5-31: Angular momentum ratios of spray droplets for Mode 3, Mode 3 fine and Mode 3 100

Figure 5-32 and Figure 5-33 show similar results as that already shown in Chapter 5.4.5, but here for Mode 3 fine and Mode 3 100. All quantities have a similar time dependent behaviour. Q_m, γ_m and $\frac{S_{WD}}{S}$ are better for Mode 3 100 than for Mode 3 and Mode 3 fine. For Q_m and γ_m no trend can be recognized depending on the grid resolution, i.e., when comparing Mode 3 and Mode 3 fine. $\frac{S_{WD}}{S}$ shows higher values for Mode 3 fine than Mode 3.

In Figure 5-34 and Figure 5-35 the spatial mass flow distribution for Mode 3, Mode 3 100 and Mode 3 fine are depicted. At all positions the distribution is much better for Mode 3 100 compared to Mode 3. This indicates that the droplet injection velocity has a big influence on the distribution, even in case an air assisted injector is used. For Mode 3 fine the spatial distribution is slightly better than for Mode 3.

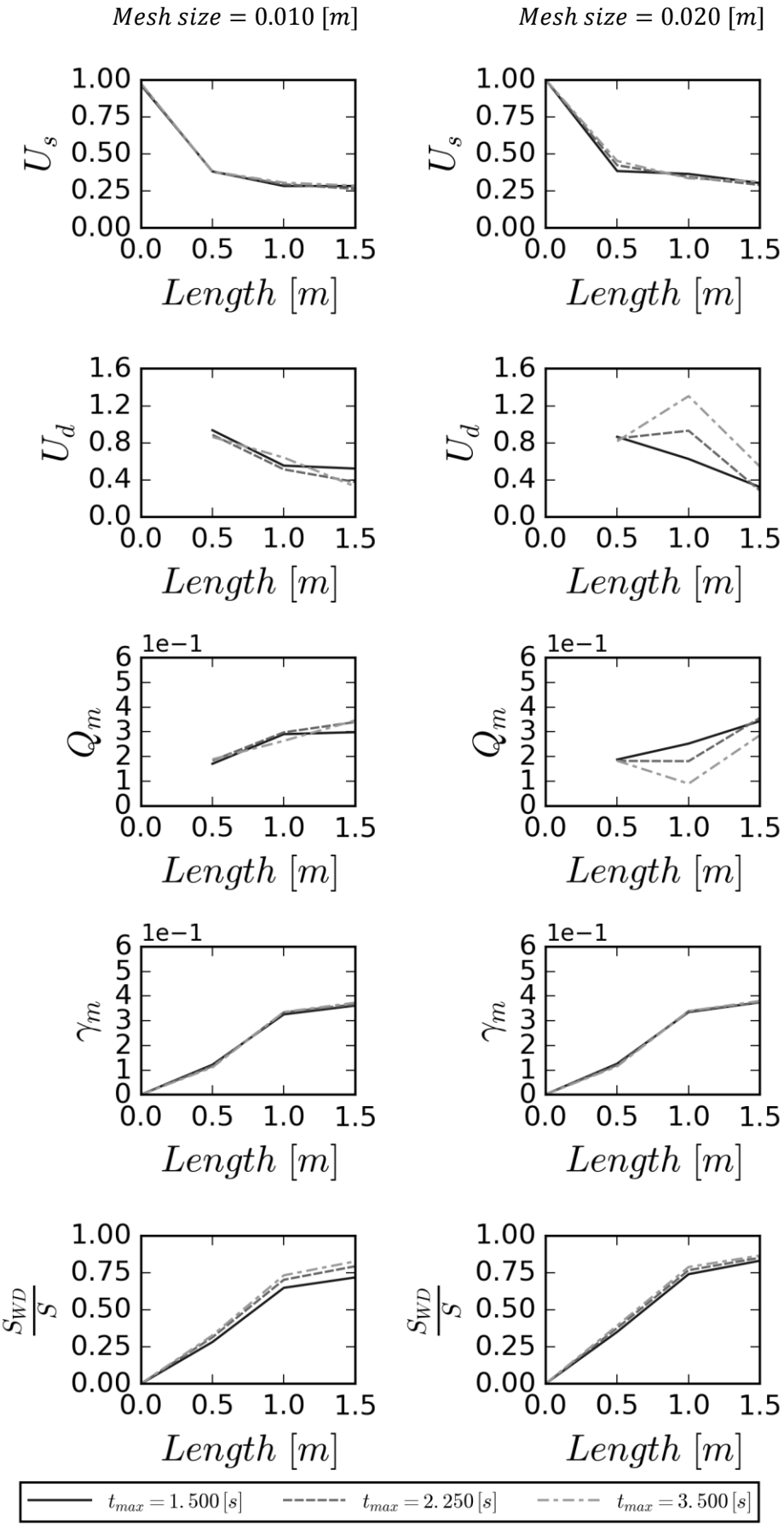

Figure 5-32: Spray mixing factors for different mesh sizes and evaluation times Mode 3 fine

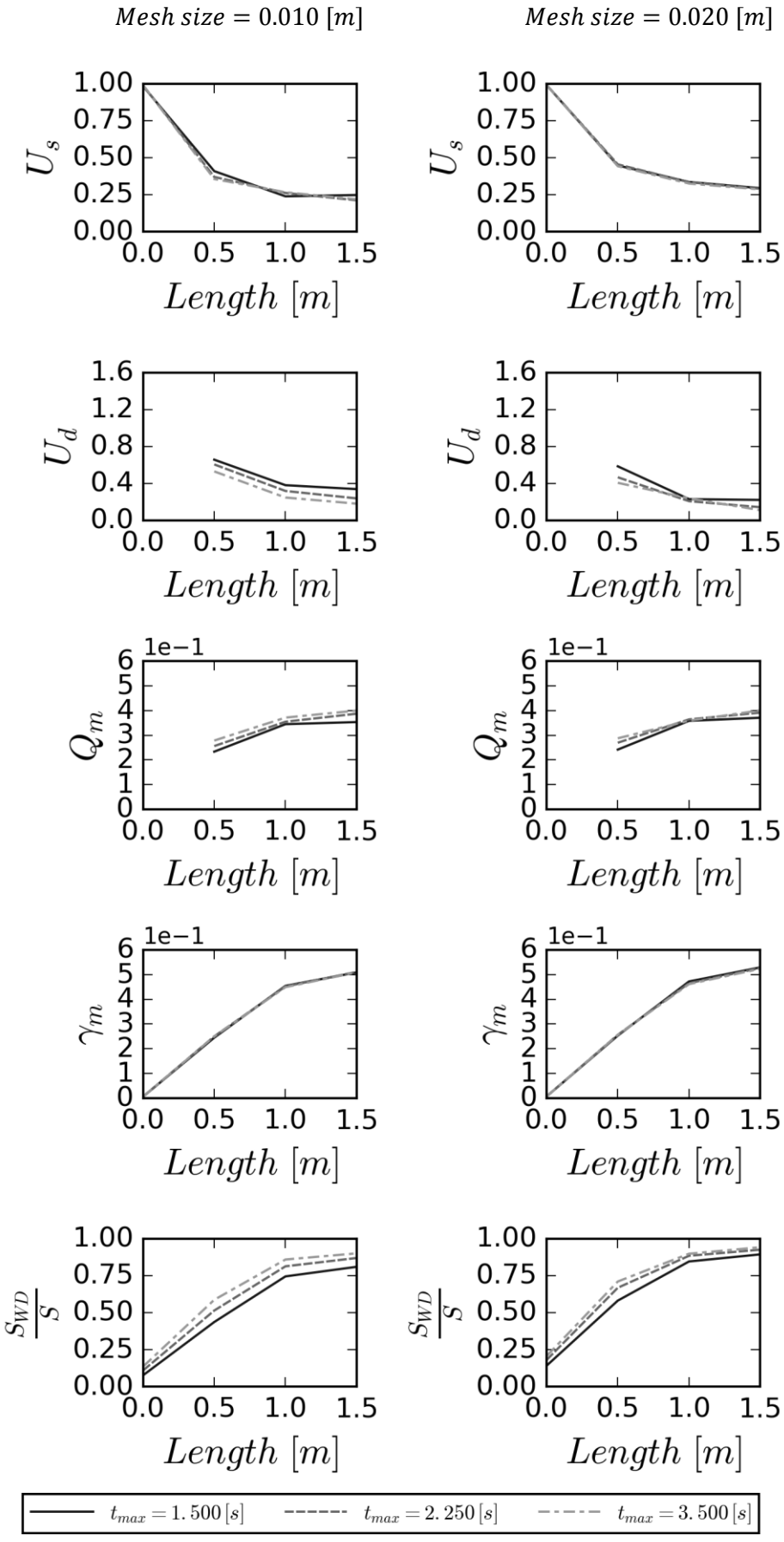

Figure 5-33: Spray mixing factors for different mesh sizes and evaluation times Mode 3 100

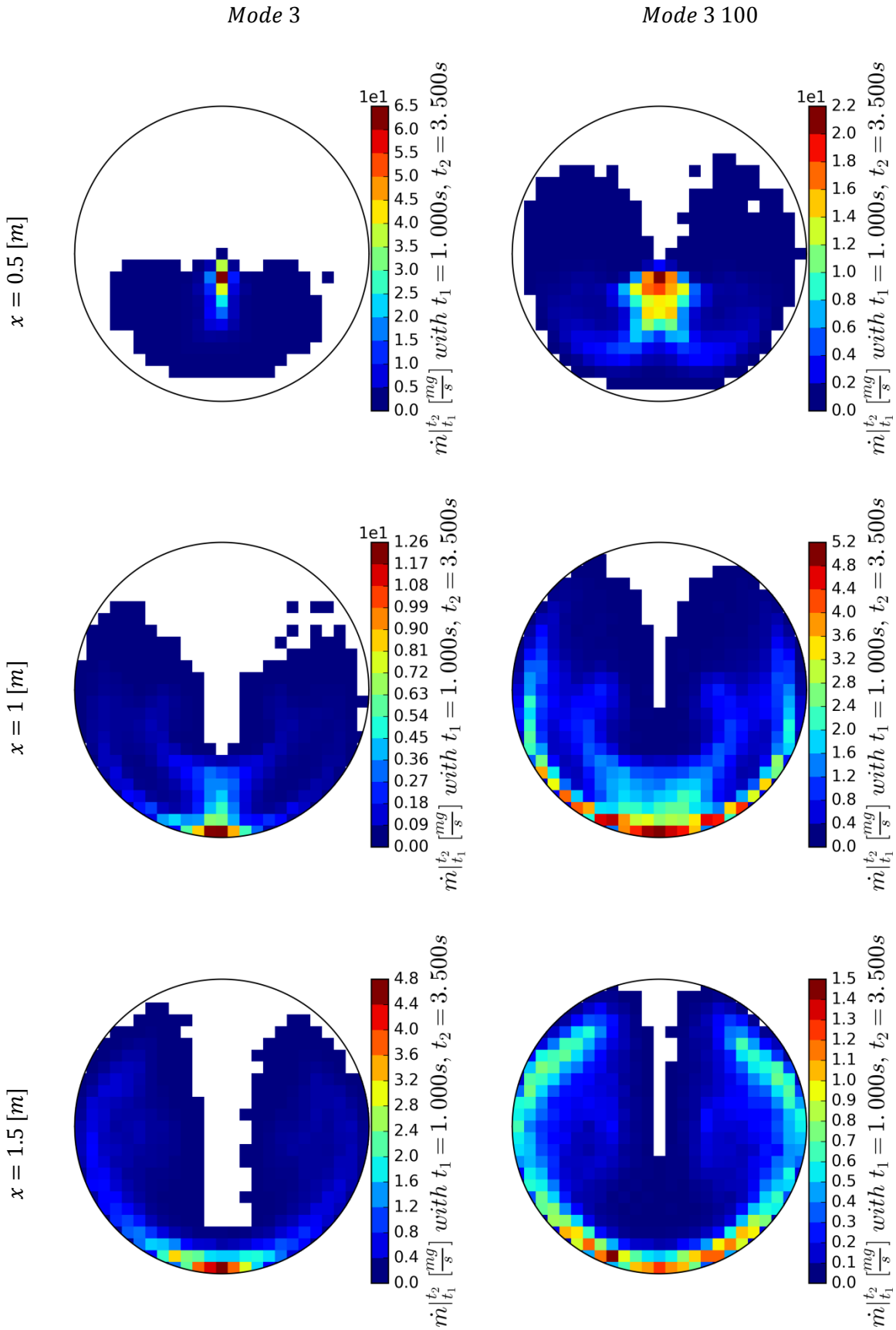

Figure 5-34: Spatial spray mass flow distribution for Mode 3 and Mode 3 100

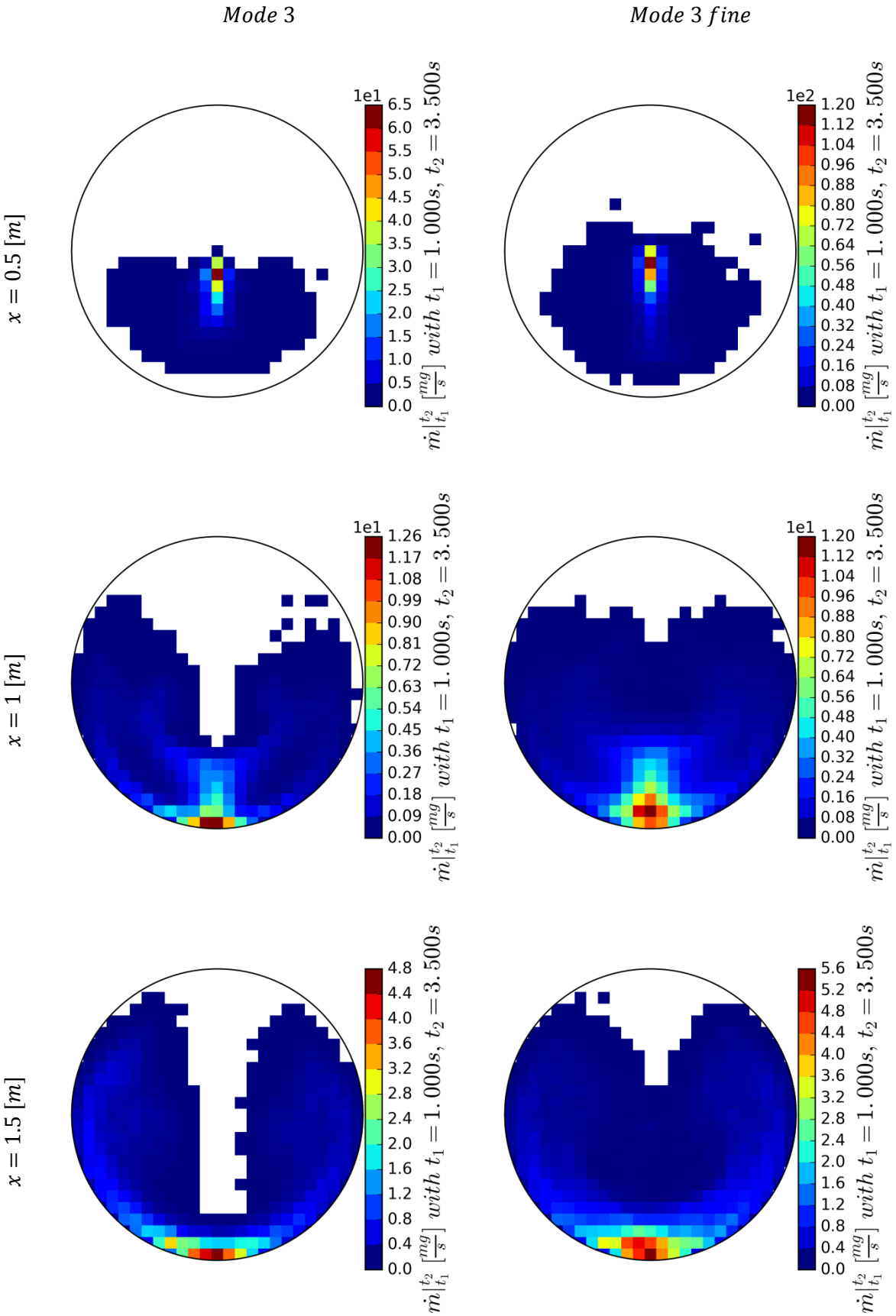

Figure 5-35: Spatial spray mass flow distribution for Mode 3 and Mode 3 fine

5.6. Comparison with and without air assisted droplet injection

In Figure 5-36 a reference geometry is shown which has been calculated without air assisted spray injection (AASI). It has AVL's internal project number G144925.

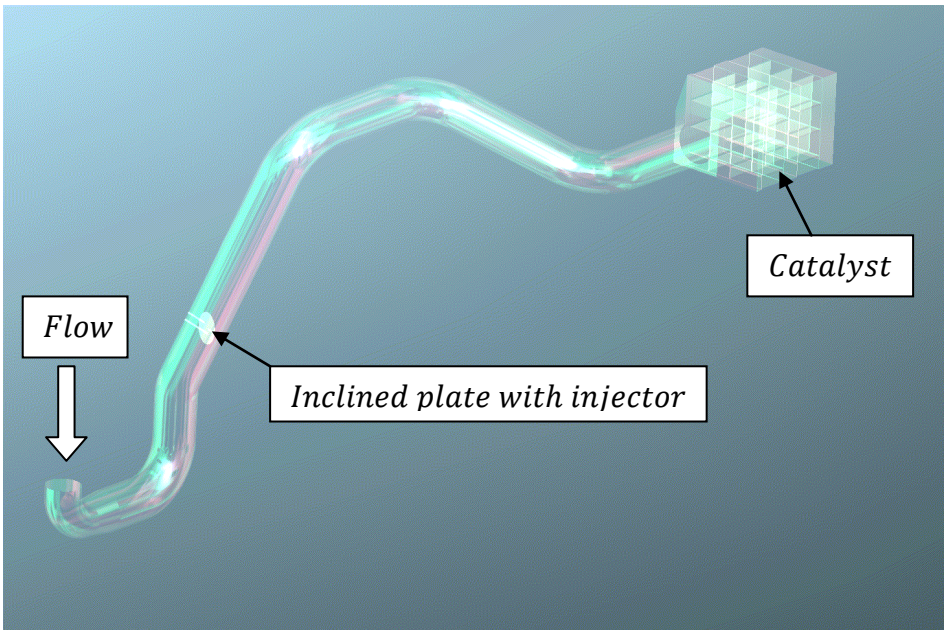

Figure 5-36: Reference geometry without AASI

The goal of this section is to compare γ_g and an indicator for the gas concentration, i.e., ϵ (see Chapter 5.4.4) shown in Figure 5-37 to judge the effectiveness of an AASI.

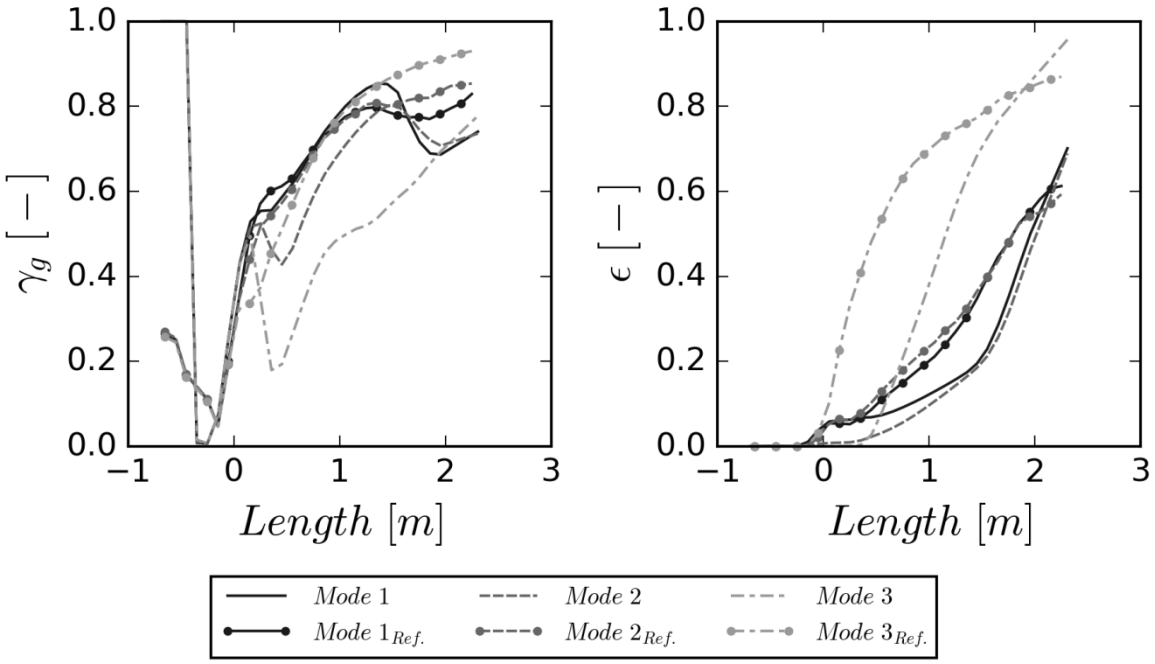

Figure 5-37: Uniformity index and concentration ratio for inclined plate with AASI and reference geometry without AASI

Values for the reference geometry are drawn in with a circle marker in the above diagram. γ_g has higher values near the outlet for the reference case. ϵ increases slower (as a function of the axial distance) with AASI than without it. A possible explanation could be that the air stream of the injector blows away the gas phase, so that it does not mix with surrounding area. This causes lower γ_g and ϵ short after the injector compared to reference geometry. Once the influence of the injector air stream decreases, because of the distance from the injection point, ϵ start to increase rapidly. Near the outlet ϵ is higher with AASI than without. In summary, AASI causes higher evaporation rates and a less efficient distribution.

In Figure 5-38 the swirl number $\left|\frac{n_s}{n_f}\right|$ is plotted as a function of the axial position. The reference geometry shows nearly the same results for all modes, i.e., whether AASI is used or not is not important for the swirl. However, further upstream the magnitude of the swirl number is higher for the reference case than for inclined plate. This is probably due to the flow deflection before the mixer: the inclined plate case has only a straight pipe at the inlet. After that $\left|\frac{n_s}{n_f}\right|$ of inclined plate starts to rise very fast and has higher magnitude than reference case. The two knees in the reference case indicate change of the sign of the swirling motion. This is caused due to a change of the rotation direction of the vortices. Swirl number is evaluated for half cross section with geometrical barycentre as rotation axis (see Chapter 5.4.4). Selections are oriented parallel to the mixer axis.

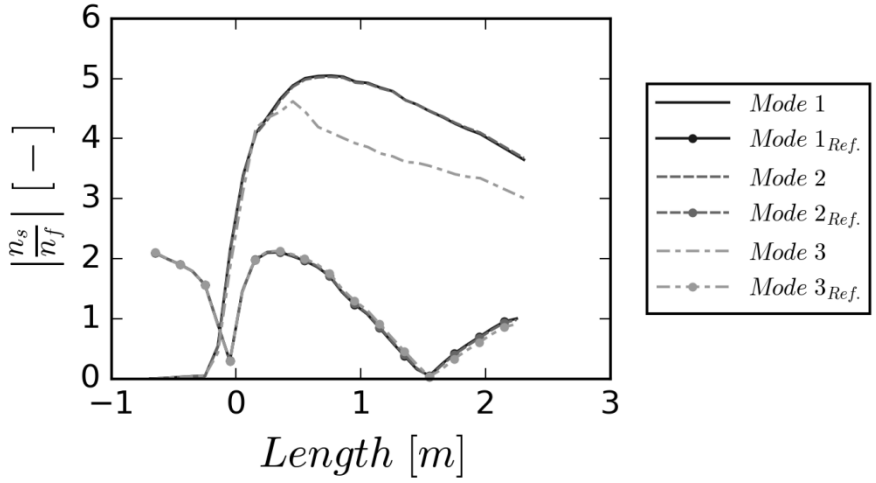

Figure 5-38: Swirl number for inclined plate and reference geometry for half cross section

The swirl number for the complete cross section (see Figure 5-39) shows a quite different behaviour. Reference modes have, over whole length, nearly same value of ~ 1. Only in a

region near the mixer, i.e., close to $x = 0$, it is a little bit lower. In contrast, the inclined plate case has very low values around 10^{-2}.

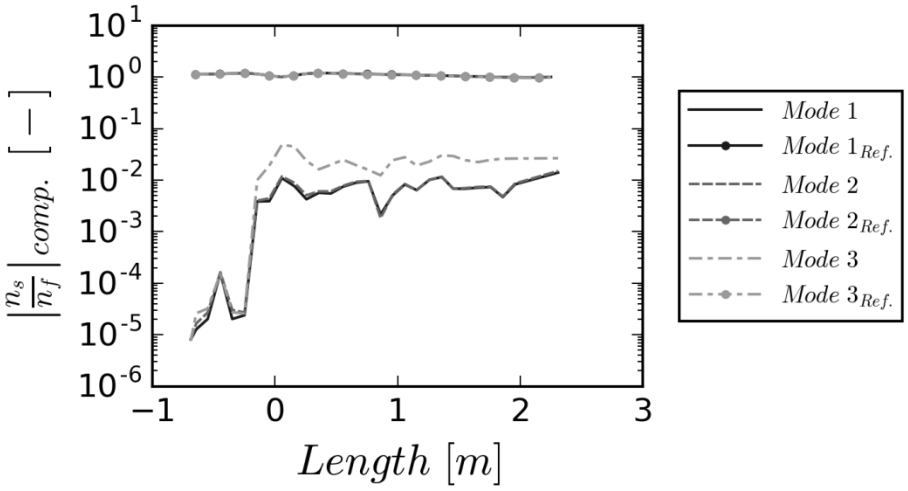

Figure 5-39: Swirl number for inclined plate and reference geometry for complete cross section

In Figure 5-40 the spray cloud for the reference modes are depicted. A significant difference cannot be seen between the three modes. This may be due to the multiple redirections of the flow, which apparently improve mixing.

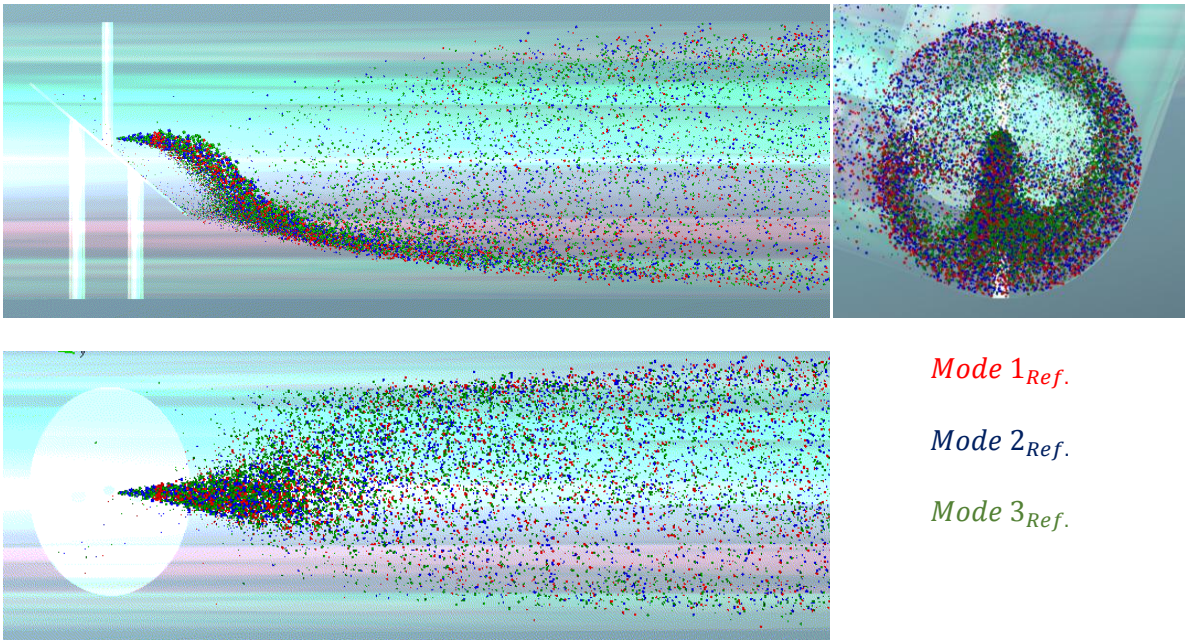

Figure 5-40: Spray cloud for modes without AASI

It is speculated that the two geometries are not completely comparable: the reference geometry without AASI has three redirectings between the inlet and the mixer, which also affects the results.

6. Conclusion and outlook

6.1. Flow parameter

The reference geometry is the benchmark for all further investigations. It has high kinetic energy ratio, swirl number and angular velocity over whole length. These metrics seem to be important for good mixing (see Chapter 2.2 and 2.3), and consequently the reference geometry shows the best mixing properties of all known geometries.

The droplet injection velocity has, even in case air assisted spray injection is used, a significant impact on spray distribution and droplet evaporation. A higher injection velocity allows droplets to escape the air stream from the injector. This effect is significant, and was initially not expected. Also, this effect improves the spray distribution, as well as increases the evaporation rate.

Comparison of air assisted and no air assisted cases show that air assisted spray injection causes higher species concentration, but lower uniformity. It appears that the injected air stream generates a plug flow regions in which a high droplet concentration can be observed. This causes worse mixing, however, a faster evaporation because of the higher relative gas-droplet velocity.

6.2. Spray parameter

U_d, covered area ratio of droplets $\frac{S_{WD}}{S}$ and Q_m show a high dependency on the evaluation duration and mesh size. U_s has a lower, and γ_m nearly no dependence on the evaluation duration and mesh size. Because of this only γ_m is recommended for quantifying spray mixing. To get stable results, however, issues with different gas velocities over the cross section should be investigated in future studies.

6.3. Comparison with literature

It was not possible to compare results of the present work with literature results in a meaningful way. In literature only experiments and simulations at ambient temperature, and in crossflow configuration were made. Because of this, evaporation is much slower than in the more relevant applications studied in the present work. Also, the spray distribution is expected to be different due to the cross flow configuration considered in literature. Thus, only spray parameters detailed in Chapter 2.2 were taken from literature, and no comparison of the mixing performance was conducted.

6.4. Uncertainties

A big problem in mesh generation is the mesh near the injection point (see Chapter 5.1.1). A lot of possibilities with different embedding methods have been tested in the present work. A combination of two connected meshes delivers the most realistic results, however also does not seems to be perfect. This topic is also a current issue in solver development: spray injection simulations using an assisting air stream show a high mesh dependency, and hence ask for additional studies in the future.

A solution to improve this could be the usage of momentum blending functions. There momentum on a droplet is not only taken from one cell into account but from several with a blending function. This allows a much more smooth momentum distribution. Disadvantage of this approach is the very high computation effort.

6.5. Tested geometries

Some geometries not shown in this thesis have been tested based on their mixing performance. A few of these geometries have a comparable mixing performance than that of the inclined plate. For this a target function is introduced which quantifies the kinetic energy ratio R, the gradients of kinetic energy ratios G, and the pressure loss compared to a reference geometry. With this technique, some more promising geometries have been identified.

With best geometry types found by this approach spray simulations with following simplifications are made:

1. No air assisted particle injection
2. Structured mesh
3. Half model with symmetry boundary condition
4. No wall film

One of the geometries (i.e., a guide blade in a rectangular duct) shows at spray simulation with rather certainty similar or even better behaviour than inclined plate. Pressure loss is higher than inclined plate but in same scale. This gives a good starting point for further investigations. With simulations with an air assisted particle injection, an unstructured mesh with the complete geometry (not only a half model) and wall film results of simplified simulations can be proofed. Also geometry optimizations could be made.

One geometry type (i.e., a 90 degree bend) shows no good mixing properties although pressure loss is very high. Because of these issues, such geometries are not suitable as mixers.

6.6. Outlook

In summary, the proposed calculation strategy, i.e., calculation of spray parameters in multiple spray planes, shows a high potential for practical usage. To make more reliable statements on the effect of the geometry, however, the influence of the sampling strategy (see Chapter 2.2.5) has to be investigated in higher detail. Thus, it should be checked whether the sampling strategy is truly able to judge the degree of mixedness, e.g., by considering a number of standard situations (e.g., laminar gas flow with a uniform droplet distribution). Also, usage of momentum blending can potentially improve the results.

The new geometry type mentioned in Chapter 6.5 has potential for further investigations. In the ideal case it can be developed to a mixer type which can be used in marine Diesel SCR applications.

7. Appendix

7.1. Residuals

Important for the solution of the simulation are the normalized residuals. They represent the numerical failure occurred by solving flow equations. Table 7-1 describes the residual outputs from *FIRE*®.

Residual	Description
RESU	Momentum equation x-direction
RESV	Momentum equation y-direction
RESW	Momentum equation z-direction
RESD	Turbulent dissipation
RESK	Turbulent kinetic energy
RESM	Continuity equation
RESH	Energy equation

Table 7-1: Description of residuals

Also the ratios of first to last residual of one timestep are evaluated. Figure 7-1 shows the position of them.

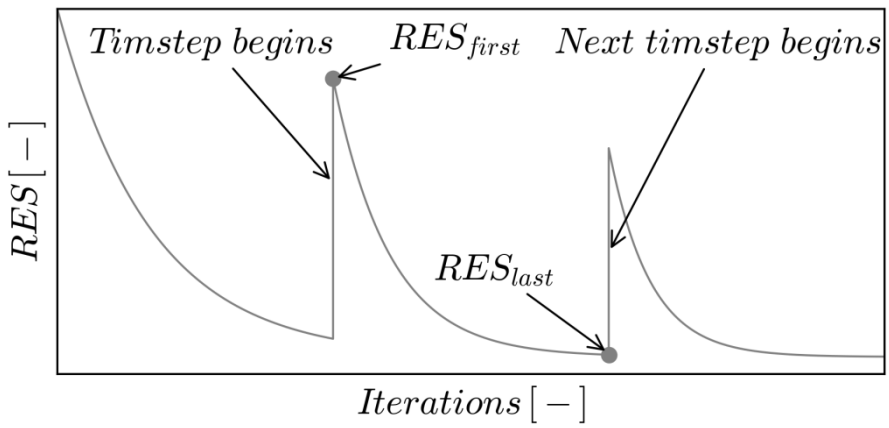

Figure 7-1: Residuals from first and last iteration step

7.1.1. Residuals inclined plate Chapter 5

For Mode 1 the residuals at last iteration at the current timestep are depicted in Figure 7-2 over time. The maximum value of them is lower than 10^{-4} which is sufficient low.

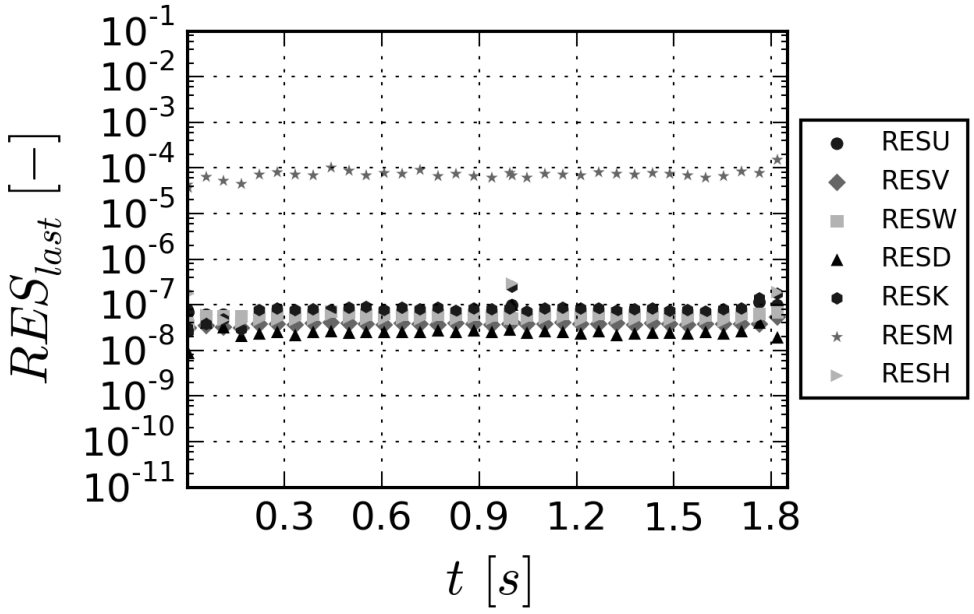

Figure 7-2: Residuals from Mode 1

In Figure 7-3 the ratios of residual of first iteration divided through residual of last iteration from timestep over residual of last iteration from timestep from Mode 1 are depicted. The colours of the markers represent time. After the beginning of the simulation values aspire the bottom side of the plot. This means that the residual of first iteration is getting lower after time and also after a number of iterations it has nearly the same value as at the first iteration. This indicates a good converging simulation. Residuals of Mode 2 and Mode 3 are in same range than in Mode 1.

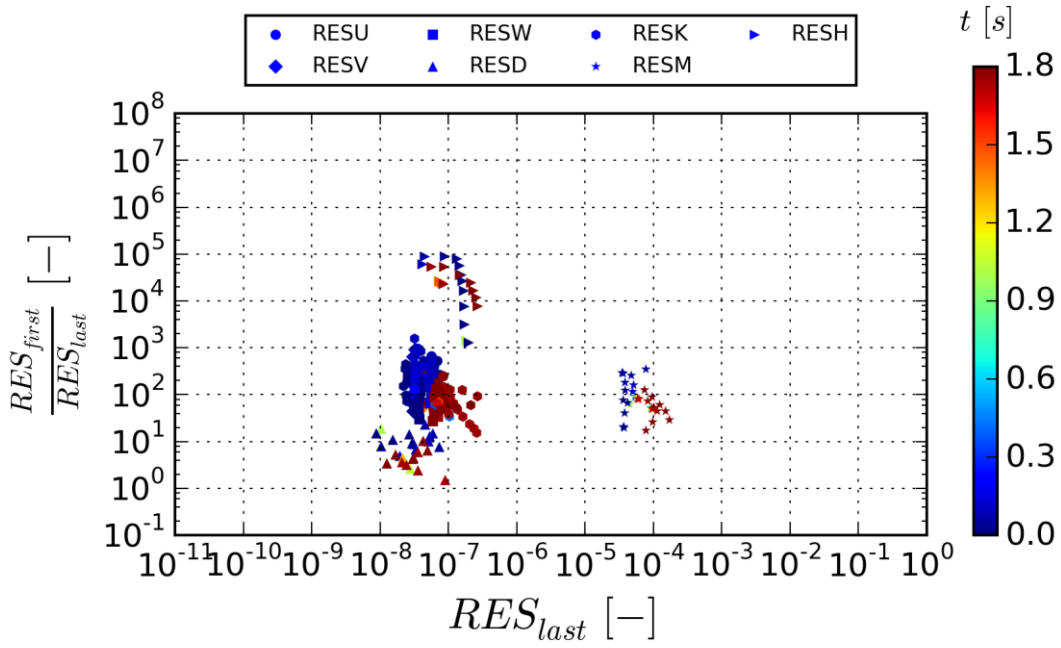

Figure 7-3: Plot of residual ratios of Mode 1